2018-06-25

Modelling In-plane Shear in Partially Reinforced Concrete Masonry

Pan, Huina

UNIVERSITY OF CALGARY

Modelling In-plane Shear in Partially Reinforced Concrete Masonry

by

Huina Pan

A THESIS

SUBMITTED TO THE FACULTY OF GRADUATE STUDIES

IN PARTIAL FULFILMENT OF THE REQUIREMENTS FOR THE

DEGREE OF MASTER OF SCIENCE

GRADUATE PROGRAM IN CIVIL ENGINEERING

CALGARY, ALBERTA

JUNE, 2018

Abstract

Diagonal cracking is the most commonly reported mode of failure for masonry walls subject to in-plane shear loads. Finite element studies were therefore carried out to seek better understanding of this failure mode by attempting to capture the diagonal shear cracks in unreinforced concrete masonry and partially grouted/reinforced concrete masonry. Some key parameters (such as boundary and loading conditions, axial stress, and wall aspect ratio) were examined in the research. Interaction between axial stress and aspect ratio has been noticed. Diagonal compression "strut" was identified from contour plots of principal compressive stress, and therefore two distinct "strut" widths were proposed to account for strength and stiffness of the wall separately. Last but not least, effect of relative panel-to-"frame" stiffness ratio (represented by effective panel-to-frame modulus ratio in this study) has been observed through modelling in partially grouted/reinforced walls. This is rather an important step toward understanding the failure patterns of partially grouted masonry since this factor has not received much attention in the literature.

Keywords: finite element modeling, diagonal cracking, diagonal strut, partially grouted masonry

Acknowledgements

My deepest regards undoubtedly go to my supervisor, Dr. Nigel G. Shrive, for his generous guidance, continuous encouragement and great support throughout my graduate study and the entire period of this research.

Meanwhile, I would like to express my sincere gratitude to Dr. Andrea Isfeld for her continuous consultation and valuable insights regarding finite element modelling issues.

Also, I would like to convey my regards to Dr. Yi Liu and Dr. Xi Chen at Dalhousie University for sharing details of their numerical model with helpful explanations.

In addition, I would like to gratefully acknowledge Dr. Manicka Dhanasekar at Queensland University of Technology for sharing their well calibrated material model.

Last but not least, I would like to thank Dr. Ron C.K. Wong and Dr. Leszek J. Sudak as members of my examination committee for their support and precious time.

Table of Contents

List of Tables

List of Figures and Illustrations

Chapter 1 Introduction

1.1 Background and motivations

It is widely recognized that there are three independent failure modes in masonry shear walls under in-plane lateral load: shear sliding, diagonal shear cracking, and flexural rocking. Combinations of any two or three modes have also been observed in masonry shear walls with various configurations. The diagonal shear cracking mode is the one most commonly reported in the literature, and it is believed to have a more brittle nature when compared to the flexural rocking mode. Understanding the diagonal cracking mode is of importance to understand the in-plane shear behaviour of masonry shear walls, and is therefore of interest in the research presented in this thesis.

The non-homogenous behaviour of masonry makes it difficult to understand the shear mechanism in masonry shear walls. Several major factors have been identified as affecting in-plane shear capacity of masonry walls, such as wall aspect ratio, pre-compressive axial stress, the strengths of the masonry and the mortar-unit bond, and the reinforcement distribution. However, there are still some discrepancies in the literature regarding the effects of certain factors on the mode of failure and the in-plane shear capacity of masonry walls. This might be the reason why different design codes and researchers take into account some leading factors differently when developing their shear models, thus resulting in poor predictions for the in-plane shear capacity of the walls.

Partially grouted masonry is often perceived as an intermediate system between unreinforced masonry and reinforced masonry. In recent years, some researchers started to find that partially grouted masonry can behave differently from both unreinforced and reinforced masonry. Consisting of unreinforced panels and grouted/reinforced cores, partially grouted

masonry can fail either in a wall action (featuring a diagonal/sliding crack spread across the entire wall), or in a panel action (featuring diagonal cracks developed in each panel individually). Partially grouted masonry needs more investigation regarding what factors affect which action to take place when walls of such masonry fail. The effect of relative panel-to-frame stiffness ratio (represented by effective panel-to-frame modulus ratio) in particular will be examined in Chapter 7 in this thesis.

1.2 Aim and objectives

The aims of this thesis are to gain understanding of the diagonal shear cracking mode and to investigate the effects of certain factors on unreinforced masonry and partially grouted masonry through finite element studies.

These aims will be achieved through exploring the following issues:

1. The effects of different boundary conditions and load application methods on the stress distribution in a masonry panel subject to in-plane shear

2. The effects of vertical axial stress and wall aspect ratio on the stress distribution

3. The effect of relative panel-to-frame stiffness ratio (represented by the effective panel-to-frame modulus ratio) on partially grouted multi-panel walls

4. Cracking visualization with the XFEM (extended finite element method) modelling technique

5. Cracking visualization with surface-based cohesive behaviour in simplified microscopic models

1.3 Outline of the thesis

This thesis is composed of eight chapters. Following this introduction chapter, the relevant literature is reviewed with a focus on the modes of failure of masonry walls, the leading

factors known to affect the in-plane shear behaviour of masonry, as well as the difficulties noted in partially grouted masonry.

A finite element study on the effects of different boundary conditions and methods of load application on a masonry test panel is then described. The finite element model is then modified to investigate the effects of wall aspect ratio and the level of axial stress. These topics are subsequently examined in greater detail using a simple cohesive strength model. A new finite element model is then built based on the cohesive strength model to capture the diagonal shear cracking using the XFEM modelling technique.

Failure in all the above models develops from the diagonal "strut" found in the stress contour plots. The diagonal strut is therefore examined to continue exploring the effects of aspect ratio and axial stress. Also, separated "strut" widths for strength and stiffness are proposed and compared with the Canadian Design Standard.

Next, simplified macroscopic and microscopic models are created to examine the effect of relative panel-to-frame stiffness ratio (represented by the effective panel-to-frame modulus ratio) on partially grouted masonry regarding whether the wall will fail in a wall action or a panel action mode in response to in-plane lateral load.

Finally, the major findings from this research are summarized with suggestions for future studies.

Chapter 2 Literature Review

2.1 Introduction

A shear wall is a structural member designed to resist lateral loads induced by wind or earthquake. Therefore, shear walls are particularly important for large or high-rise buildings, or buildings in regions of high wind and seismic activity.

Plain masonry with no reinforcement, also called unreinforced masonry (URM), is an excellent structural material when compressive stresses are predominant. However, the weak tensile strength of masonry becomes insufficient when lateral loads increase to certain levels. Steel reinforcement is considered as a good solution to increase the tensile strength of masonry. Although fully reinforced masonry (RM) can be very effective in resisting wind and earthquake loads, it can be very expensive and might not be necessary in regions of low wind and seismic activity. Partially grouted masonry, which has reinforcement distributed along the length of the wall, with some cores in the masonry remaining unfilled with grout, is therefore used in these situations. When the spacing of the reinforcement is larger than a metre, partially grouted masonry is also called wide-spaced reinforced masonry (WSRM).

This chapter gathers information to understand the behaviour of concrete masonry walls subject to lateral loads. Literature on the major factors that influence the in-plane shear capacity of masonry walls will be reviewed. Partially grouted masonry will be discussed at the end.

2.2 Modes of failure

For masonry shear walls, three independent modes of failure under in-plane shear have been observed by several researchers (e.g.: Drysdale et al. (1993), Mahmoud et al. (1995), Zhuge (1995)). There is consensus amongst researchers that these three modes are shear sliding, diagonal shear cracking and flexural rocking, as shown in Figure 2-1.

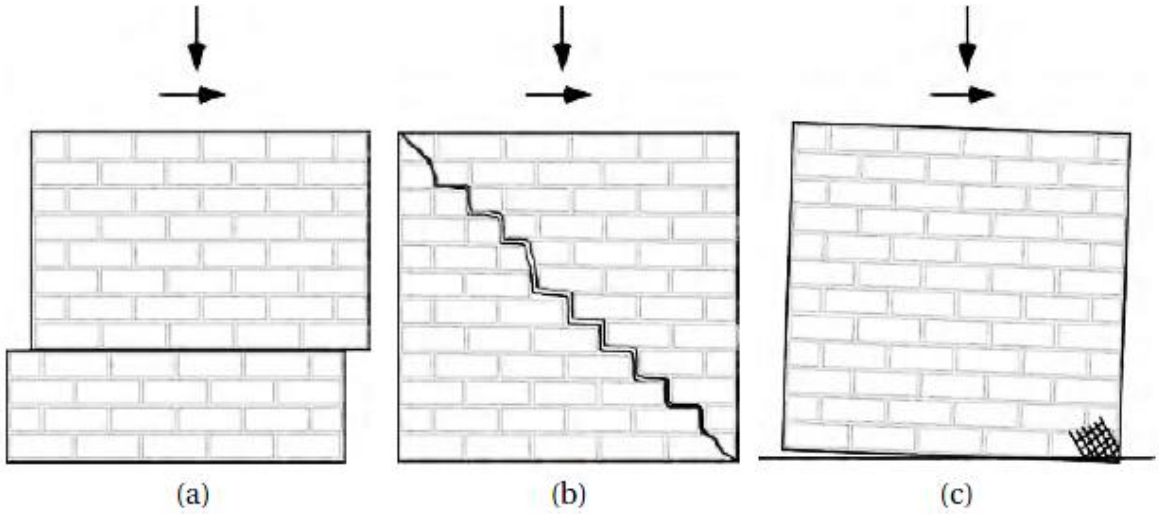

Figure 2-1 Three modes of failure: (a) shear sliding (b) diagonal shear cracking (c) flexural rocking (Petersen (2009))

Shear sliding along horizontal bed joints occurs when the shear stress developed on a bed joint exceeds the bond strength between the mortar and the masonry units. Diagonal shear cracking (either stepping through head and bed mortar joints, or passing through masonry units and mortar joints) occurs when the tensile stress on the diagonal resulting from high principal tension and compression exceeds the splitting tensile strength of the masonry. Flexural rocking failure (tensile cracking at the heel and/or compressive crushing at the toe) occurs due to overturning caused by either a low level of axial stress (vertical pre-compression), a weak tensile bond strength of mortar joints, or insufficient vertical reinforcement.

While the three main failure modes are independent, combinations have also been reported by many researchers. For instance, Benli and Houqin (1991) carried out tests on 40 partially reinforced brick walls subjected to vertical compression and cyclic lateral loads. The cracking pattern of the walls with one or two horizontal reinforced concrete belts is shown in Figure 2-2. The diagonal/sliding failure was produced in the region beneath the lowest reinforcement belt; and the region above the lowest belt remained undamaged.

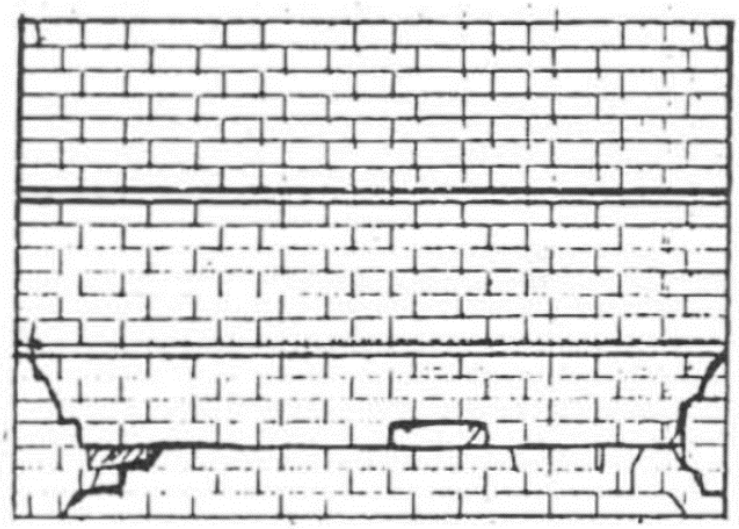

Figure 2-2 Diagonal/sliding failure (Benli and Houqin (1991))

Shing et al. (1990) tested 22 reinforced square masonry walls under axial and lateral loads. Four combined modes of failure were observed from the tests: flexural /diagonal, flexural/sliding, diagonal/sliding, and flexural/diagonal/sliding. They found that walls dominated by the diagonal mode exhibited a more brittle behaviour than those dominated by the flexural mode. Furthermore, they found that increasing the axial stress can shift the failure pattern from a relatively ductile flexural/diagonal mode to a brittle diagonal mode.

Various design codes and researchers recommended different shear models for predicting the shear strength of masonry and the corresponding failure mode. However, these models are vastly different and do not predict the strength and failure mode with consistent accuracy. Dickie and Lissel (2009) gathered experimental data for 75 walls to determine the reliability of eight shear models, including six international design codes. Although it was assumed to predict the failure mode correctly if the model predicted the failure in any one of the modes in the case of combined failures, the best model predicts the correct failure mode in only 73% of the cases assessed.

2.3 Effect of axial stress

The level of axial pre-compressive stress is an important factor that influences the mode of failure and in-plane shear capacity of masonry walls. Several researchers have found that axial stress affects the mode of failure considerably (e.g.: Dhanasekar (1985), Mahmoud et al. (1995), Zhuge (1995)). Generally, a low level of axial stress allows failure in horizontal bed joints, resulting in sliding or flexural failure; a moderate level of axial stress leads to diagonal shear cracking, whereas a high level of axial stress causes compressive failure at the toe of the wall.

There is agreement amongst researchers that increasing the axial stress increases the shear strength of masonry walls (e.g.: Bernardini et al. (1997), Fattal (1993), Shing et al. (1990), Yokel and Fattal (1976)). Prior to the initiation of damage, axial stress improves the bond resistance between mortar and masonry units and prevents principal stresses from inducing tensile stress exceeding the tensile capacity of the masonry. After damage has occurred, axial stress provides higher frictional force between the mortar and the masonry units to resist the shear load.

Haider (2007) reported that increasing the axial stress by 84% on squat walls with an aspect ratio of 0.5 caused only an 11.1 % increase in the in-plane shear capacity of the walls. Voon and Ingham (2006) tested eight concrete masonry walls with different levels of axial stress (0, 0.25 MPa and 0.5 MPa). Their results showed that increases in axial stress of 0.25 MPa and 0.5 MPa on square walls enhanced the in-plane shear capacity by 13% and 22%, respectively.

Ghanem et al. (1993) investigated the effect of axial stress on partially grouted masonry. They concluded that increasing the axial stress changed the mode of failure from flexural rocking to diagonal shear cracking for square walls, whilst increased their in-plane shear capacity. A

maximum of 10% of the compressive strength was applied as axial stress on top of the wall, and this enhanced the shear capacity by 80%.

Kaminosono et al. (1986) tested four walls and found that increasing the axial stress from 0.5 MPa to 2 MPa increased the shear strength by 25%. A change in failure mode with increasing axial stress was also observed from the tests. At low axial stress (0.5 MPa), the mode of failure was flexural. By increasing the axial stress to 2 MPa and more (4 MPa and 6 MPa), a pure diagonal shear failure mode was obtained. Later, after testing 22 wall specimens (14 of which were reinforced concrete masonry walls), Kaminosono et al. (1988) concluded that increasing the axial stress increased the shear strength of the walls whilst decreasing their ductility.

Other researchers have also come to the conclusion that axial stress improves the in-plane shear capacity of masonry walls whilst reducing ductility (e.g.: Alcocer and Meli (1995), Assa and Dhanasekar (2000), Da Porto et al. (2009), Davidson and Brammer (1996)).

Haach (2009) conducted both experiments and numerical simulations on reinforced masonry walls. He found that the mode of failure changed from flexural rocking to diagonal shear cracking in the presence of increasing axial stress. The shear strength of masonry increased with increasing axial stress as reported by many researchers. However, when axial stress increased beyond 40% of the compressive strength of the masonry, compressive failure took place, i.e. the shear strength decreased considerably with a high level of axial stress.

Flexural rocking failure features tensile cracking at the heel and compressive crushing at the toe. Increasing the axial stress can reduce the tension at the heel and increase the compression at the toe. If the compressive strength at the toe is high enough to resist the combined compression, then failure will take place in the next weakest manner – diagonal shear

cracking. The direction of the diagonal cracks is usually parallel to the principal compression, but it is also affected by energy demands. According to Loov (2000), when cracks follow the path requiring least energy, the crack angle can be altered away from the principal compression direction. Oan and Shrive (2011) found the angle of diagonal cracking is affected by the magnitude of axial stress applied to the masonry.

2.4 Effect of aspect ratio

The aspect ratio (height/length) of the wall is another major factor affecting which failure mode will occur. Generally, slender walls (aspect ratio > 1) are prone to fail in flexural rocking mode, whilst squat walls (aspect ratio < 1) are likely to fail in diagonal cracking, and sometimes sliding with low or no axial stress. Square walls (aspect ratio = 1) generally fail in a combined mechanism of diagonal cracking and flexural rocking.

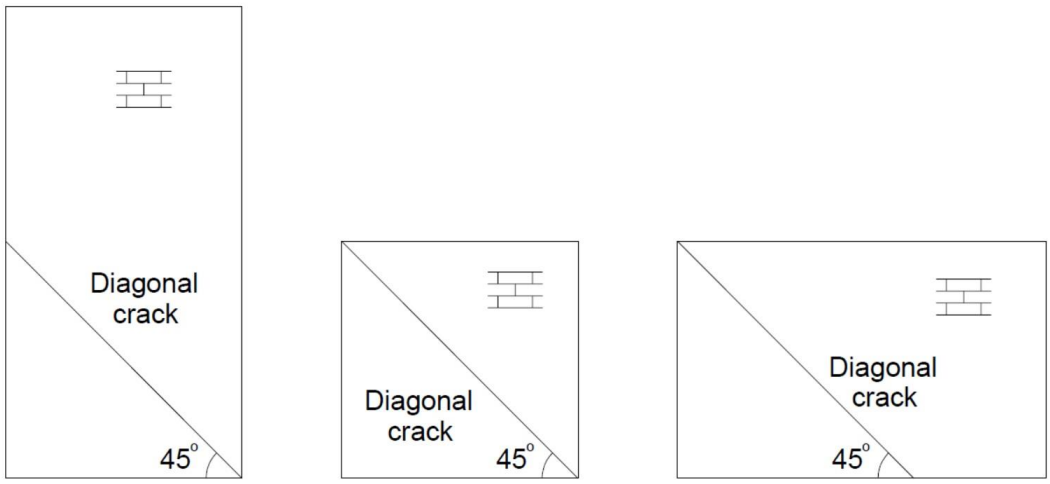

(a) slender wall (b) square wall (c) squat wall

Figure 2-3 Diagonal crack with distinct aspect ratios (Haach (2009))

Shing et al. (1993) examined masonry walls with varying aspect ratios. They found the major diagonal crack remains the angle about 45°, as shown schematically by Haach (2009) in Figure 2-3. In slender walls, the diagonal crack was located in the bottom part of the wall

connecting the loading face and the toe. In square walls, the diagonal crack occupied the whole wall connecting the loading point and the toe. In squat walls, the diagonal crack spread from the loading point with an angle of 45° toward the bottom of the wall, irrespective of the toe.

Davidson and Brammer (1996) tested several reinforced masonry walls and found that shear tends to dominate the flexural behaviour in squat walls (aspect ratio=0.6). ElGawady et al. (2005) examined five unreinforced masonry walls in dynamic and static cyclic tests. The squat walls (aspect ratio=0.45) failed in a combined flexural/diagonal mode, whereas the square walls (aspect ratio=1) failed in flexural rocking mode. Schultz et al. (1998) tested partially grouted walls with aspect ratio of 0.5, 0.7, and 1. Walls with aspect ratio of 0.5 had dominant vertical cracks and some inclined cracks. When the aspect ratio was raised to 0.7, the walls presented more inclined diagonal cracks than vertical cracks, and the in-plane resistance was reduced significantly. For square walls, diagonal cracks dominated at an angle of 45°, which is less steep compared to the walls with an aspect ratio of 0.7.

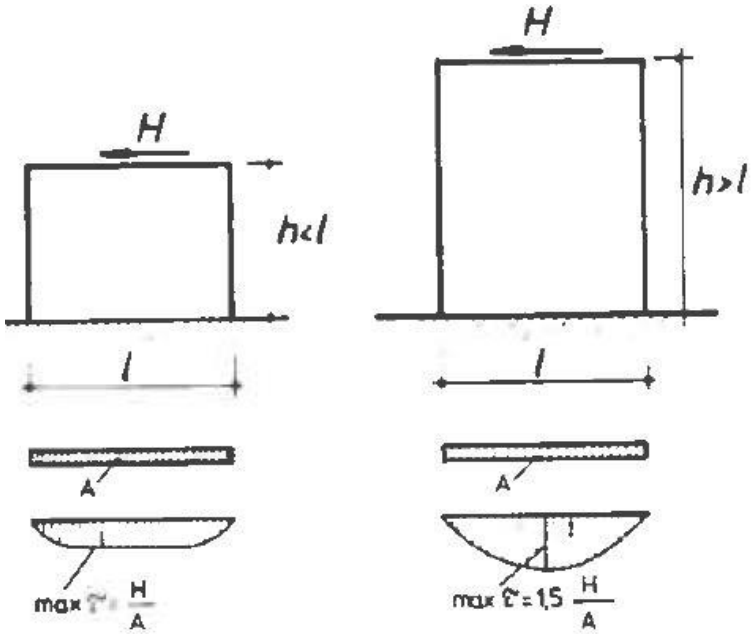

Figure 2-4 Shear stress distribution affected by aspect ratio (Mann and Muller (1982))

Mann and Muller (1982) found that the mode of failure gradually changes from flexural rocking to diagonal cracking with decreasing aspect ratio. They presented the shear stress distribution in squat and slender walls, and indicated their maximum shear stress as in Figure 2-4. H is the applied lateral load and A is the cross-sectional area of the wall. The maximum shear stress in the slender wall is 1.5 times larger than the maximum shear stress in the squat wall, which means the slender wall has less resistance than the squat wall.

Many researchers agree that the shear capacity of masonry decreases with increasing aspect ratio (e.g.: Dhanasekar and Haider (2008), Masami et al. (1986), Schultz et al. (2000), Timothy (2010), Voon and Ingham (2006)). Matsumura (1987) verified this effect by testing 57 concrete walls and 23 brick walls with aspect ratios ranging from 1 to 3.4. Maleki et al. (2009) tested partially grouted reinforced masonry walls with aspect ratios of 0.5, 1, and 1.5. The results showed 10%-31% reduction in shear capacity and stiffness when the aspect ratio was increased.

Brunner and Shing (1996) have reported that walls with higher aspect ratios tend to fail in flexure rocking, whilst walls with lower aspect ratios tend to fail in diagonal cracking. They found that walls with lower aspect ratios had higher shear capacity. 20% and 60% increases in the shear resistance were noticed when the aspect ratio was reduced from 0.93 to 0.72 and 0.59, respectively.

Fattal (1993) investigated the influence of aspect ratio on the behaviour of partially grouted masonry walls based on an extensive data set from past experimental studies. It was reported that as aspect ratio increased, the ultimate shear strength and cracking strength of the masonry walls decreased. No explicit correlation between aspect ratio and deformation was observed in walls with aspect ratios in the range from 0.75 to 3.0.

2.5 Effects of other factors

Material property is another factor that influence the in-plane shear strength of masonry walls. The important material properties are the tensile, shear and compressive strengths of the masonry units and mortar-unit bonds. Riddington and Naom (1994) reported the tensile strength of masonry units can increase the shear capacity of the wall. Dhanasekar (1985) determined that increases in the tensile and shear bond strengths lead to increases in the shear capacity of the wall, while the compressive bond strength has insignificant influence. Zhuge et al. (1998) added that the tensile and shear bond strengths are more influential when axial stress is low.

The strengths of mortar and grout, on the other hand, have limited effect on the shear capacity of the walls (Drysdale and Hamid (1979a), Scrivener and Baker (1988), Riddington and Naom (1994), Hansen et al. (1998), Thamboo 2014).

The type, percentage and location of reinforcement play an important role when it comes to reinforced masonry shear walls (e.g.: Jianguo and Jingqian (1986), Khattab and Drysdale (1993), Ingham et al. (2001), Voon and Ingham (2004), Steelman and Abrams (2007), Banting and El-Dakhakhni (2014), Janaraj and Dhanasekar (2014, 2015)).

Like other researchers have found experimentally and numerically (Shing and Cao (1997), Schultz et al. (1998), Oan and Shrive (2015)), Janaraj and Dhanasekar (2014, 2015, 2016a, 2016b) continuously demonstrated that horizontal reinforcement is ineffective in increasing the in-plane shear capacity of concrete masonry walls through experimental and finite element studies.

2.6 Partially grouted masonry

Partially grouted masonry, or wide-spaced reinforced masonry, is usually considered by designers as an intermediate system between plain unreinforced masonry and fully reinforced

masonry. The Australian Standard (AS 3700-2011) requires partially grouted masonry to have vertical reinforcing bars at spacing between 800 mm to 2000 mm. In the Canadian Standard (CSA S304.1-14), vertical reinforcement can be placed as widely as 2400 mm. The MSJC 2013 Code allows vertical reinforcement to be distributed without exceeding a spacing of 2440 mm.

Over the years, the in-plane shear behaviour of plain masonry and reinforced masonry have been studied extensively through experimental and numerical approaches, while the behaviour of partially grouted masonry hasn't received much attention, and is thus not well understood.

It is not clear how a partially grouted masonry wall, that consists of unreinforced panels confined by grouted reinforced cores, would fail under in-plane shear load. In recent years, there is growing awareness that the in-plane shear behaviour of partially grouted masonry can be different to that of plain masonry and fully reinforced masonry (e.g.: Voon et al. (2000), Dhanasekar et al. (2001), Haider and Dhanasekar (2004a, 2004b), Shrive and Page (2008), Dhanasekar et al. (2008), Hamedzadeh and Shrive (2013)).

It has been reported that partially grouted masonry has an extra failure variation in addition to the aforementioned three independent failure modes and any combined modes. The cracking pattern of a three-panel wall tested by Shrive et al. (2009) is shown in Figure 2-5. A diagonal/ sliding failure developed across the entire wall, namely a "wall action". In contrast, another three-panel wall tested by Hamedzadeh (2013) demonstrated diagonal cracking failure in each of the panels individually, namely a "panel action", as illustrated in Figure 2-6.

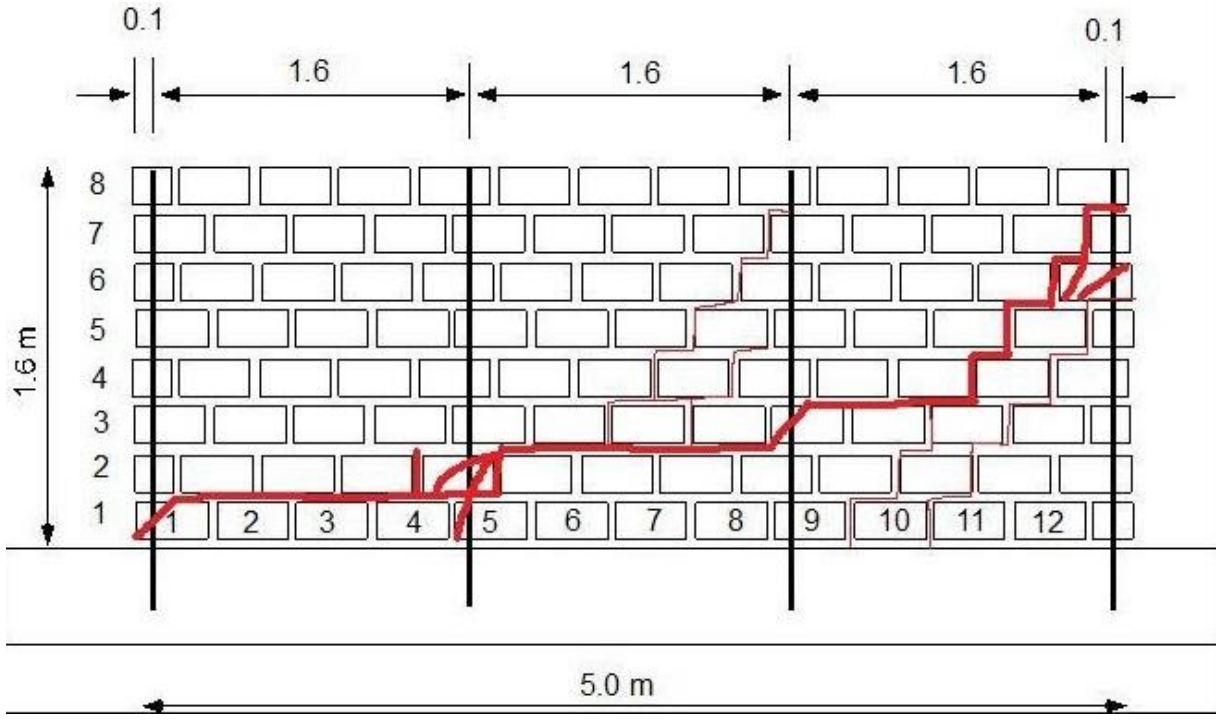

Figure 2-5 Cracking pattern: wall action (Shrive et al. (2009))

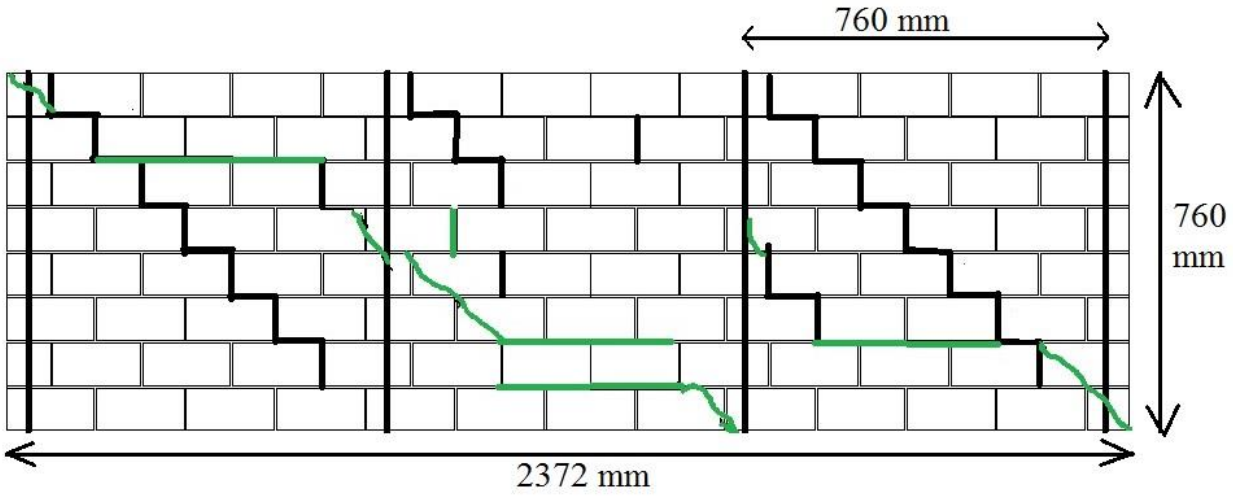

Figure 2-6 Cracking pattern: panel action (Hamedzadeh (2013))

Both walls had aspect ratio of 0.32. Both walls had square panels. Both walls had reinforced bond beams along the top of the wall. What caused the distinct failure patterns in the

two similar walls? The methods of load application were not the same, nor the axial stresses, nor the relative stiffness of the reinforced cores to the unreinforced panels.

Chen and Liu (2015) conducted a finite element study and proposed an analytical method to evaluate the strength of concrete masonry infill walls with openings. When examining several key masonry infill material properties, they found the strength reduction factor (a critical variable in their proposed analytical approach) was remarkably influenced by the variation of the infill-to-frame stiffness ratio. As the infill-to-frame stiffness ratio decreased, a reduction in strength was indicated in the results.

Many tests on partially grouted masonry have been done on single panels reinforced on both sides with a top bond beam. The grouted reinforced cores and the top bond beam form a portal "frame" enclosing the ungrouted masonry. Shing and Cao (1997) built some finite element models to predict the behaviour of partially grouted reinforced masonry walls under cyclic in-plane lateral loads, and calibrated the models with experimental tests conducted by Shultz (1994). The crack patterns show that the behaviour of such a wall is very similar to that of an infilled frame. Bolhassani et al. (2016) tested three full-scale partially grouted masonry walls. They proposed a numerical modeling technique based on the infilled frame concept and calibrated it with the experimental data. They found the behaviour of partially grouted walls was similar to masonry infill walls confined by a concrete frame.

Janaraj et al. (2011) and Dhanasekar et al. (2011) investigated the in-plane shear behaviour of partially grouted masonry walls. They concluded that a critical panel aspect ratio significantly affects the in-plane shear capacity and ductility of the walls.

2.7 Summary

Extensive studies have been done to understand the modes of failure and in-plane shear mechanism of masonry walls subject to lateral loads.

Some agreements can be drawn from literature that: Masonry walls can fail in three independent modes of failure, plus combinations of any two or three modes. An increase in the axial stress increases the in-plane shear capacity of the walls, whilst decreasing their ductility. Oppositely, an increase in the aspect ratio decreases the in-plane shear capacity of the walls. Higher strengths of masonry and bond can improve the in-plane shear capacity of masonry walls, while higher strengths of mortar and grout have limited influence.

On the other hand, it seems that many factors collectively affect the mode of failure, so that conclusions on one certain factor would vary from paper to paper. Similarly, there exist many shear models proposed by different design codes and researchers for predicting the in-plane shear capacity of masonry walls. However, these models take into account the major factors (pre-compressive axial stress, wall aspect ratio, strength of masonry, and reinforcement) differently, and therefore predict the shear strength and mode of failure with inconsistent accuracy.

Partially grouted masonry, or wide spaced reinforced masonry, has received more attention in recent years than in the past. Failures in wall action and in panel action have been reported for multi-panel walls. More investigation needs to be done on what factors cause the wall to take different actions when it fails under in-plane shear loads. Treating partially grouted masonry as masonry infill walls bounded by concrete frame might be a good approach.

Chapter 3 Effects of Boundary Condition and Load Application

3.1 Models without bond beam

3.1.1 Model description.

To begin to understand the in-plane shear behaviour of masonry walls, a 2-D finite element model was built to investigate the influence of different boundary conditions and load application methods on an unreinforced masonry wall, as would be tested experimentally.

In general, there are three common modelling strategies: detailed micro modelling, simplified micro modelling and macro modelling. Detailed micro modelling treats units and mortar joints as continuum elements, whereas unit-mortar interfaces as discontinuous elements. In a simplified microscopic model, mortar joints are combined with unit-mortar interfaces and represented by discontinuous elements. Macro modelling considers the whole masonry assemblage as one composite continuum integrated by units, mortar joints and unit-mortar interfaces.

Since we sought basic understanding of the stress distribution within a masonry wall subject to in-plane lateral load, a simple model was desired in spite of the scale of the wall (the number of mortar joints) or details of the material properties. Therefore, a macro modelling strategy was adopted, an isotropic elastic material model was considered (Young's modulus=10,000 MPa, Poisson's ratio=0.25), and a default 4-node quadrilateral bilinear plane stress element was picked (type CPS4R, with reduced integration and hourglass control).

There are two load application methods that can be commonly seen in experimental tests. In one scenario, the lateral load is applied to the top portion of the wall from the side. In the other scenario, the lateral load is applied to a spreader beam, through which the load is transmitted to the top surface of the wall. In addition, two typical boundary conditions can be found in

buildings: 1) top surface vertically restrained and 2) top surface vertically unrestrained. The walls with their top surface vertically unrestrained are non-structural walls, and the walls with their top surface vertically restrained are load-bearing walls. Typically, test specimens are subject to one of these two conditions, depending on what situation the experimenter is trying to simulate. Hence, four finite element models were built to represent the two load applications and the two top boundary conditions as shown in Figure 3-1.

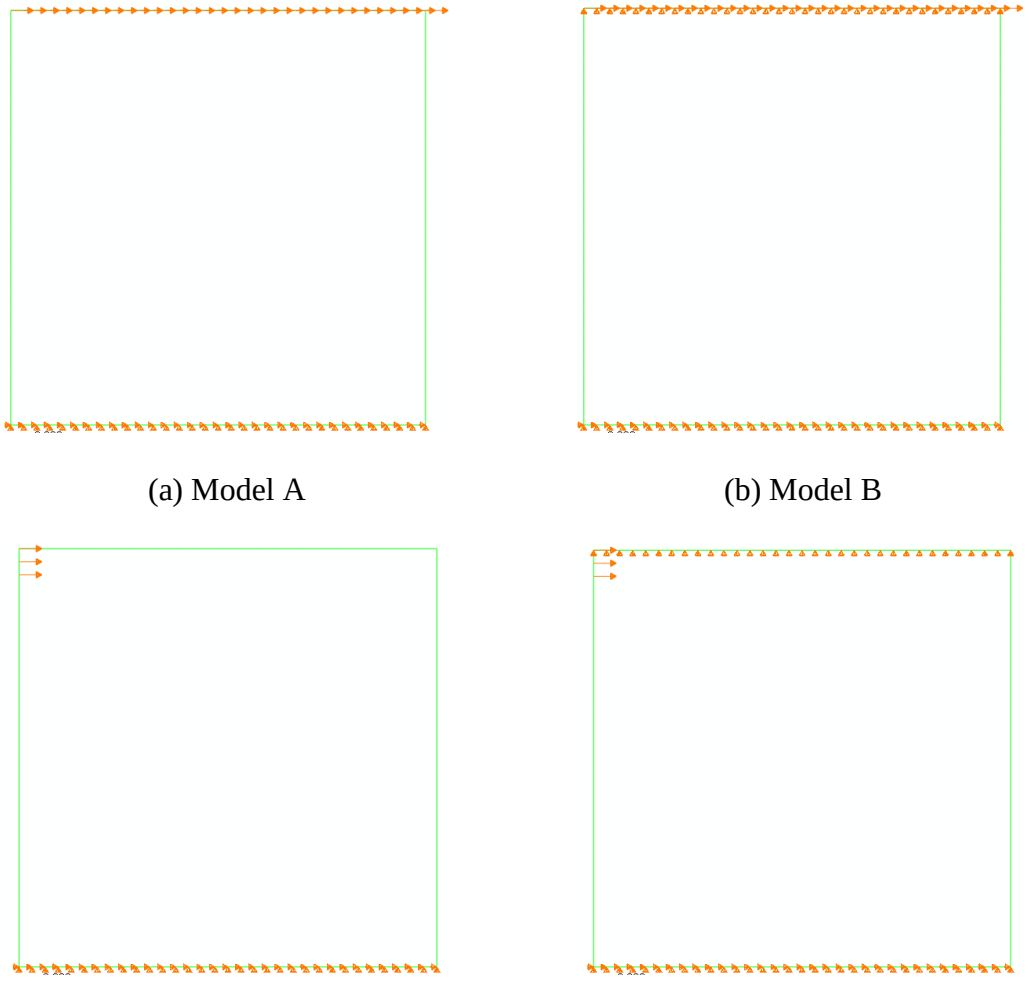

(a) Model A (b) Model B

(c) Model C (d) Model D

Figure 3-1 Models with different boundary and loading conditions

The bottom surfaces of the four walls are constrained in both the horizontal and vertical directions, whilst the top surfaces of the walls are either free (Model A and Model C) or constrained vertically (Model B and Model D). Lateral shear load is applied from left to right in the form of a horizontal displacement. This load is applied either to the top surface of the wall (Models A and B) or over the top one-tenth of the left loading surface (Models C and D). Model A simulates the case where a spreader beam is pushed laterally, but not constrained to remain horizontal – the additional constraint in Model B. Model C simulates those tests where the lateral load is applied to the side of the top course of masonry in the wall. Model D has the same load application as in Model C, but has the top surface constrained to remain horizontal.

A mesh convergence study was carried out using Model B. Lateral load applied to the top surface of the wall and minimum principal stress at the centre node of the wall were examined. The results were plotted against the number of mesh seeds on each edge of the wall as shown in Figure 3-2. It shows that the model can provide sufficient accuracy if the number of elements on each edge reaches 14 or above. A mesh seed of 20 was finally picked for the four models to obtain smoother contour plots for comparison in the next step.

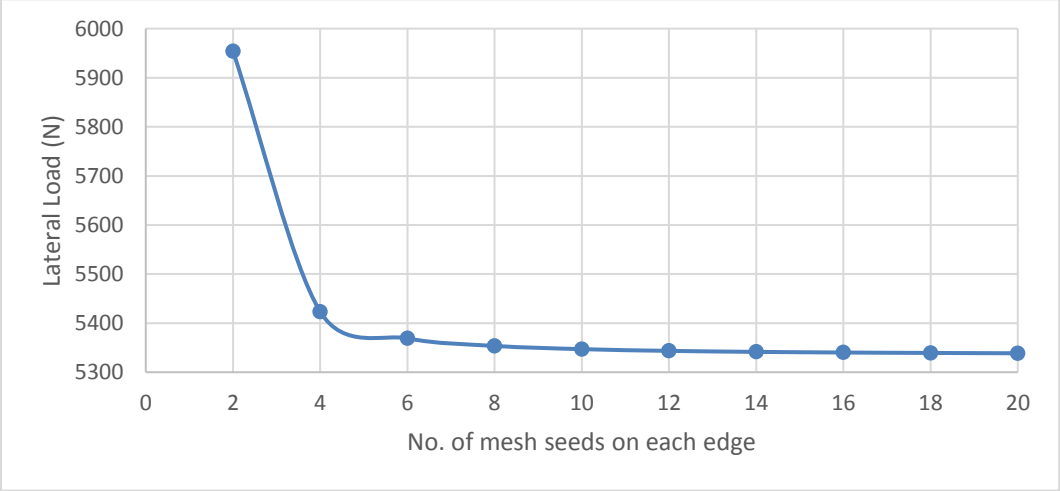

(a) Lateral Load applied to the wall

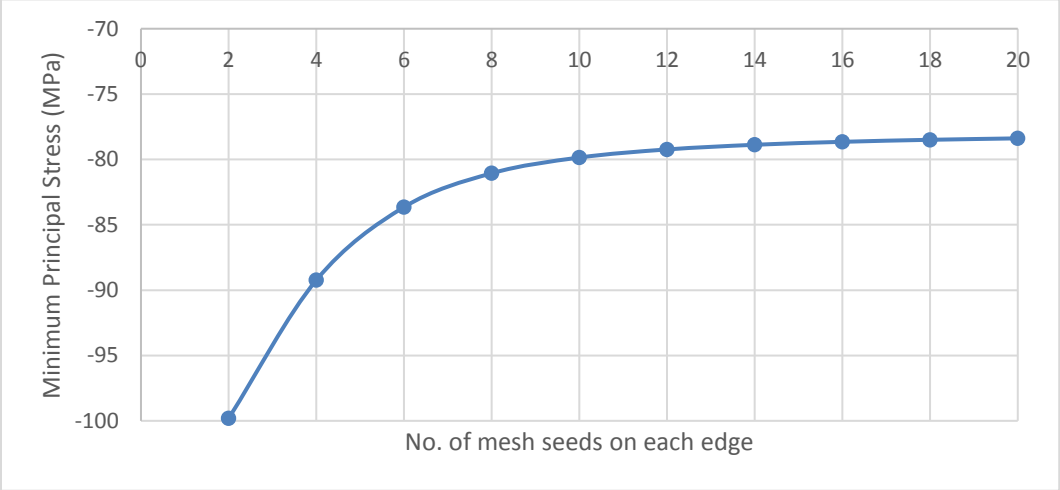

(b) Minimum principal stress at the centre node of the wall

Figure 3-2 Mesh convergence study results

3.1.2 Results and discussion.

Figure 3-3 shows the distribution of normal stress in the direction of the diagonal, which is nearly the minimum in-plane principal stress (i.e. maximum principal compression) across the wall. Models C and D have severe deformations at the top left corner as the load is applied intensely to that area. Additionally, Model D has undesirable large principal compression (in the blue colour) due to the vertical constraint. Compared with Model A, Model B has a clear compression zone along the diagonal and a symmetric stress distribution with respect to the diagonal. This stress distribution matches perfectly with the diagonal cracking mode which has been commonly observed in experimental tests. Therefore, the boundary and loading conditions adopted in Model B will be inherited to the next investigation.

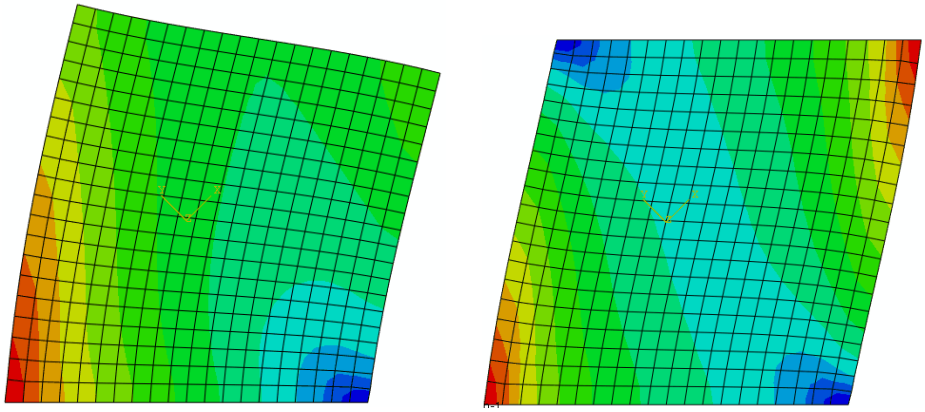

(a) Model A (b) Model B

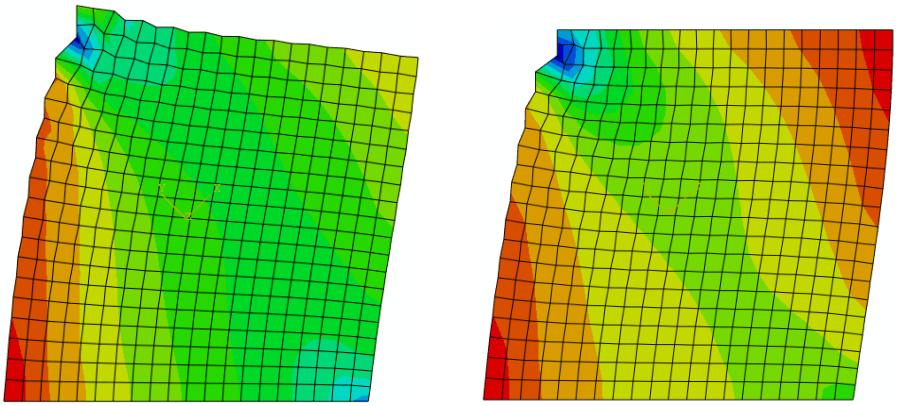

(c) Model C (d) Model D

Figure 3-3 Stress distribution in the diagonal direction

3.2 Models with bond beam

3.2.1 Model description.

Large principal tension was noticed to have developed at the top right and bottom left corners of the wall under Model B's configuration, as shown in the red colour in the symbol plots in Figure 3-4. In order to release the tension in the top right corner, a bond beam was placed on top of the wall, as shown in Model E. An isotropic elastic material was assumed for the bond beam as well. The Young's modulus of the beam was set as 100,000 MPa, which is 10 times stiffer than the masonry wall. The Poisson's ratio of the bond beam was given as 0.25. The

interface between the bond beam and the masonry wall was defined by a surface-to-surface contact with cohesive behaviour properties (normal stiffness=100 N/mm^3, tangential stiffness =2,000 N/mm^3). This allows the top surface of the wall to separate from the bond beam so as to release some tensile stress, as would occur in an experimental test.

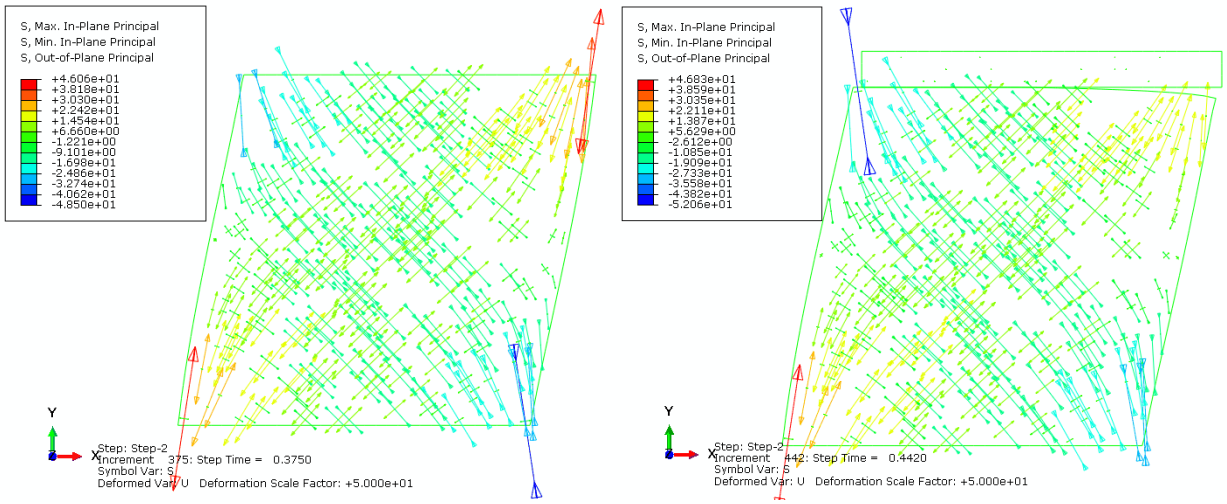

(a) Model B (b) Model E

Figure 3-4 Principal stresses in walls with and without a top bond beam

Similar to the configuration of Model B, the bottom surface of Model E is fixed in both the x- and y- directions. Instead of the top surface of the wall, the bond beam is constrained in the vertical direction, and then subject to a displacement-controlled lateral load from left to right.

Figure 3-4 gives the symbol plots of the maximum and minimum principal stresses of Model B and Model E when they have developed the same value of reaction force at the bottom surface (it took a little more time for Model E to develop the same reaction force under displacement-controlled load application due to the tangential cohesion in the contact). Comparing plot (a) with plot (b) shows that adding a top bond beam effectively releases the tension at the top right corner.

To better represent what happens in tests, another bond beam was placed at the bottom of the wall to release the tension at the bottom left corner. With the same elastic material properties as the top bond beam, the bottom beam also has the same cohesive behaviour properties as the top beam for the surface-to-surface contact connecting it with and the masonry wall. At the same time, the bottom beam is constrained in the horizontal and vertical directions so that the bottom surface of the wall is set free.

In experimental tests, an actuator is usually attached to the bond beam and applies lateral load to the beam first. The shear load will then be distributed along the beam and transferred to the wall. Thus, it will be examined whether the location and area of the contact between an actuator and the bond beam affects the load transmission to the wall and therefore affects the stress distribution in the wall. Three loading conditions are represented in Figure 3-5. The displacement-controlled lateral load was applied either over the whole top beam (Model F), or on the central vertical line of the top beam (Model G), or on a square area at the centre of the top beam (Model H).

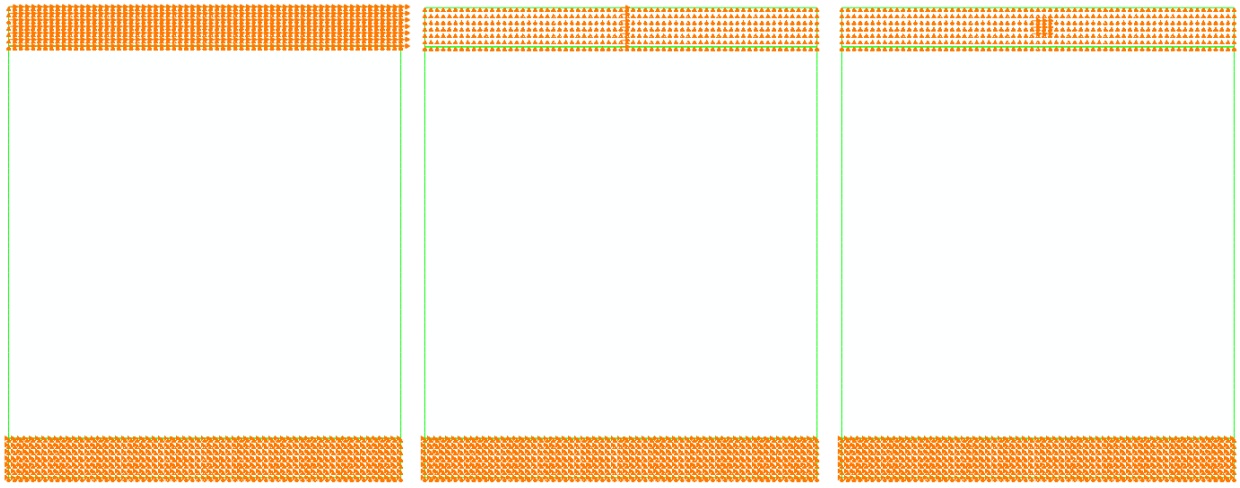

(a) Model F (b) Model G (c) Model H

Figure 3-5 Models with different load application methods

3.2.2 Results & discussion.

Figure 3-6 gives the contour plots of the principal compressive stress parallel to the diagonal for Models F, G and H (with the bond beams hidden from view). The different loading applications represented by the three models produced almost the same stress distributions across the walls. Therefore, the display stress limits were adjusted to highlight the possible differences between the three models.

After the adjustment of the display stress limits, a slight difference is noticed near the middle of the top surface of the wall. Among the three models, Model F has the symmetric stress distribution with respect to the main diagonal, which is desirable for further investigation of other important factors. Hence, the configuration of Model F was adopted to examine the effects of axial stress and aspect ratio in the next chapter.

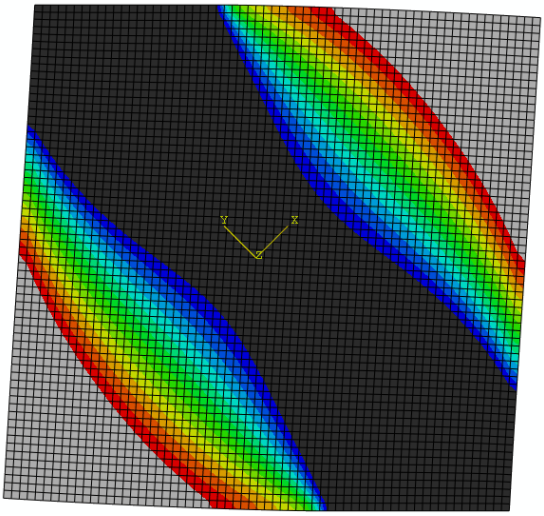

(a) Model F

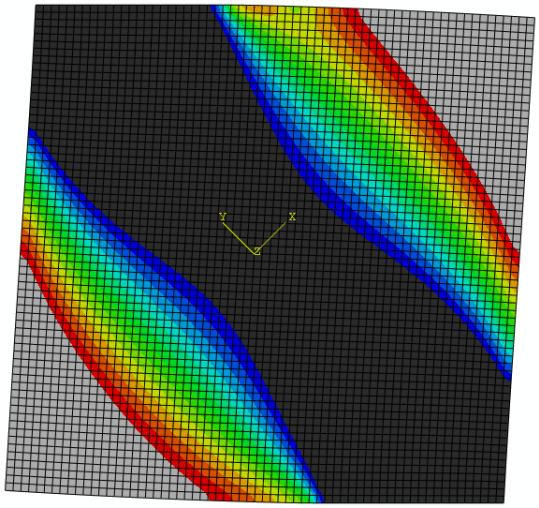

(b) Model G

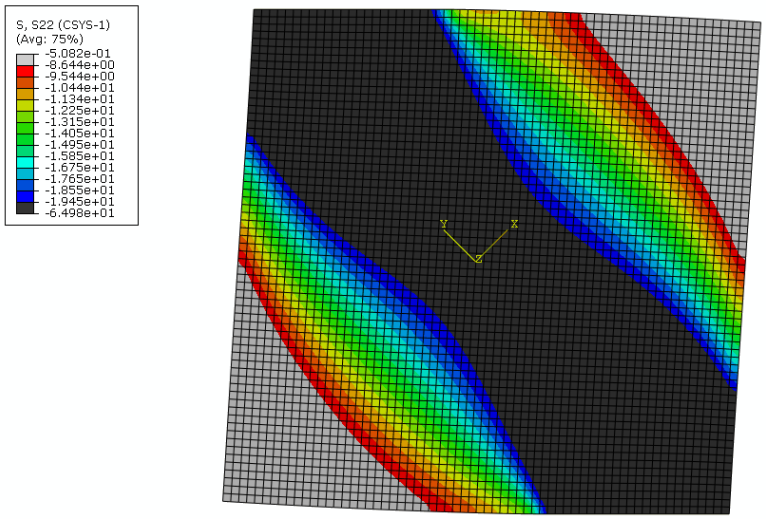

(c) Model H

Figure 3-6 Principal compressive stress parallel to the diagonal

It is worth mentioning that, with the help of adjustment of the display stress limits, a compressive "strut" appeared in the diagonal direction from top left to bottom right, as shown in Figure 3-6. The black colour zone represents high principal compression where failure might initiate, whilst the grey colour zone bears very little compression.

It is clear from these plots that the width of the high compression zone (blue-to-blue width) is much narrower than the width of the material that is compressed (red-to-red width). In other words, the width of material that is being compressed and will therefore contribute to the stiffness is wider than the width of high compressive stress where failure is likely to initiate and therefore the width for predicting the strength. Further investigation on the compressive "strut" width will be discussed in Chapter 6.

Chapter 4 Effects of Axial Stress and Aspect Ratio

4.1 Basic models

Both Model B and Model F, described in Chapter 3, were selected as basic models for investigating the effects of axial stress and aspect ratio on an unreinforced masonry wall under in-plane shear. As shown in Figure 4-1, Model B is the original model without bond beams, while Model F is the improved model with the beams. Both models contain a square wall made of isotropic elastic material standing for unreinforced masonry (Young's modulus=10,000 MPa, Poisson's ratio=0.25). In Model B, the bottom surface of the wall is confined in horizontal and vertical directions. The top surface is restrained vertically, and is subjected to evenly distributed lateral load in the form of horizontal displacement. The same boundary condition and lateral load application were applied to the bond beams in Model F.

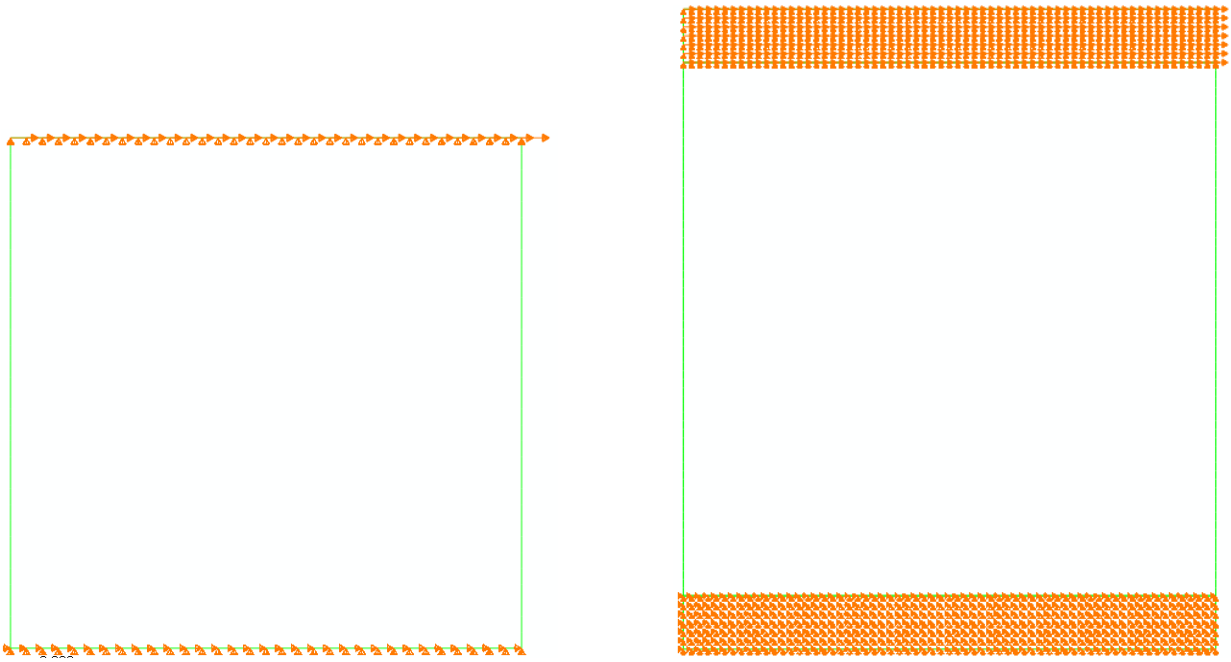

Figure 4.1 Model F with bond beams

4.2 Effect of axial stress

4.2.1 Model description.

To investigate the effect of axial stress, the vertical restraint on the top surface of Model B was removed. The loading application was divided into two steps. In the first pre-compression load step, the top surface of the wall was subject to five different levels of axial stress respectively (0, 1 MPa, 2 MPa, 5 MPa and 10 MPa). Under each level of axial stress, the vertical displacement of the nodes on the top surface were obtained, and the average vertical displacement was calculated. The top surface was then kept to the average vertical displacement in the second lateral load step, when shear load (in the form of horizontal displacement) was applied to the top surface as well.

4.2.2 Results and discussion.

Maximum and minimum principal stress data were collected at thirteen points when the horizontal reaction force reached 1000 N. The points are situated on the two perpendicular diagonals and divide each diagonal into eight equal segments. These data were arranged as in Figure 4-2 to show how the principal stresses change along the two diagonals when axial stress is increased. Each grid (outlined by black lines) contains two values of principal stress at one of the thirteen points, and the grid is arranged according to the corresponding point's relative geometric location on the diagonals.

When there is no axial stress, the principal stress distribution was found to be symmetric with respect to the two diagonals. With increasing axial stress applied to the upper surface of the top beam, as may be seen in Figure 4-2, the principal tensile stresses on the two diagonals decrease. This suggests that the wall should be able to bear more shear load with the increasing axial stress.

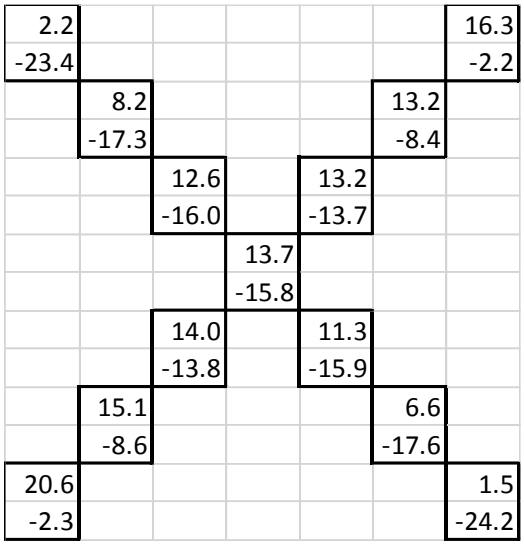

(a) axial stress = 1MPa

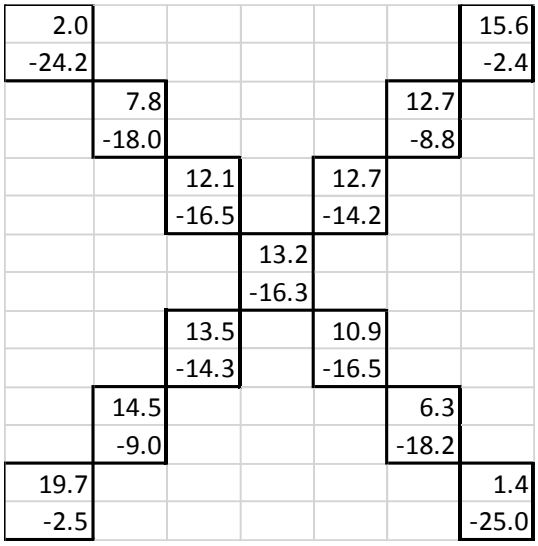

(b) axial stress = 2MPa

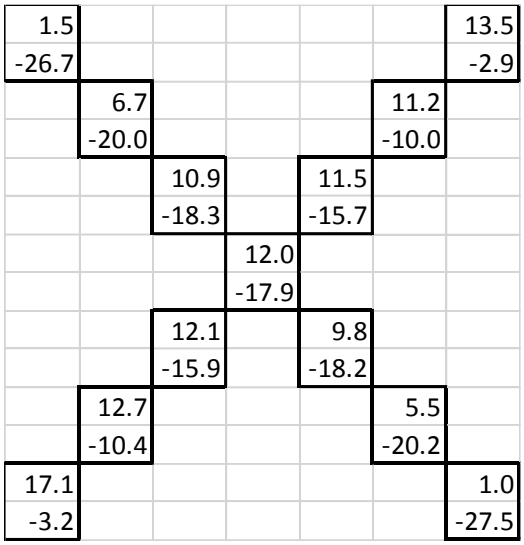

(c) axial stress = 5MPa

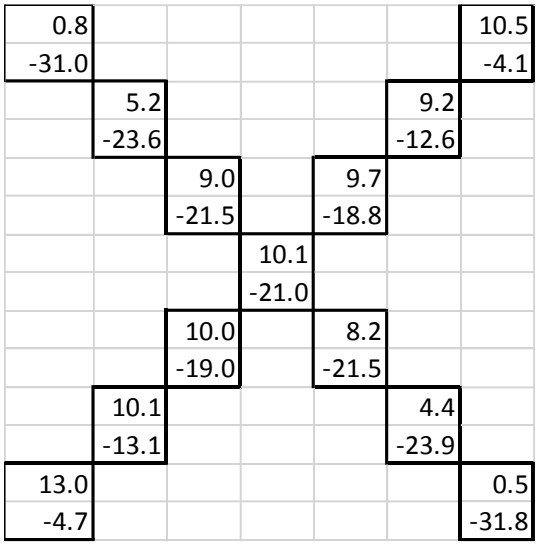

(d) axial stress = 10MPa

Figure 4.2 Principal tensile and compressive stresses on the two diagonals

4.3 Effect of aspect ratio

4.3.1 Model description.

To observe the effect of wall aspect ratio (height/length), a geometric change was made to the Model F. The wall width was kept at the same value, while the wall height was adjusted to

different values so that the wall aspect ratio was shifted to 0.5, 0.75, 1, 1.5 and 2, respectively. Also, a surface traction was applied to represent the shear load to the upper surface of the top beam, replacing the previous displacement-controlled load which required extra work to find the sub time step to make sure reaction forces reached the same value in all cases. No axial stress was applied in this modified model.

4.3.2 Results and discussion.

Figure 4-3 shows the symbol plots of the minimum and maximum principal stresses distributions in the walls with increasing aspect ratio. The deformation scale factor is set as 10. The direction of the arrow indicates the direction of the principal stress, and the length of the arrow indicates the magnitude of the stress.

When the aspect ratio is 0.5, the distribution of principal compressive stress seems to be of a widely-spread pattern. As the aspect ratio is increased, the distribution of principal compressive stress gradually changes to a more concentrated pattern aligned with the compressive diagonal.

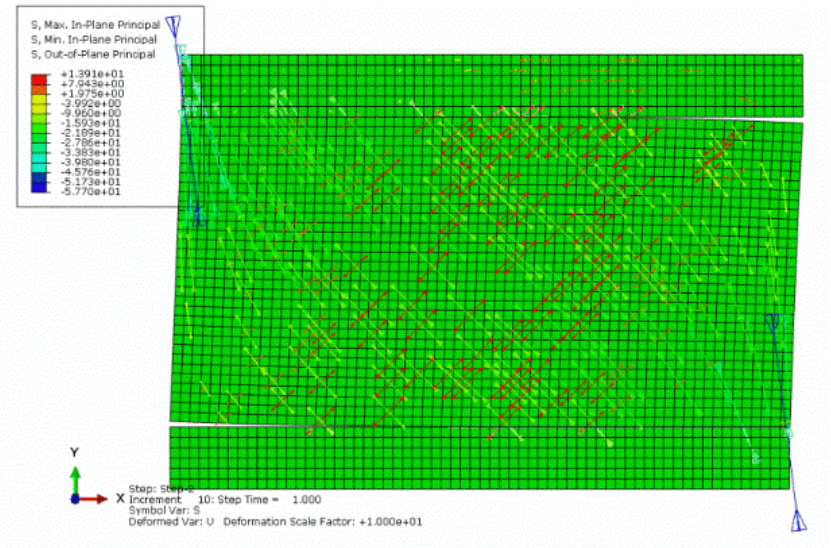

(a) aspect ratio=0.5

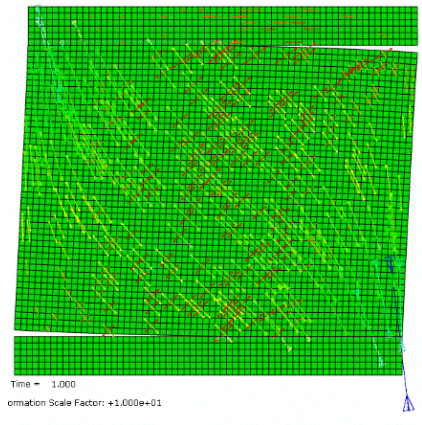

(b) aspect ratio=0.75

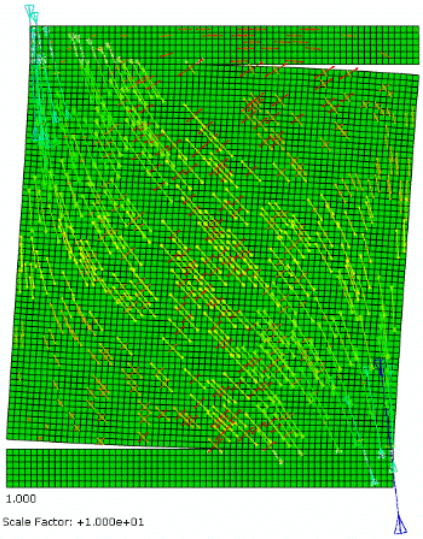

(c) aspect ratio=1

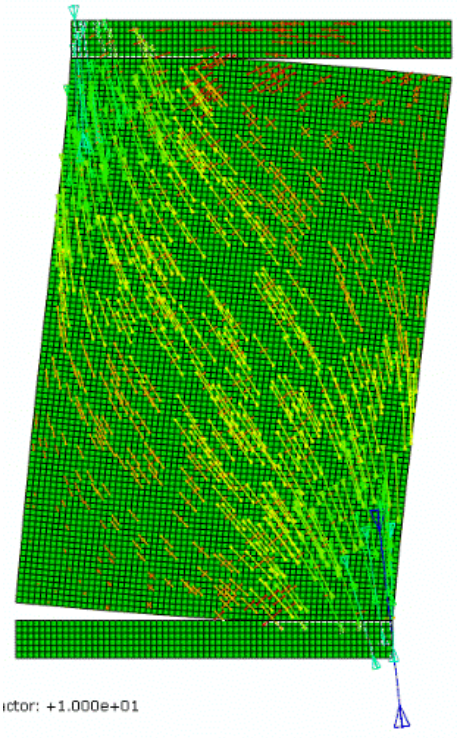

(d) aspect ratio=1.5

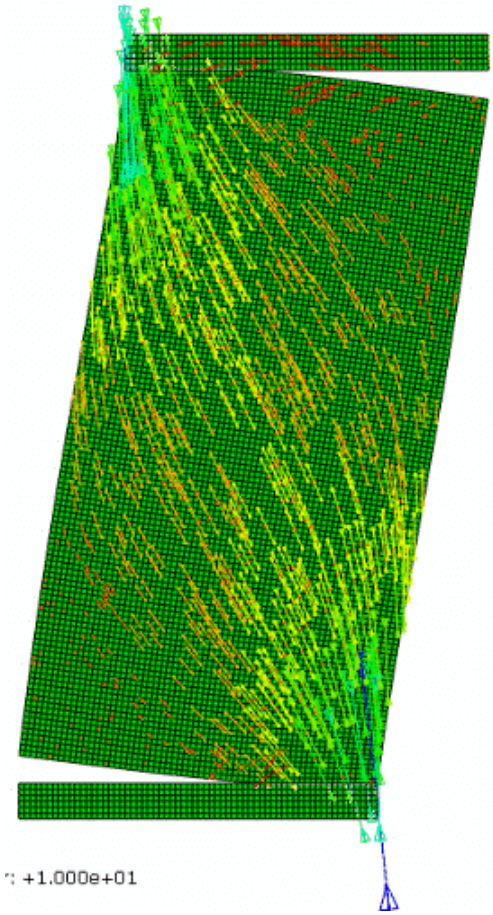

(e) aspect ratio=2

Figure 4.3 Minimum and maximum principal stresses

4.4 Combined effects of axial stress and aspect ratio

4.4.1 Model description.

To further discuss the effects of varying levels of axial stress and aspect ratios on the stress distribution within the wall, the two modified models described in the last two sections were combined into a new model subject to different levels of axial stress (0, 2 MPa, 5 MPa, 10 MPa) and with varying aspect ratios (0.5, 0.75, 1, 1.5, 2), resulting in 20 cases in total.

4.4.2 Results and discussion.

To collect principal stress data, three quadrisection lines of and perpendicular to the compressive diagonal were drawn as shown in Figure 4-4. Given that the elements are kept the same size in these models, the number of the nodes that can be found on the quadrisection lines is varying since the wall changes aspect ratio. The principal compressive stress data on the three quadrisection lines were acquired from the result files. The data on the bisection line (middle line) were considered most typical among the data on the three lines, and are plotted in Figure 4-5 and Figure 4-6.

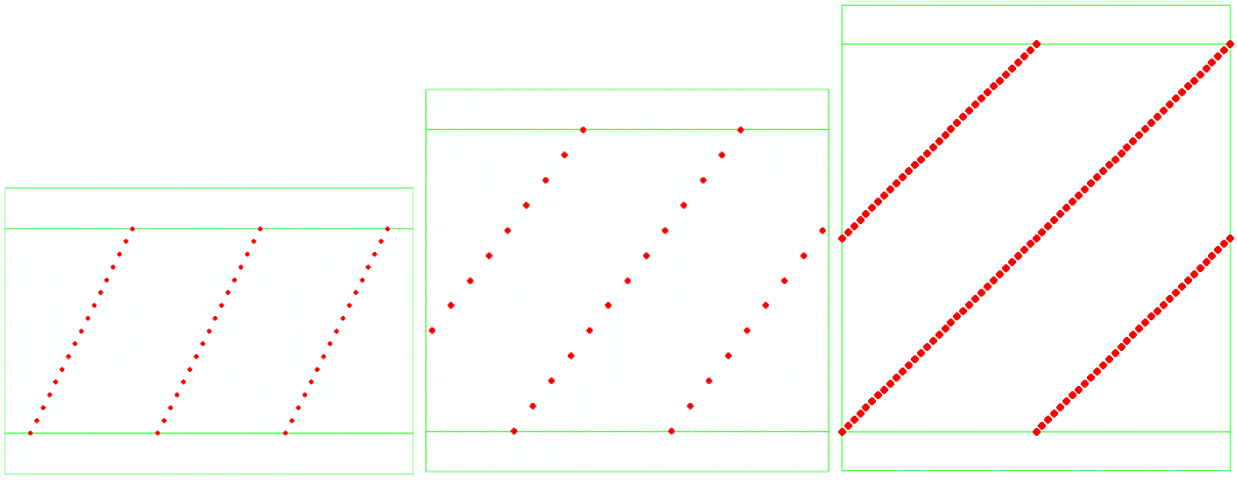

(a) aspect ratio=0.5 (b) aspect ratio=0.75 (c) aspect ratio=1

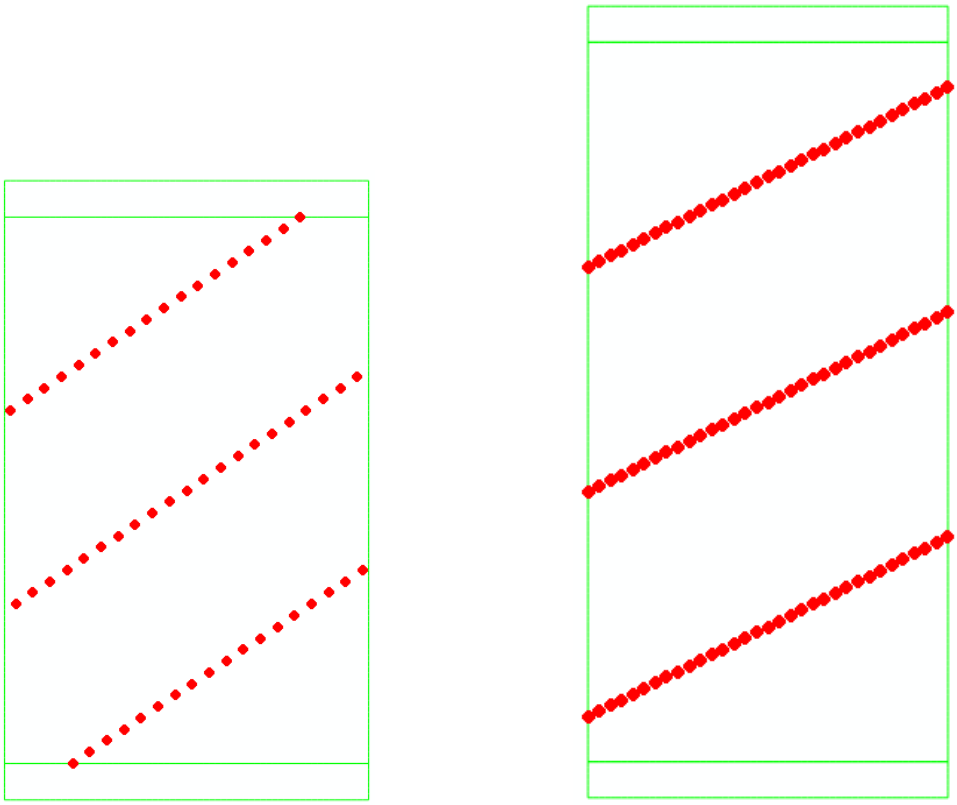

(c) aspect ratio=1.5 (d) aspect ratio=2

Figure 4-4 Quadrisection lines perpendicular to the compressive diagonal

To observe the respective effect of aspect ratio and axial stress, the principal compressive stress curves on the bisection lines were grouped by axial stress of 0, 2 MPa, 5 MPa and 10 MPa (Figure 4-5), and by aspect ratio of 0.5, 0.75, 1, 1.5 and 2 (Figure 4-6). Different colours indicate the five aspect ratios from 0.5 to 2 in Figure 4-5, and differentiate the four axial stresses from 0 to 10 MPa in Figure 4-6. The y- axis denotes the value of the principal compressive stress (0 to 35 MPa). The x- axis indicates the node's horizontal location on a quadrisection line by counting the number of elements between the node and the intersection of the quadrisection line and the compressive diagonal, from bottom/left (negative) to top/right (positive). When the x coordinate

of a node equals zero, it means the node resides on the compressive diagonal as well as its corresponding quadrisection line.

It is worth mentioning that, when the aspect ratio is less than one, the bisection line is shorter than the wall width. That's why in Figure 4-5, the curves with aspect ratio of 0.5 and 0.75 are shorter than the other curves, and in Figure 4-6 the scale of the x- axis in plot (a) and (b) is smaller than that in plot (c), (d) and (e).

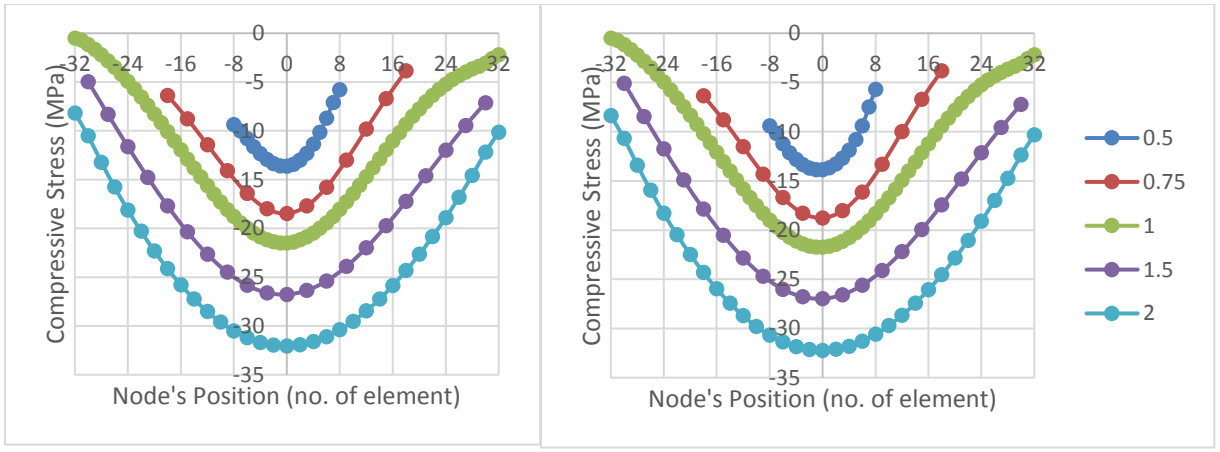

(a) axial stress=0 (b) axial stress=2 MPa

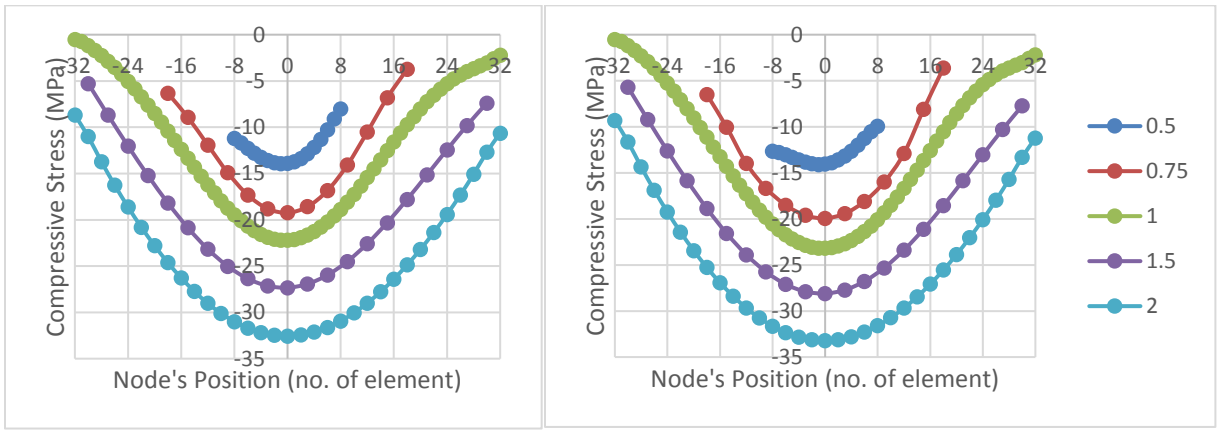

(c) axial stress=5 MPa (d) axial stress=10 MPa

Figure 4-5 Compressive stress on the bisection line (grouped by axial stress) for walls of different aspect ratio (labeled on the right)

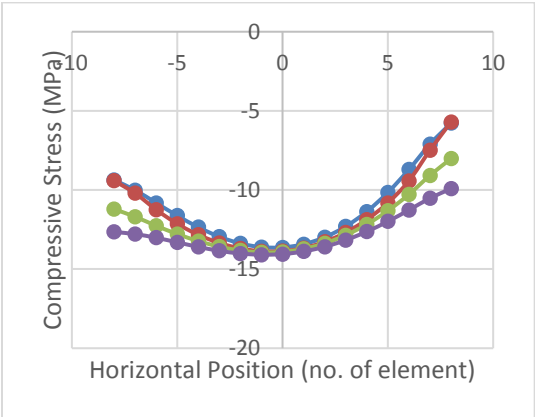

(a) aspect ratio=0.5

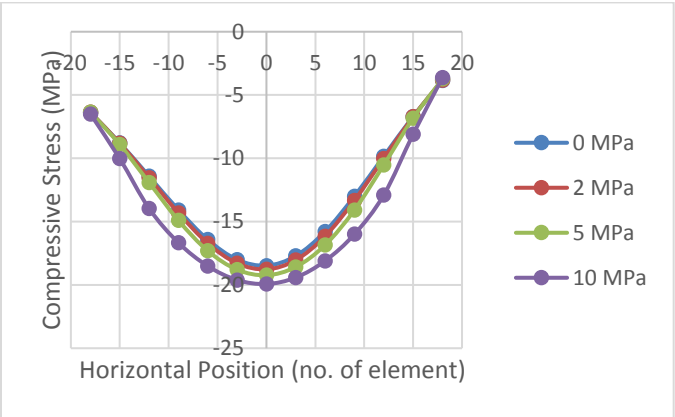

(b) aspect ratio=0.75

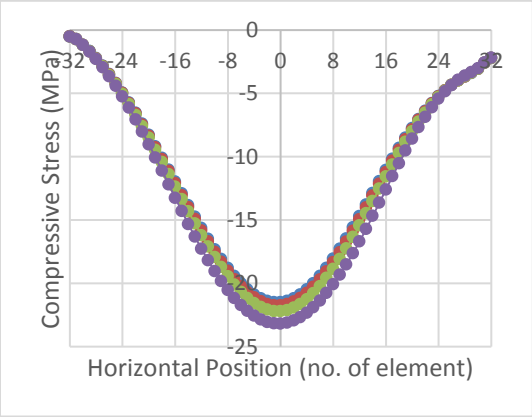

(c) aspect ratio=1

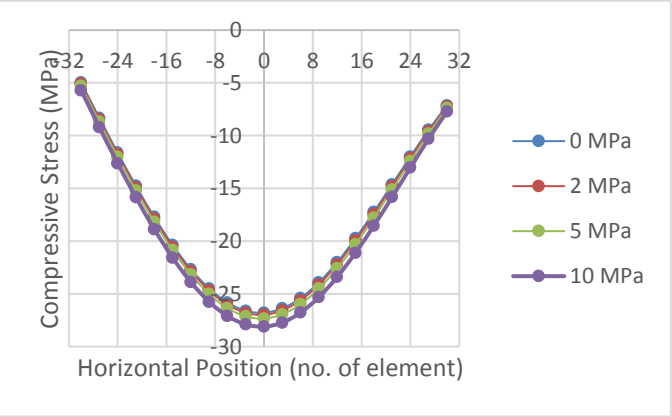

(d) aspect ratio=1.5

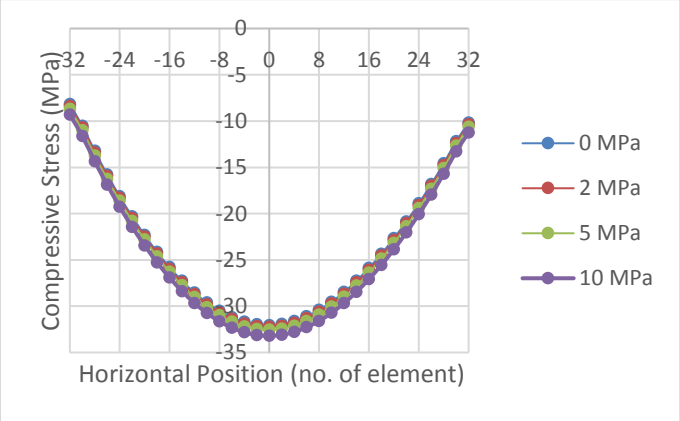

(e) aspect ratio=2

Figure 4-6 Compressive stress on the bisection line (grouped by aspect ratio) when the walls are subject to different axial stresses (labeled on the right).

When observing any plot from Figure 4-5, when the aspect ratio increases, there is a clear increase in the magnitude of the principal compressive stress near the compressive diagonal (when x equals zero). However, when comparing the four plots in Figure 4-5, there is only a very slight increase in the magnitude of the compressive stress with increasing levels of axial stress – indeed the change can be hardly perceived as the data suggest. Even when the stress curves were grouped by aspect ratio in Figure 4-6, the effect of axial stress in each plot was still very limited. These plots indicate that aspect ratio has a much stronger effect than axial stress does when it comes to the stress distribution within the wall.

In the next chapter, the effect of axial stress and aspect ratio will be further discussed when an imaginary void is introduced in the wall using a simple cohesive strength model.

Chapter 5 Cohesive Strength Model and XFEM Crack Visualization

5.1 Cohesive strength model

A simple cohesive strength model was used to investigate the combined effects of axial stress and aspect ratio on the in-plane shear behaviour of masonry walls further. According to Shrive (1983), as shown in Figure 5-1, an imaginary spheroidal void was introduced to the material. The stresses that develop on the surface of the void, at each of the three points A, B, and C, in each of the three directions 1, 2, and 3, in plot (b) can be determined by the principal stresses existing at some distance from the void, denoted as σ_{1a}, σ_{2a}, σ_{3a} in plot (a). For instance, the stresses at point A on the surface of the void can be calculated as expressed in Equation 5-1:

$$\sigma_{11} = 0$$

$$\sigma_{22} = \sigma_{2a} + \frac{1}{14-10\nu}[\sigma_{1a}(-3-15\nu) + \sigma_{2a}(13-5\nu) + \sigma_{3a}(-3+15\nu)] \qquad \text{Eq. 5-1}$$

$$\sigma_{33} = \sigma_{3a} + \frac{1}{14-10\nu}[\sigma_{1a}(-3-15\nu) + \sigma_{2a}(-3+15\nu) + \sigma_{3a}(13-5\nu)]$$

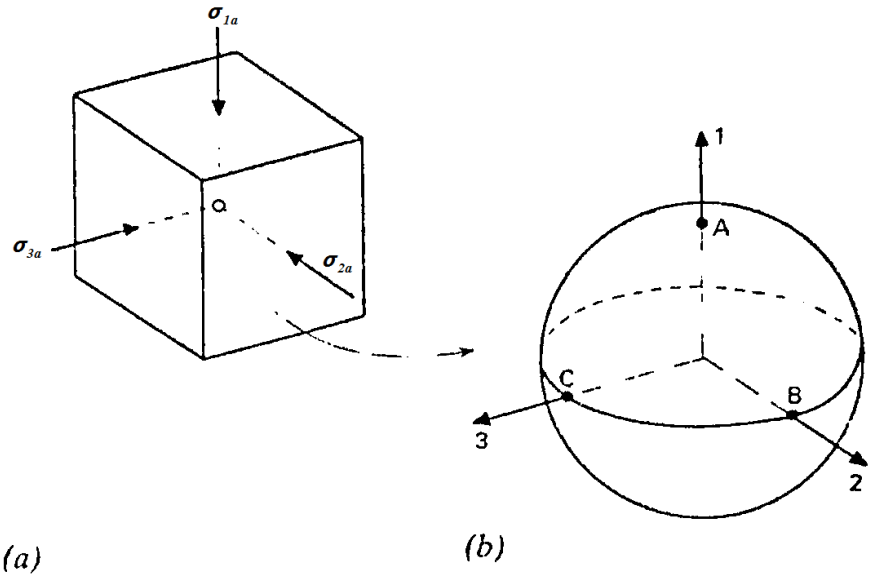

Figure 5-1 Cohesive strength model with a spheroidal void (Shrive (1983))

The cohesive strength model of cracking is based on the idea that once a certain tensile stress is developed in a material, a crack will extend perpendicular to that tensile stress. This criterion is based on the fact that tensile stress is needed to break interatomic bonds: compressing an interatomic bond will not break it. In a compressive stress field (for example, uniaxial compression), there is therefore a need to develop a tensile stress. Voids occur in materials, especially concrete and masonry, and create tension at their surfaces in a macro compression stress field. Thus, if there is uniaxial compression in the 1- direction in Figure 5-1, then tension will develop in the 2- and 3- directions at point A on the spheroidal void. To use the spheroidal void model in the current work, an infinitesimal imaginary void was positioned at the nodes on the three quadrisection lines of and perpendicular to the compressive diagonal (as shown in Figure 4-4 in Chapter 4). Principal stress data required by the Equation 5-1 were obtained from the results of the 20 cases studied in Chapter 4 Section 4.4, where the finite element model was subject to increasing axial stress (0, 2 MPa, 5 MPa and 10 MPa) and shaped with different aspect ratios (0.5, 0.75, 1, 1.5 and 2). Given the principal stresses at the nodes on the three quadrisection lines for each case, the tensile stress at the surface of each void in the direction of the diagonal was determined according to Equation 5-1.

Figure 5-2 presents the stress in the diagonal direction developed at the surface of the voids on the three quadrisection lines. Results from 10 typical cases were plotted, with five aspect ratios and two selected levels of axial stress (0 and 10 MPa). Tensile stress has a positive value, as opposed to compressive stress. The x- axis represents the void's horizontal position on a quadrisection line from bottom/left (negative) to top/right (positive), by counting the number of elements between the void and the zero position (where the quadrisection line intersects the diagonal). Label "middle" refers to the middle quadrisection line, i.e. the bisection line that cuts

the diagonal half, label “top/left” refers to the quadrisection line that is above or to the left of the “middle” line, and label “bottom/right” refers to the quadrisection line beneath or to the right of the “middle” line.

Additionally, the surface stress data at the quadrisection points of the diagonal (when x equals zero) were displayed in Table 5-1 and Table 5-2 for further discussion.

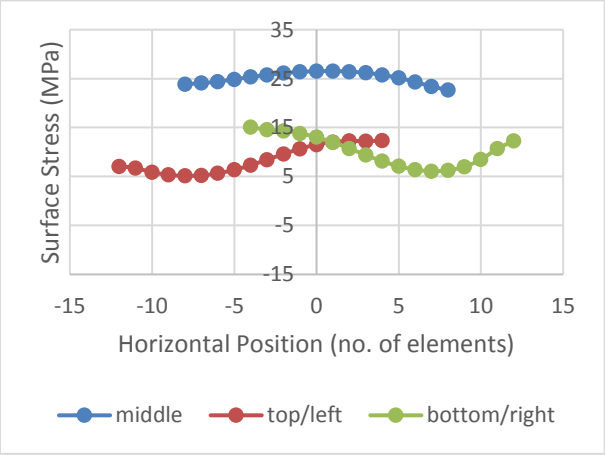

(a) aspect ratio=0.5, axial stress=0

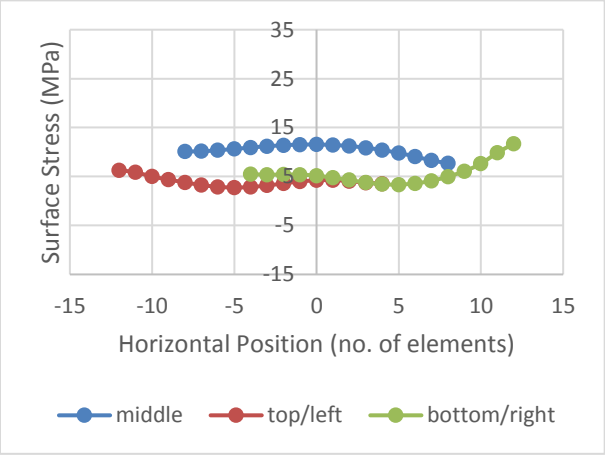

(b) aspect ratio=0.5, axial stress=10MPa

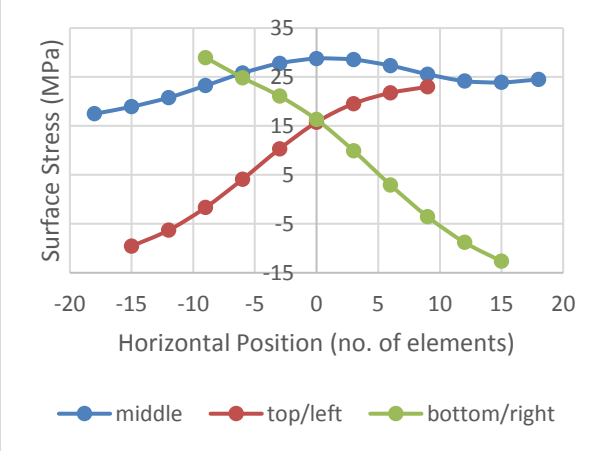

(c) aspect ratio=0.75, axial stress=0

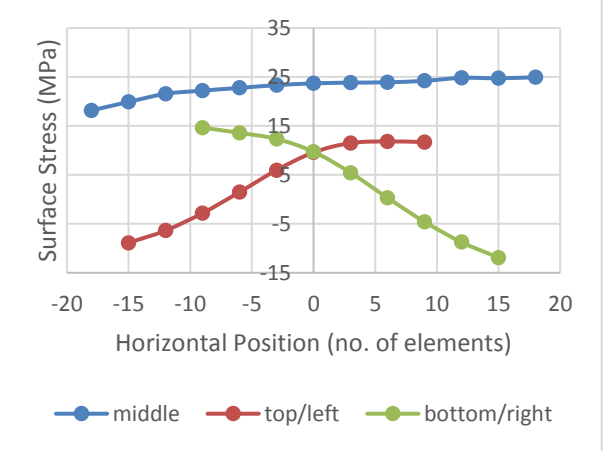

(d) aspect ratio=0.75, axial stress=10 MPa

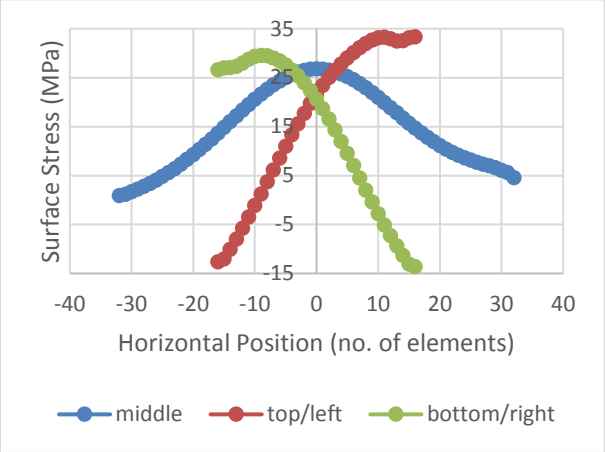

(e) aspect ratio=1, axial stress=0

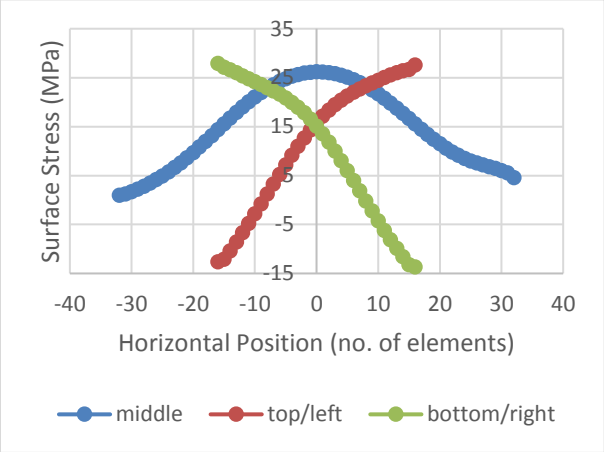

(f) aspect ratio=1, axial stress=10 MPa

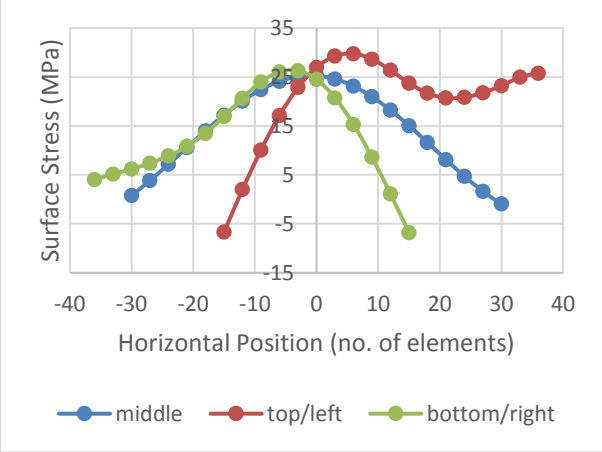

(g) aspect ratio=1.5, axial stress=0

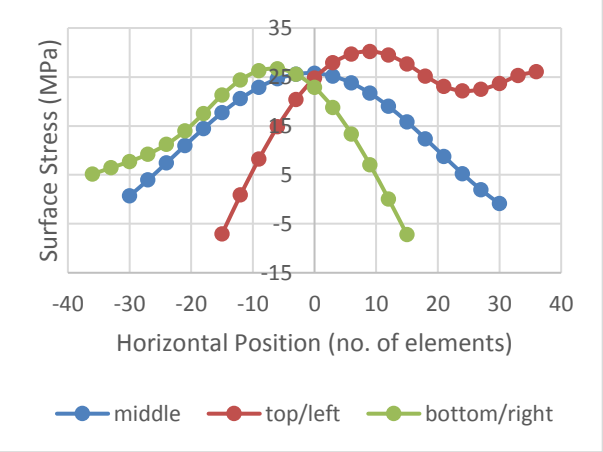

(h) aspect ratio=1.5, axial stress=10 MPa

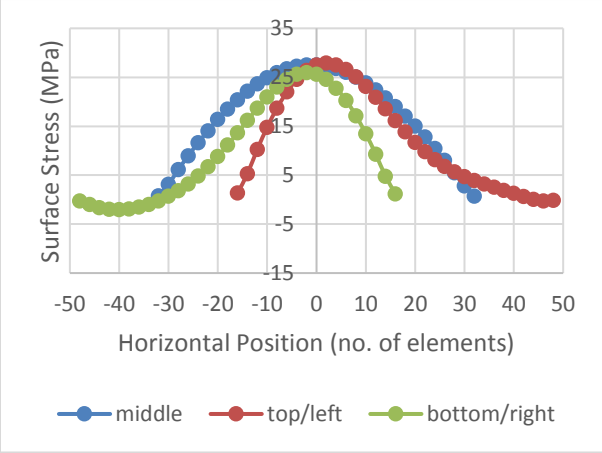

(i) aspect ratio=2, axial stress=0

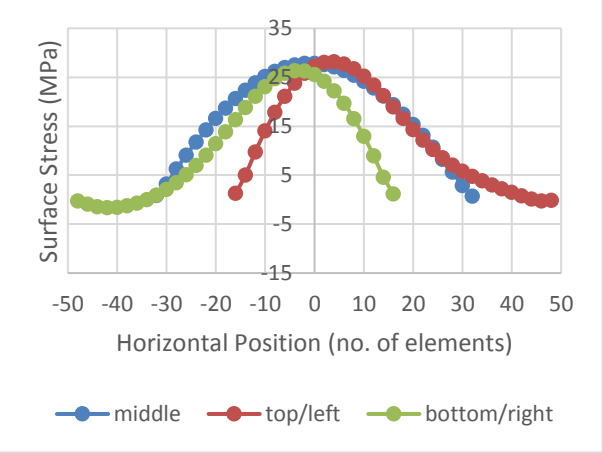

(j) aspect ratio=2, axial stress=10 MPa

Figure 5-2 Surface stress of the voids in the diagonal direction on the quadrisection lines

Observing the plots vertically in Figure 5-2, aspect ratio seems to have an apparent impact on the surface stress of the voids in the diagonal direction. When there is no axial stress, according to Table 5-1 and plots on the left side of Figure 5-2, the tensile stress that has developed at the middle point of the diagonal (the blue dot on the y- axis in Figure 5-2) has a steady value ranging approximately from 25 MPa to 29 MPa, regardless of the varying aspect ratio. In contrast, the tensile stress at the other two quadrisection points (the red and green dots on the y- axis in Figure 5-2) seems to experience a remarkable increase, especially when the aspect ratio is less than 1.5.

It can also be noted that in squat walls, the middle point of the diagonal has the highest tensile stress when compared to the other two quadrisection points. In contrast, in slender walls, tensile stress seems to be of very close high values along the diagonal regardless of the position.

Table 5-1 Surface stress of the voids on the diagonal (axial stress=0)

Surface stress (MPa)	Aspect ratio = 0.5	Aspect ratio = 0.75	Aspect ratio = 1	Aspect ratio = 1.5	Aspect ratio = 2
middle	26.5	28.8	26.8	25.3	27.5
top/left	11.5	15.8	21.7	27.0	27.5
bottom/right	13.0	16.3	20.6	24.5	25.6

Table 5-2 Surface stress of the voids on the diagonal (axial stress=10 MPa)

Surface stress (MPa)	Aspect ratio = 0.5	Aspect ratio = 0.75	Aspect ratio = 1	Aspect ratio = 1.5	Aspect ratio = 2
middle	11.5	23.7	26.2	25.8	27.9
top/left	4.2	9.6	15.8	24.8	27.3
bottom/right	5.2	9.7	15.1	22.9	25.6

On the other hand, the level of axial stress decreases the surface stress of the void to some extent. When comparing the plots horizontally in Figure 5-2, it can be concluded that increasing axial stress decreases the surface stress of the voids. However, this effect is less notable when the aspect ratio is larger than 1.

When comparing Table 5-2 with Table 5-1, the application of axial stress (i.e. increasing axial stress from 0 to 10 MPa) decreases the surface stress effectively in squat walls with low aspect ratio (nearly 60% off when the aspect ratio equals 0.5), but becomes less effective in slender walls with high aspect ratio. Furthermore, when comparing the five plots on the right side of Figure 5-2 (applied axial stress equals 10 MPa compression) with the five plots on the left side (no axial stress applied), the decrease in the surface stress can be observed near the x=0 line (which represents the diagonal of the panel), but can be hardly seen when it's far from the x=0 line even in walls with low aspect ratio. This means the level of axial stress has sufficient impact on the area close to the diagonal, but has neglectable impact on the area far from the diagonal. In terms of wall strength, if a set tensile stress is needed to initiate cracking, axial stress has little effect for high aspect ratios, but will require a distinctly higher shear load to cause failure of a squat wall, as has been observed in experimental tests.

In addition, it can be observed from Figure 5-2 that the maximum tensile stress which is likely to initiate a crack is located on or close to the diagonal - mostly at the centre of the wall. Therefore, in the next section, a circular void is introduced to the centre of the wall to see whether a crack would initiate in the middle of the wall as indicated by the cohesive strength model, and whether the crack would propagate in the diagonal direction as widely observed in experiments.

5.2 Crack visualization with XFEM modelling technique

The XFEM (extended finite element method) modelling technique offered by Abaqus allows a crack to occur in an element interior, without predefining a crack location and path (along element boundaries) for the crack to initiate and progress. Given this advantage, the XFEM approach was adopted to visualize the potential diagonal cracking of an unreinforced masonry wall subject to in-plane lateral load.

A circular void was introduced at the centre of a 100 mm$\times$100 mm square masonry panel. An XFEM type crack was assigned to the region of the entire panel without specifying the crack initiation location. The material model for the masonry panel includes isotropic elastic material properties (Young's modulus=10,000 MPa, Poisson's ratio=0.2), as well as damage parameters for crack initiation and evolution.

The failure mechanism consists of a damage initiation criterion and a damage evolution criterion. A typical linear traction-separation cohesive response is shown in Figure 5-3. A maximum principal stress initiation criterion was specified so that degradation of the cohesive response will begin when maximum principal stress in an element reaches 2 MPa. The direction of the crack is perpendicular to the maximum principal stress direction. The damage evolution law describes the degrading rate of the cohesive stiffness, and can be defined based on either the effective separation or the fracture energy (the area under the traction-separation curve). This evolution criterion will be discussed in Section 5.2.3.

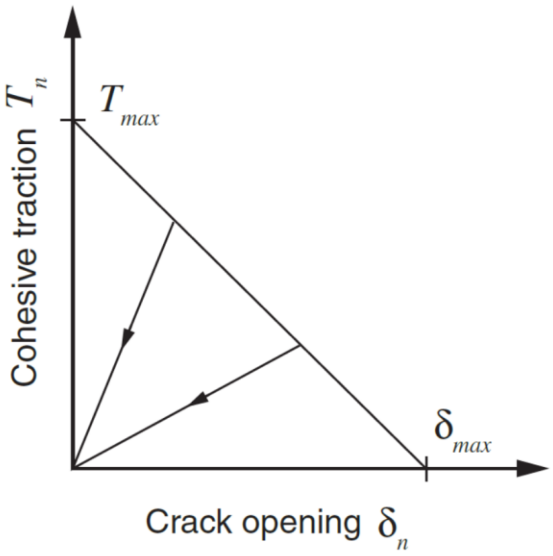

Figure 5-3 Linear traction-separation cohesive response (Abaqus (2014))

No bond beams were attached to the panel. Therefore, lateral load was applied to the top surface of the panel in the form of a horizontal displacement. And the bottom surface of the panel was restrained both horizontally and vertically.

To optimize the model for crack visualization, the void radius, mesh density and damage evolution criterion are considered as variables and are discussed in the following.

5.2.1 Radius of the void.

The radius of the central void was chosen to be 0.2 mm, 1 mm and 5 mm, where the side length of the square panel is 100 mm. As shown in Figure 5-4, the crack initiates and evolves well along the diagonal when the radius of the void equals 1 mm and 5 mm. However, when the void radius equals 0.2 mm, a major crack develops into the top left part of the panel, with unexpected “garbage” cracks spread from the centre of the panel in the bottom right part of the panel. The void radius of 0.2 mm was thus eliminated as this model failed to initiate the crack with a clear direction in the bottom right part of the panel. This lack of distinct cracking eventually led to the evolution of the undesirable “garbage” cracks.

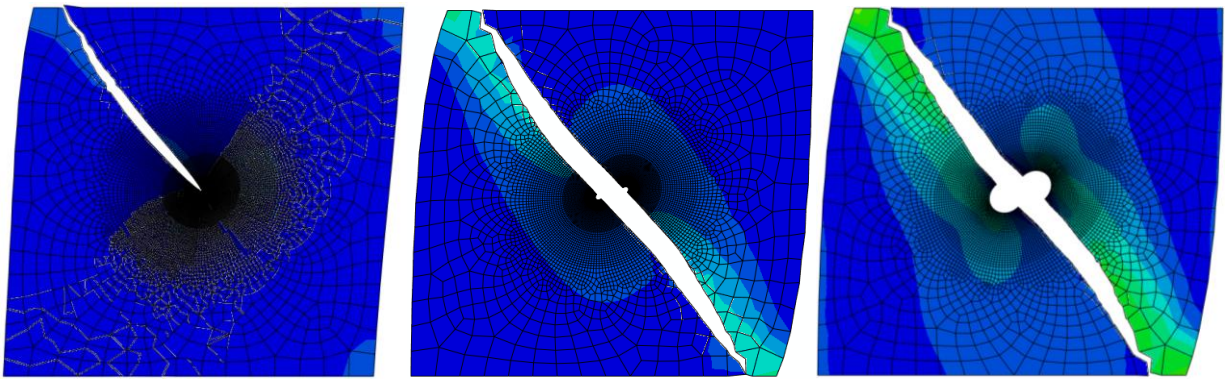

(a) radius of the void=0.2 mm (b) radius of the void=1 mm (c) radius of the void=5 mm

Figure 5-4 Effect of void radius on XFEM cracks (1)

As shown in Figure 5-5, when the mesh was made more dense, slight "garbage" cracks appeared at the anti-diagonal corners of the panel with void radius of 1 mm, whilst the panel with void radius of 5 mm still produced a crack along the diagonal as expected. Given these results, 5 mm appears to be the best radius choice for the central void. Therefore, subsequent models with void radius of 5 mm were used to examine the influence of mesh density and the damage evolution criterion.

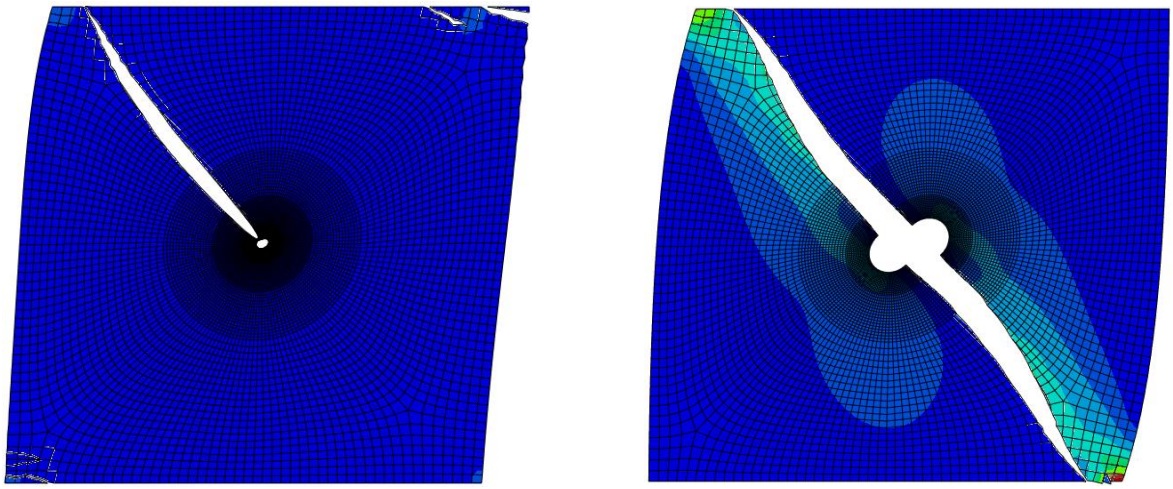

(a) radius of the void=1 (b) radius of the void=5

Figure 5-5 Effect of void radius on XFEM cracks (2)

5.2.2 Mesh density.

A concentric circular partition with radius of 20 mm was created to refine the mesh in the central void area where cracks initiate. The mesh density of the rest part of the panel (area away from the void) is varied from coarse to fine by adjusting the number of elements on the four edges of the panel.

XFEM cracks generated in the panels with different mesh densities are shown in Figure 5-6. All the cracks initiated from the central void and evolved mainly along the diagonal as expected. “Garbage” cracks started to appear from plot (d) when there are 30 elements defined on each of the four edges of the panel. It can be concluded that refined mesh tends to cause “garbage” cracks and therefore should be avoided for the area away from the void.

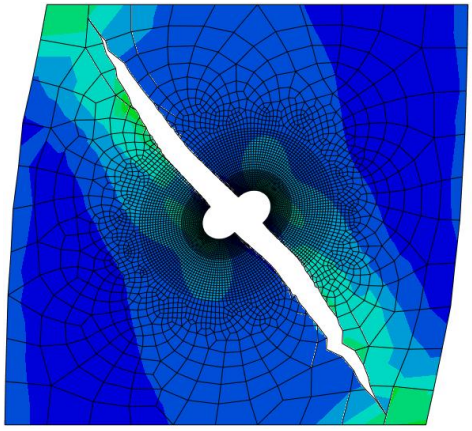

(a) number of elements per edge=10

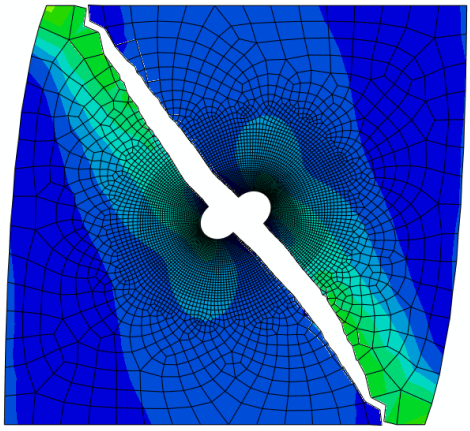

(b) number of elements per edge=15

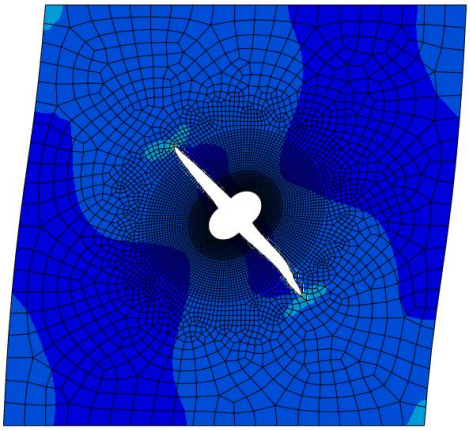

(c) number of elements per edge=20

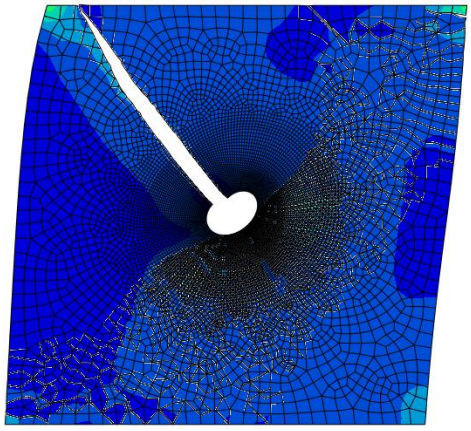

(d) number of elements per edge=30

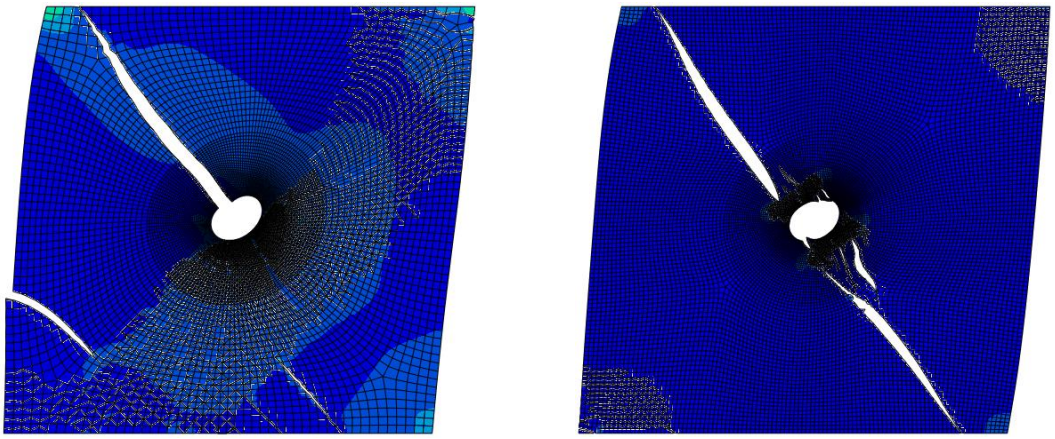

(e) number of elements per edge=50 (f) number of elements per edge=100

Figure 5-6 Effect of mesh density on XFEM cracks

5.2.3 Damage evolution criterion.

After damage initiation, the displacement-type damage evolution criterion defines damage as a function of the total or plastic displacement. A total displacement of 0.01 mm was given as required for the displacement damage evolution.

On the other hand, the energy-type damage evolution criterion defines damage in terms of the energy required for failure. The dependence of the fracture energy on the mode mix was specified using the BK (Benzeggagh-Kenane) form, as expressed in Equation 5-2 (Benzeggagh and Kenane (1996)).

$$G_n^C + (G_s^C - G_n^C)\left(\frac{G_S}{G_T}\right)^{\eta} = G^C \qquad \text{Equation 5-2}$$

where $G_S = G_s + G_t$, $G_T = G_n + G_s + G_t$, and η is a cohesive property parameter.

G_n, G_s, and G_t are the work done by the tractions and their corresponding separations in the normal, first shear, and second shear directions. The critical fracture energies in the normal and shear directions were specified as 0.1 N/mm, and η was given 2.284. According to Abaqus

(2014), when fracture energies in the first and second shear directions are the same, the response is insensitive the value of η.

Both displacement-type and energy-type damage evolution criteria were tested for panels with different mesh densities. The results are shown in Figure 5-7.

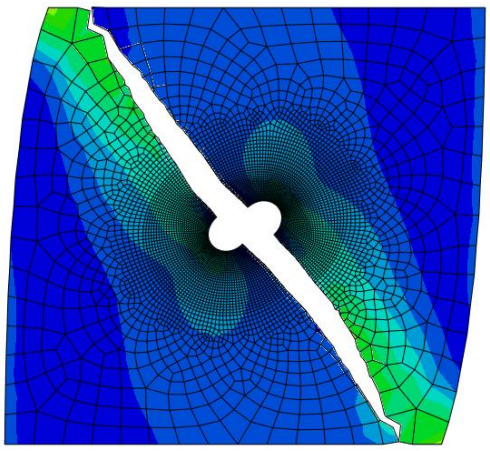

(a) displacement damage evolution

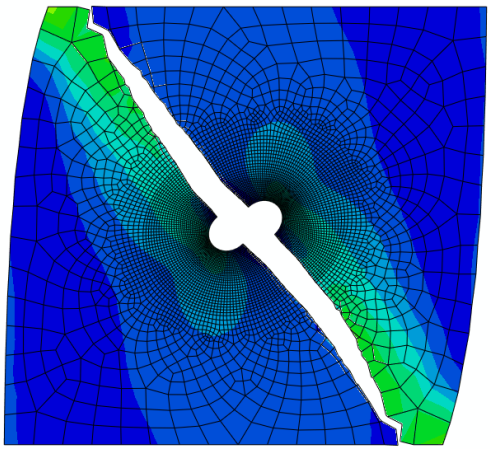

(b) energy damage evolution

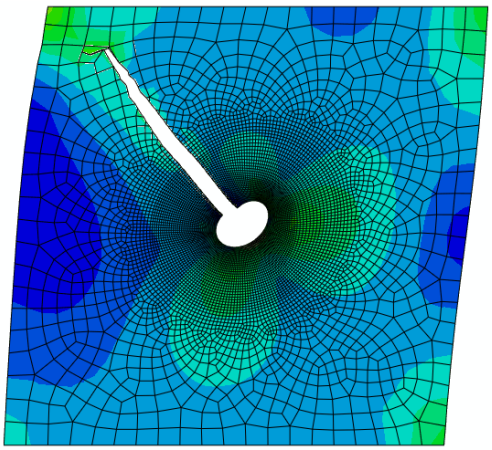

(c) displacement damage evolution

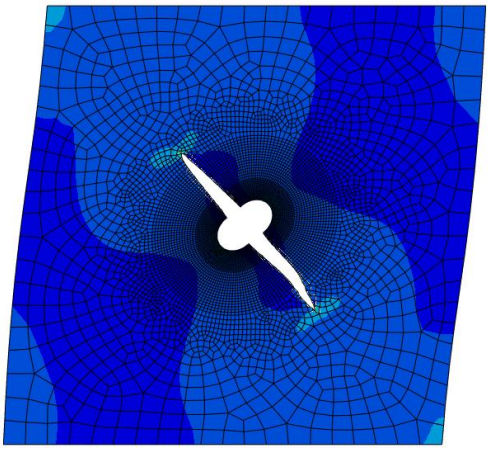

(d) energy damage evolution

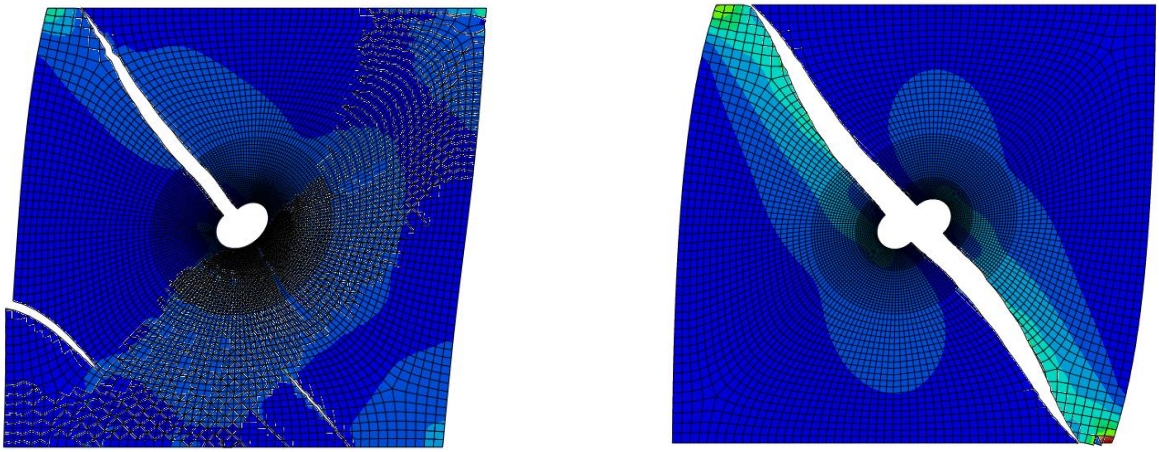

(e) displacement damage evolution (f) energy damage evolution

Figure 5-7 Effect of damage evolution criterion on XFEM cracks

Comparing plot (a) and plot (b) in Figure 5-7, the difference can hardly be seen between the two damage evolution criteria when the mesh density is low. However, comparisons between plot (c) and plot (d), and plot (e) and plot (f) indicate that when the mesh becomes more dense, cracks grow unstably with the displacement damage evolution criterion.

In a nutshell, when visualizing a diagonal shear crack in masonry using the XFEM modelling technique, the energy damage evolution criterion is recommended, together with a void radius of 5 mm (void diameter is 1/10 the width of the panel in this study) and low to medium mesh density.

Chapter 6 Diagonal Strut Width

6.1 Diagonal compression strut

When discussing the effects of different boundary conditions and load application methods in Chapter 3, a diagonal compression strut was found in the contour plots of the minimum principal stress (i.e. principal compressive stress) with adjusted display stress limits. Since the high compression zone (the black colour area) is basically parallel to the diagonal, the stress in the diagonal direction was then plotted to "straighten" the diagonal compression strut, as illustrated in Figure 6-1.

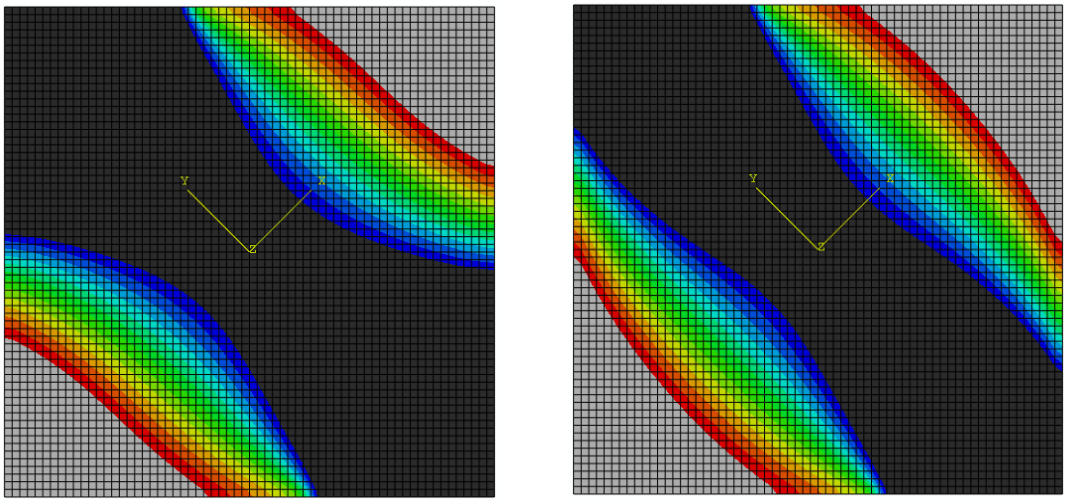

(a) Minimum principal stress (b) Stress in the diagonal direction

Figure 6-1 Principal compression and "straightened" diagonal strut

The minimum principal stress data and stress data in the diagonal direction along the anti-diagonal line of a square wall were extracted and plotted in Figure 6-2. It can be seen from the plot that the maximum compressive stress on the anti-diagonal happens at the centre node of wall, though difference between the two data sets can be hardly observed. In fact, among the 65 nodes on the anti-diagonal of the wall, 45 nodes in the middle area (accounting for 70% of the

line) have differences in stress lower than 5% when comparing the two stress data sets. Therefore, the "straightening" of the diagonal strut seems reasonable and effective.

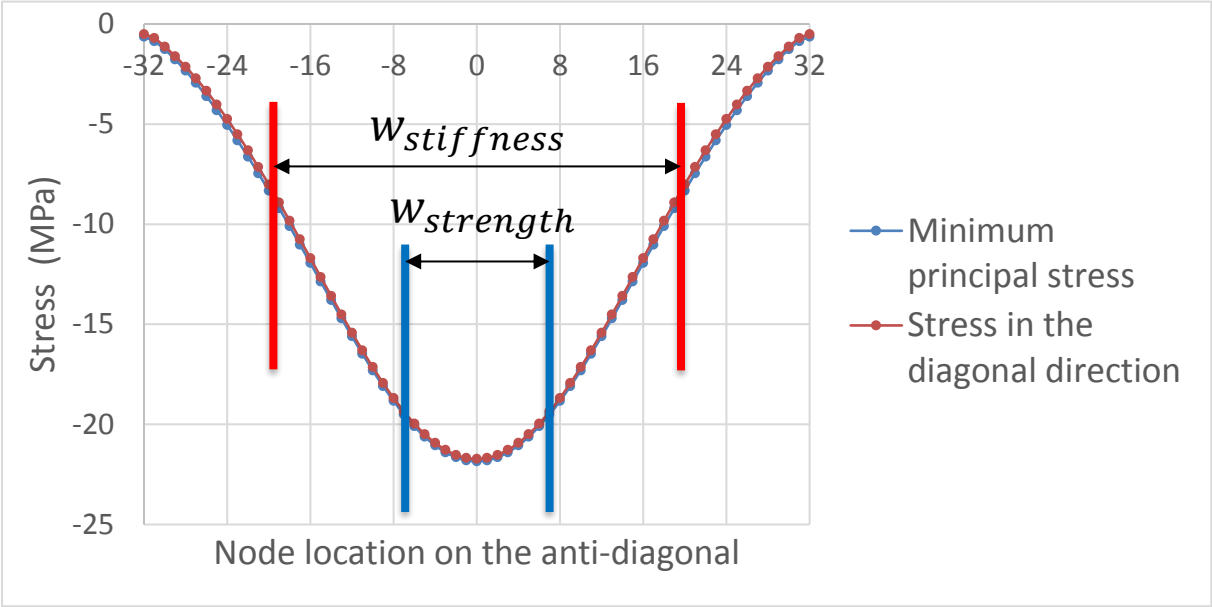

Figure 6-2 Stress data along the anti-diagonal

Next, the display stress limits (used to define the boundaries of the diagonal strut as a percentage of the maximum compressive stress on the anti-diagonal) need to be readjusted to formalize the width of the diagonal strut. Comparing plots (a), (b) and (c) in Figure 6-3, when the red contours are fixed to be 20% of the peak compressive stress, there is little difference between the shapes of the black colour zone bounded by the blue contours. 90% of the peak compressive stress was chosen to be the upper stress limit which determines where the blue contours locate. Comparing plots (d), (e) and (f) in the second row in Figure 6-3, a difference can be observed between varied lower stress limits. 40% of the peak compressive stress was chosen as the lower stress limit which determines the location of the red contours.

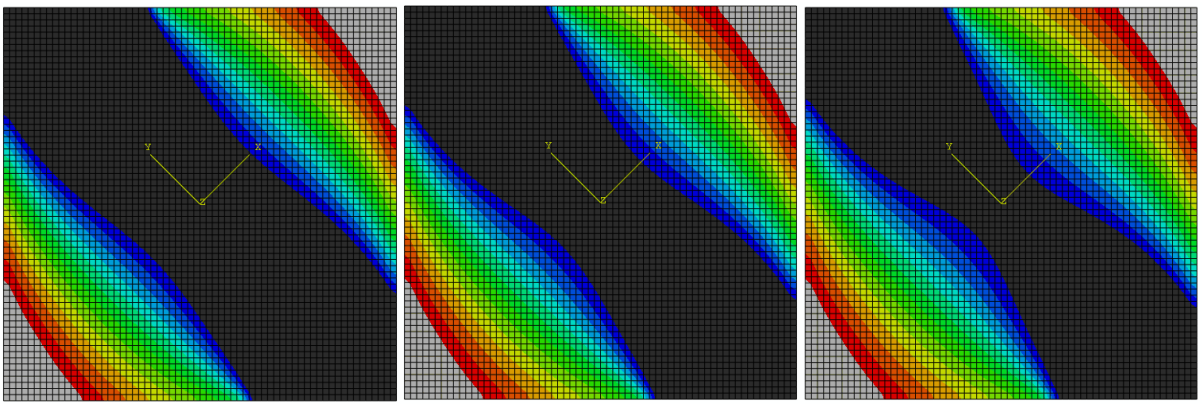

(a) 20% and 85% (b) 20% and 90% (c) 20% and 95%

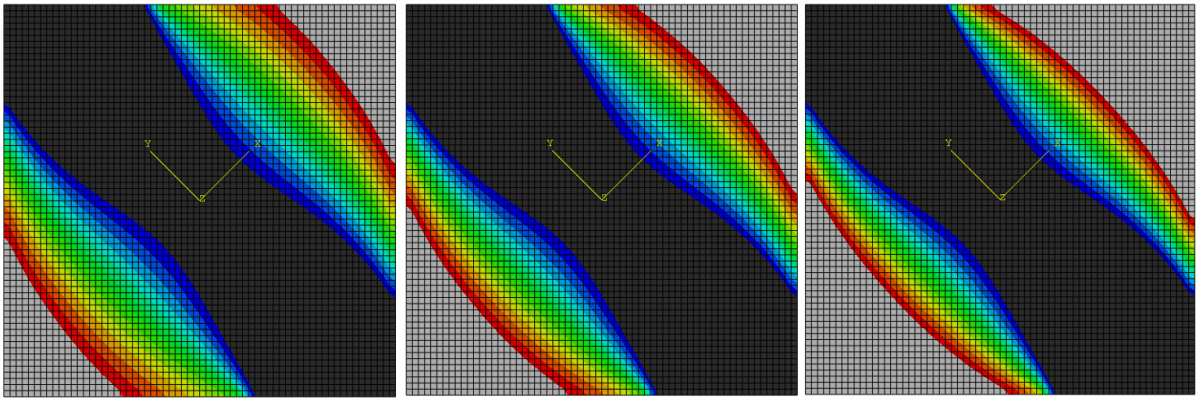

(d) 30% and 90% (e) 40% and 90% (f) 50% and 90%

Figure 6-3 Stress limits

Finally, a "straightened" and well-sized diagonal compression strut with 40%-90% stress limits is formalized (refer to plot (e) in Figure 6-3). The compressive stress in the black zone, bounded by the blue contours, is 90% or more of the peak compressive stress on the anti-diagonal and therefore this zone is expected to be where cracking is most likely to occur. The zone bounded by the red contours, which has compressive stress of 40% or higher of the peak stress, represents the portion of the wall that bears most of the compressive stress caused by the lateral load and therefore contributes to the stiffness of the wall.

6.2 Effects of aspect ratio and axial stress

Figure 6-4 reveals how the compression strut is affected by wall aspect ratio and applied axial load. It can be observed vertically from the plots that as the aspect ratio increases from 0.5 to 2, the directions of both the 90%-peak strut (the black zone) and the 40%-peak strut (the rainbow colour zone) change gradually in an anticlockwise manner (note, for axial stress of zero for example, how the black zone touches the top surface almost entirely for an aspect ratio of 0.5, but slowly extends down the left vertical side as the aspect ratio is increased). On the other hand, when the axial stress is increased from 0 to 10 MPa, the width of the 90%-peak strut is widened and the direction of the strut slightly turns clockwise (more notable in the walls with low aspect ratios).

As the aspect ratio is increased, more of the anti-diagonal corners is released from the contact with the bond beams (hidden from view). The compression is subsequently borne by a smaller portion of the wall. For the walls with high aspect ratio, the slope of the compression strut is already steep, so the addition of axial load does not significantly change the strut geometry.

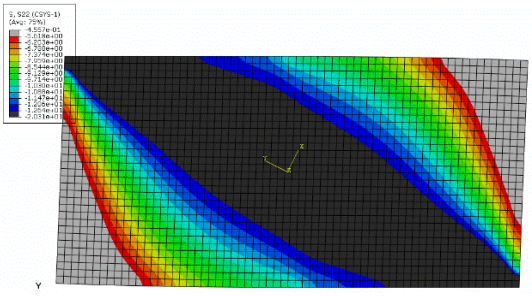

(a) aspect ratio=0.5, axial stress=0

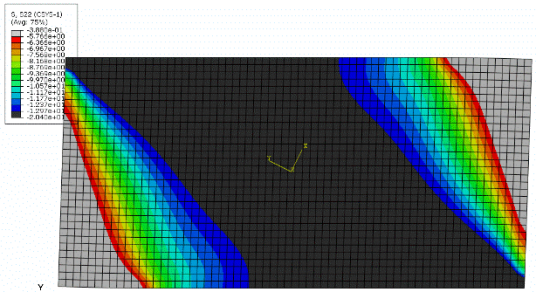

(b) aspect ratio=0.5, axial stress=10MPa

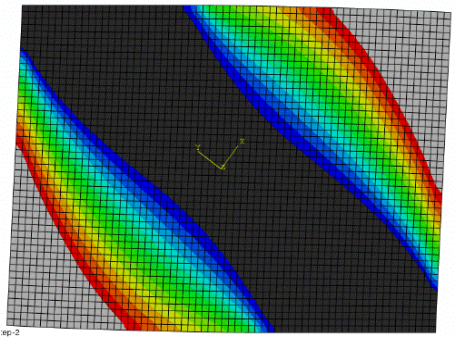

(c) aspect ratio=0.75, axial stress=0

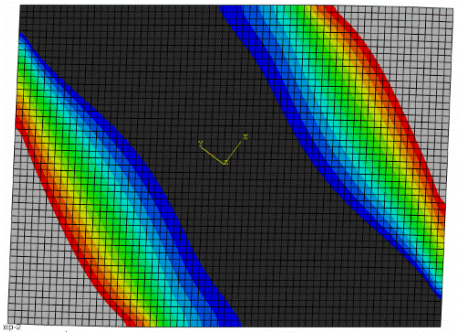

(d) aspect ratio=0.75, axial stress=10MPa

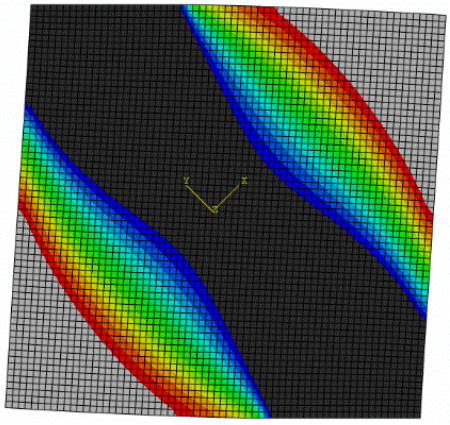

(e) aspect ratio=1, axial stress=0

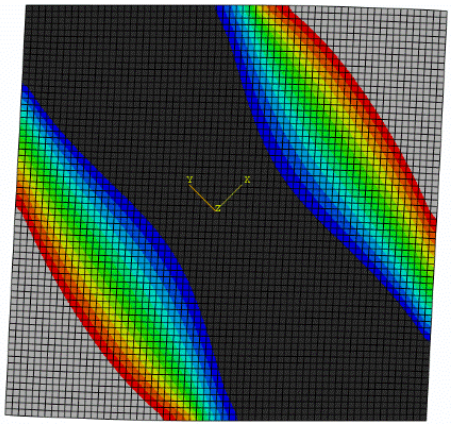

(f) aspect ratio=1, axial stress=10MPa

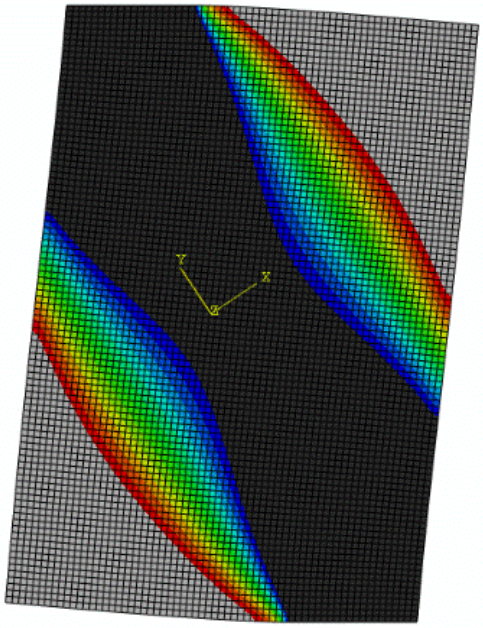

(g) aspect ratio=1.5, axial stress=0

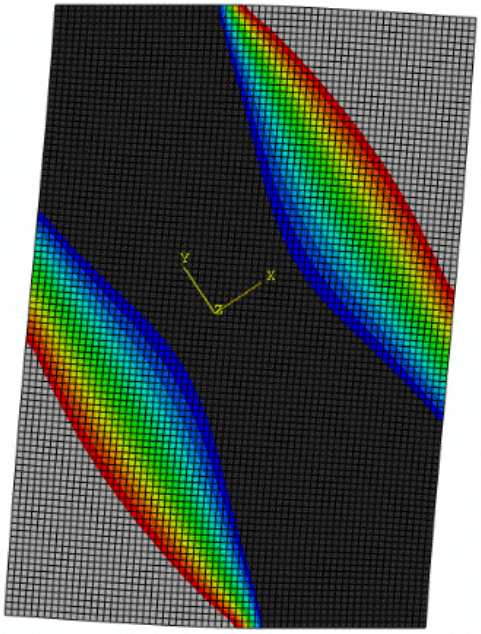

(h) aspect ratio=1.5, axial stress=10MPa

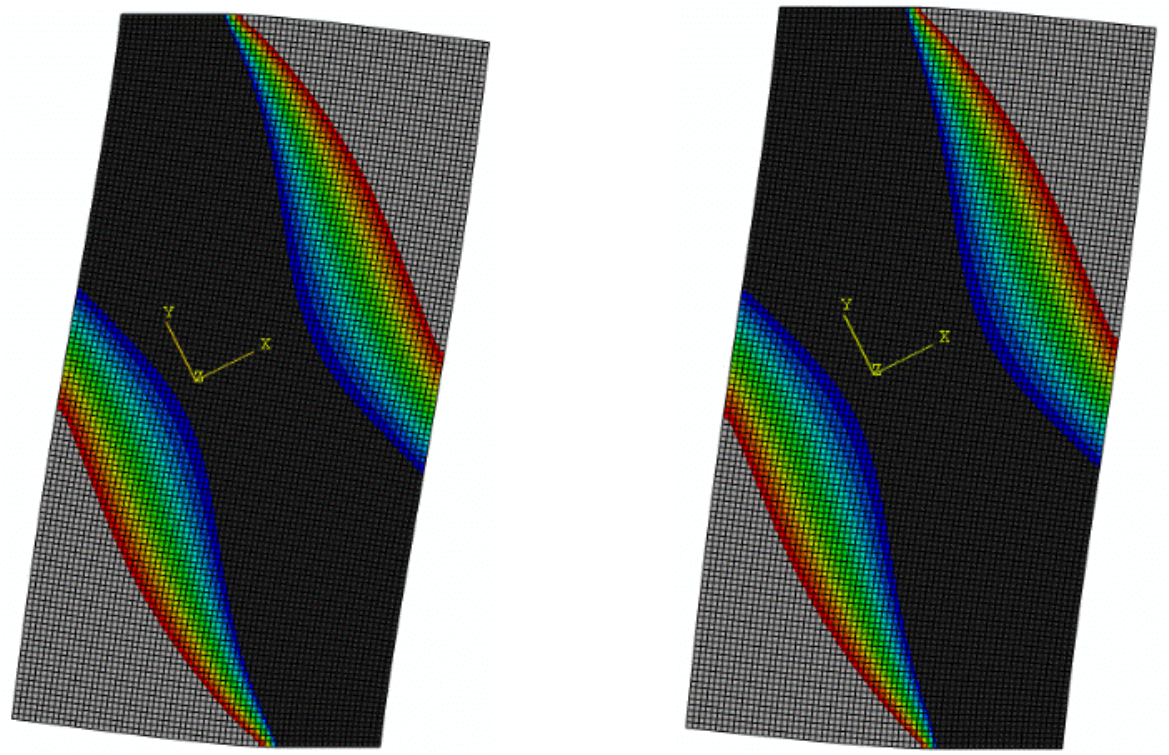

(i) aspect ratio=2, axial stress=0 (j) aspect ratio=2, axial stress=10MPa

Figure 6-4 Compression strut in walls with varied aspect ratios and axial stresses

6.3 Comparison to the Canadian Masonry Design Standard

6.3.1 Diagonal strut model.

The diagonal strut model was first proposed by Polyakov (1957) to simplify infill walls. The idea was to replace the infill masonry with an equivalent compressed diagonal strut, as shown in Figure 6-5. Since then, this model and its variations have been widely adopted in research on infill masonry walls, and many studies have been dedicated to suggesting equations for the diagonal strut width which affects the stiffness and strength of the infill wall.

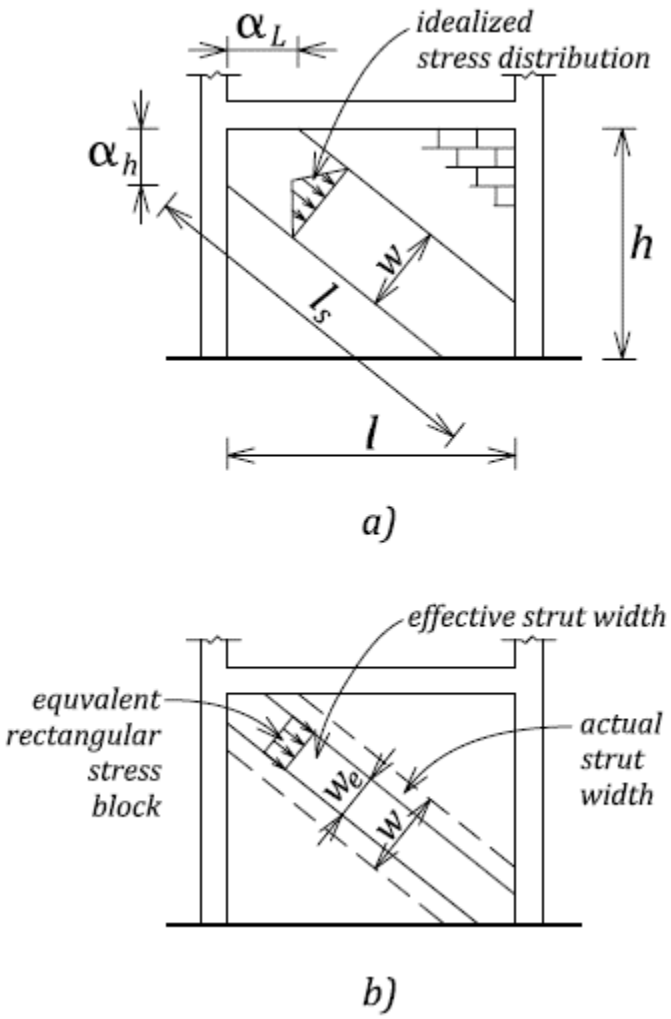

Figure 6-5 Diagonal Strut Model (Anderson and Brzev (2009))

The empirical equation in the Canadian Masonry Design Standard (CSA S304-14) Clause 7.13.3.3 determines the diagonal strut width as follows:

$$w = \sqrt{{\alpha_h}^2 + {\alpha_L}^2} \qquad \text{Equation 6-1}$$

where α_h and α_L are vertical and horizontal contact length between the frame and the diagonal strut, respectively, and

$$\alpha_h = \frac{\pi}{2}\sqrt[4]{\frac{4E_f I_c h}{E_m t_e \sin 2\theta}} \qquad \text{Equation 6-2}$$

$$\alpha_L = \pi \sqrt[4]{\frac{4E_f I_b l}{E_m t_e \sin 2\theta}} \qquad \text{Equation 6-3}$$

where E_m, E_f = moduli of elasticity of the infill wall and frame material, respectively

I_c, I_b = moments of inertia of the column and the beam of the frame, respectively

h, l = height and length of the infill wall, respectively

t_e = thickness of the wall

θ = $\tan^{-1}\frac{h}{l}$

The effective diagonal strut width, w_{eff}, for the calculation of the compressive strength of the diagonal strut is determined as:

$$w_{eff} = w/2 \qquad \text{Equation 6-4}$$

And, w_{eff} should not exceed one quarter of the strut length $l_d = \sqrt{h^2 + l^2}$.

Since the abovementioned diagonal strut model is usually used to design infill walls that are contained within a frame confining the shape of the wall, a new finite element model was created to include a frame partitioned out of the masonry wall as shown in Figure 6-6. The Young's modulus and Poisson's ratio of the frame are defined with the same values of the material properties of the masonry panel. The lateral shear load is applied to the top surface of the bond beam as surface traction, so that the five walls (with varied aspect ratios but same length of the wall which is 3000 mm) receive the same magnitude of shear load. The bottom beam is fixed, and the top surface of the top beam is constrained vertically to simulate displacement-controlled axial loading.

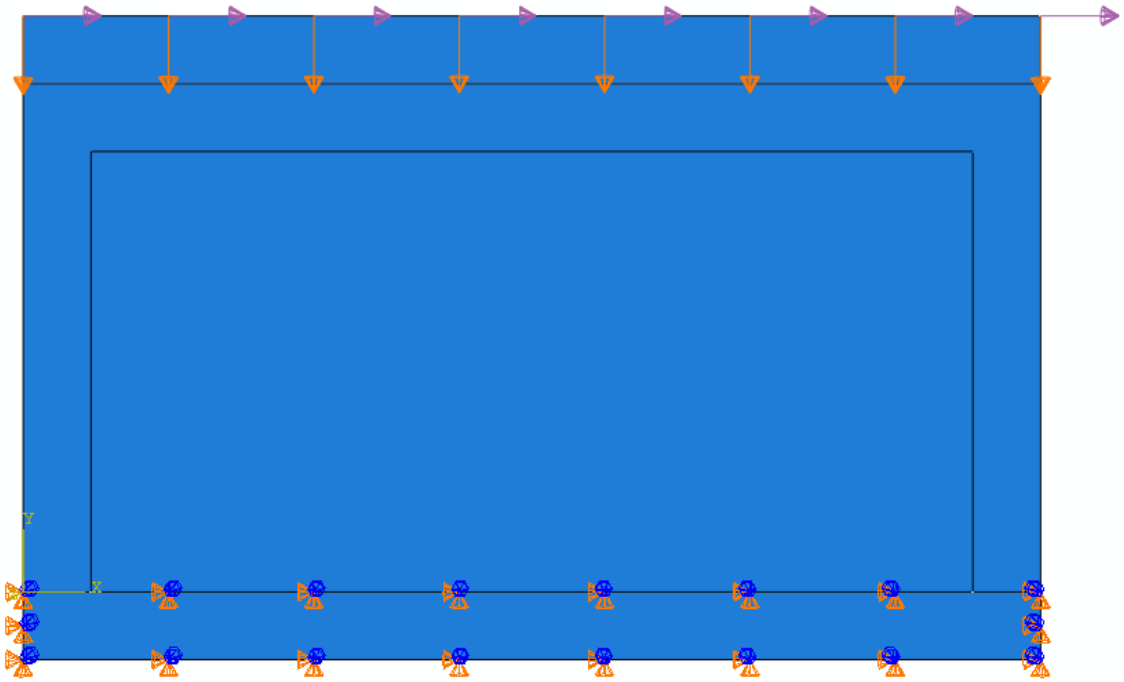

Figure 6-6 Infill wall model (aspect ratio=0.5)

6.3.2 Width ratios for strength and stiffness.

The manual estimation of the diagonal strut widths for strength and stiffness is done by drawing approximate lines on the "straightened" strut plots. Figure 6-7 illustrates an example of how strut widths for strength and stiffness were estimated, where the red lines confine the strength width and the blue lines form the stiffness width. The display stress limits are kept the same to be 40%-90% of the peak compressive stress on the anti-diagonal, the value of which varies from wall to wall. To improve convenience of measurement, the contour plots are displayed with undeformed shape.

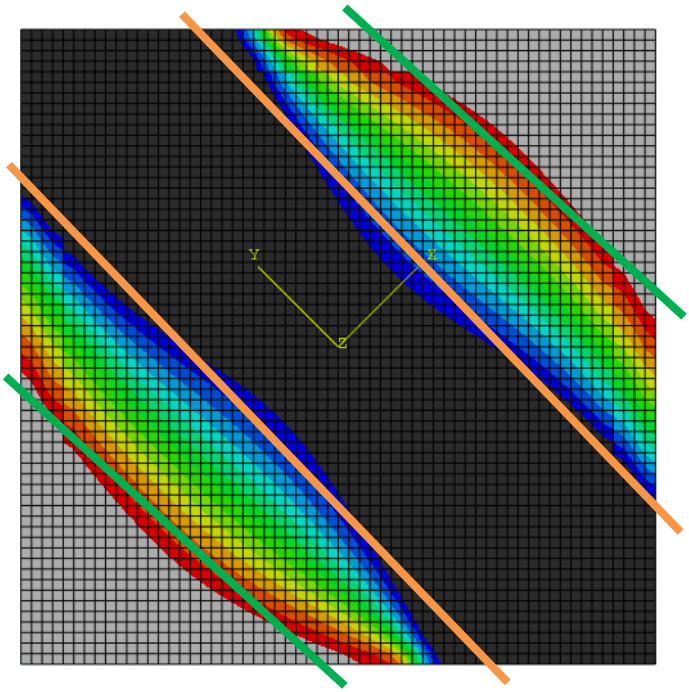

Figure 6-7 Manual estimation of strut widths (aspect ratio=1, axial stress=0)

The strength width $w_{strength}$ (distance between the red lines), stiffness width $w_{stiffness}$ (the distance between the blue lines), and length of the wall L were manually measured from the compression strut plots. Both strength width and stiffness width were then divided by the length of the wall to obtain their respective width ratio, i.e. $\frac{w_{strength}}{L}$ and $\frac{w_{stiffness}}{L}$.

The other set of width ratios for strength and stiffness were obtained by dividing the effective diagonal strut width w_{eff} (calculated from Equation 6-4) and the diagonal strut width w (calculated from Equation 6-1) by the length of the wall, respectively. Parameters required by the equations and the width ratio results are recorded in Table 6-1, Table 6-2, and Table 6-3. The width ratios for strength and stiffness for both the finite element model and the Canadian Masonry Design Standard are plotted in Figure 6-8.

Table 6-1 Width ratios for strength and stiffness (axial stress=0)

Aspect ratio	Principal compressive stress (MPa)	40% (MPa)	90% (MPa)	Length. wall (cm)	Width. strength (cm)	Width ratio. strength	Width. stiffness (cm)	Width ratio. stiffness
0.5	-16.1	-6.4	-14.5	16.1	4.3	0.27	12.5	0.78
0.75	-19.1	-7.7	-17.2	11.55	3.1	0.27	9.4	0.81
1	-21.7	-8.7	-19.6	9	2.6	0.29	7.7	0.86
1.5	-27.2	-10.9	-24.4	6.25	2.1	0.34	5.9	0.94
2	-33.1	-13.2	-29.8	4.8	1.85	0.39	4.9	1.02

Table 6-2 Width ratios for strength and stiffness (axial stress=10 MPa)

Aspect ratio	Principal compressive stress (MPa)	40% (MPa)	90% (MPa)	Length. wall (cm)	Width. strength (cm)	Width ratio. strength	Width. stiffness (cm)	Width ratio. stiffness
0.5	-20.2	-8.1	-18.2	16.1	6.9	0.43	12.7	0.79
0.75	-22.3	-8.9	-20.1	11.55	3.7	0.32	9.25	0.80
1	-24.0	-9.6	-21.6	9	2.8	0.31	7.7	0.86
1.5	-28.5	-11.4	-25.7	6.25	2.2	0.35	6	0.96
2	-34.1	-13.6	-30.7	4.8	1.9	0.40	5.1	1.06

Table 6-3 Width ratios for strength and stiffness (CSA S304-14)

Aspect ratio	Height. panel (mm)	Length. panel (mm)	$l_d/4$ (mm)	w_{eff} (strength) (mm)	Width ratio. strength	w (stiffness) (mm)	Width ratio. stiffness
0.5	1300	2600	726.7	519.9	0.20	1039.8	0.40
0.75	2050	2600	827.7	504.6	0.19	1009.2	0.39
1	2800	2600	955.3	509.0	0.20	1018.1	0.39
1.5	4300	2600	1256.2	537.1	0.21	1074.3	0.41
2	5800	2600	1589.0	571.5	0.22	1142.9	0.44

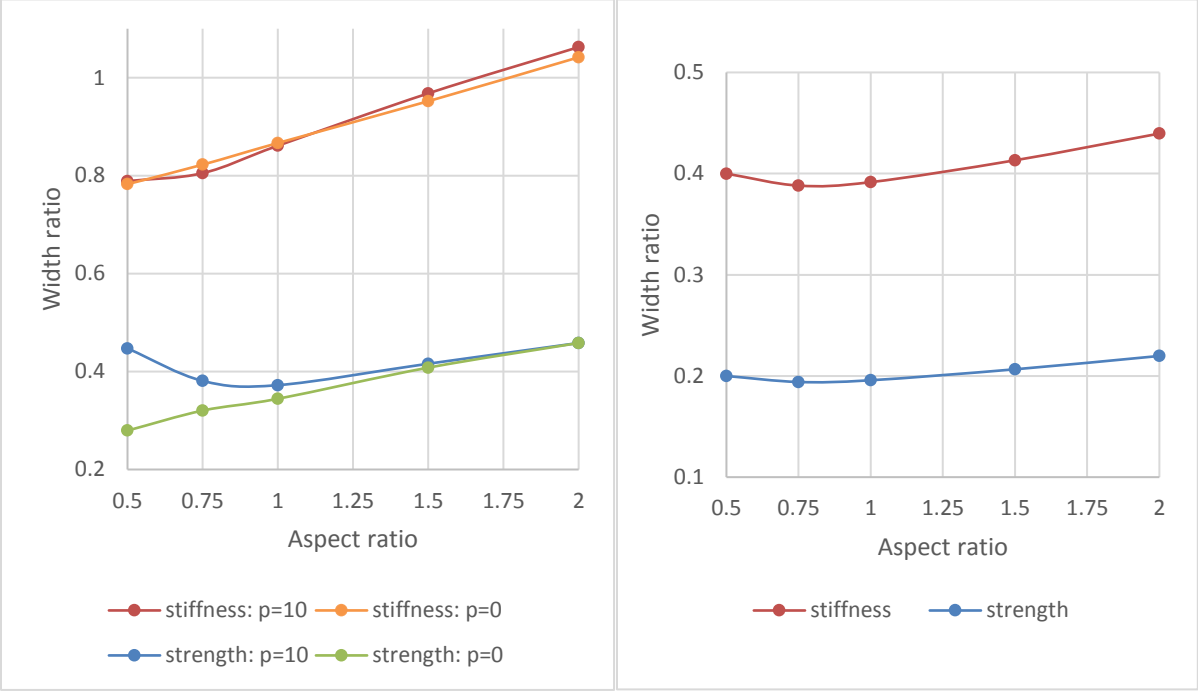

(a) Finite element model (b) CSA S304-14

Figure 6-8 Strut width ratios for strength and stiffness

In Figure 6-8, the x- axis denotes the increasing aspect ratio of the wall, and the y- axis refers to the calculated width ratios for strength and stiffness. In the legend area of plot (a), "p=0" means there is no axial stress applied to the wall, and "p=10" means the applied axial stress equals10 MPa.

Since the 40%-90% stress limits were picked before checking the standard, the resulting values of the finite element model don't match well with that of the standard. However, this is not important as the widths have to be multiplied by some factor to get the actual estimate of strength or stiffness, so different factors would be applied for the widths from the model and the standard. With respect to the aspect ratio of the wall, the changing tendency of the width ratios for the picked strength and stiffness in plot (a) is similar to the tendency indicated by the code as shown in plot (b). Also, the stiffness width in the left finite element model plot is shown to be

nearly twice the strength width, which coincides with the relationship of the diagonal strut width (considered to represent stiffness) and the effective diagonal strut width (considered to represent strength) according to the standard.

Neglecting the points of aspect ratio = 0.5, both plots (a) and (b) show that increasing the aspect ratio of the wall would result in wider strut widths for strength and stiffness. In plot (b), the width ratio curve has a “hook” at the left end for squat walls - this phenomenon also appears in the finite element model when high axial stress of 10 MPa is applied, although axial stress is not in the design equations defined by the standard. It can be observed that axial stress widens the widths for both strength and stiffness, though its influence seems limited.

Chapter 7 Failure Patterns of Partially Grouted Masonry

7.1 Problem of interest

In the last section of Chapter 6, a finite element model was created to have a panel confined by a frame using the partition tool in Abaqus. The question was then raised as to whether the stiffness of the frame (assuming the stiffness of the masonry remains the same) would affect the stress distribution over a multi-panel wall, and eventually affect the failure pattern of the wall.

As mentioned in Chapter 2 Section 2.6, two distinct failure patterns of partially grouted multi-panel walls have been reported in the literature. Figure 7-1 illustrated the two failure patterns (i.e. wall action and panel action) for typical partially grouted masonry walls subject to monotonic loading. In this chapter, finite element models will be built to investigate whether the relative stiffness ratio of the panel to the frame (represented by effective panel-to-frame modulus ratio in the study) affects the failure mode of a multi-panel wall; and if it does, can the relative stiffness ratio shift the failure pattern of the wall from a wall action (diagonal/sliding shear crack spread across the entire wall) to a panel action (panels fail individually with diagonal cracks)?

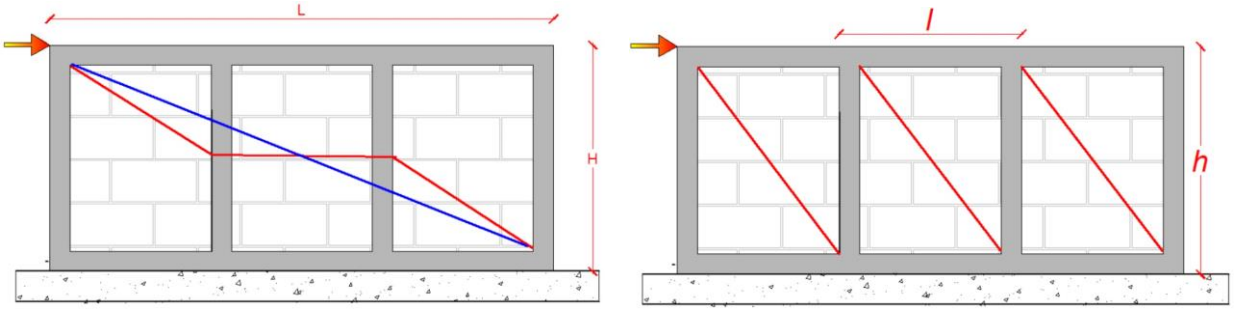

(a) wall action (b) panel action

Figure 7-1 Failure patterns of a multi-panel wall (Janaraj (2014))

7.2 Macroscopic Model

7.2.1 Model description.

Three basic models were built respectively for walls containing two panels, three panels, and four panels. Figure 7-2 illustrates the case of a three-panel wall with bond beams attached to the top and bottom of the wall. Model 3A is an intact masonry wall without a frame or separated panels. Model 3B features a frame and three panels by partitioning the wall so that the frame and the panels can be assigned with different material properties. The frame and the three panels in Model 3C are created as individual parts connected by cohesive contacts.

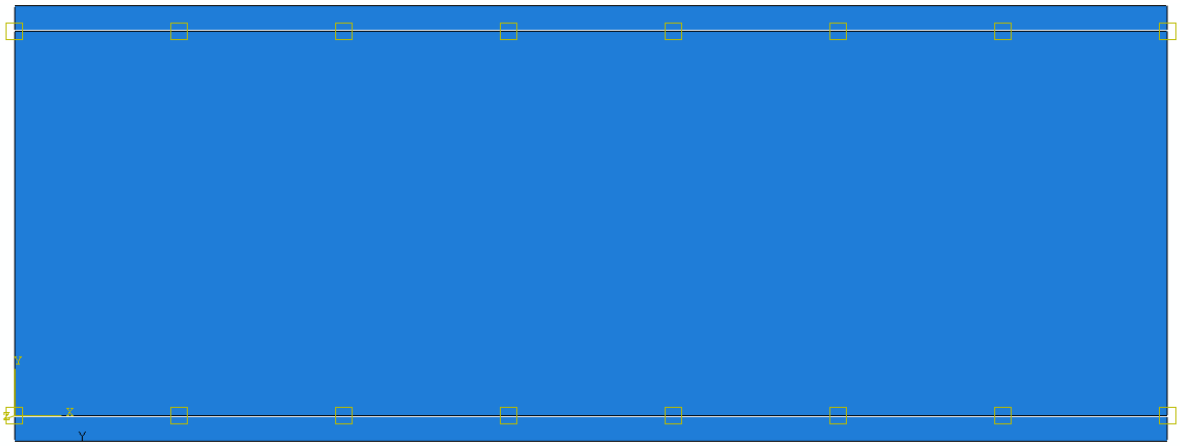

(a) Model 3A: Intact wall with no frame or panel

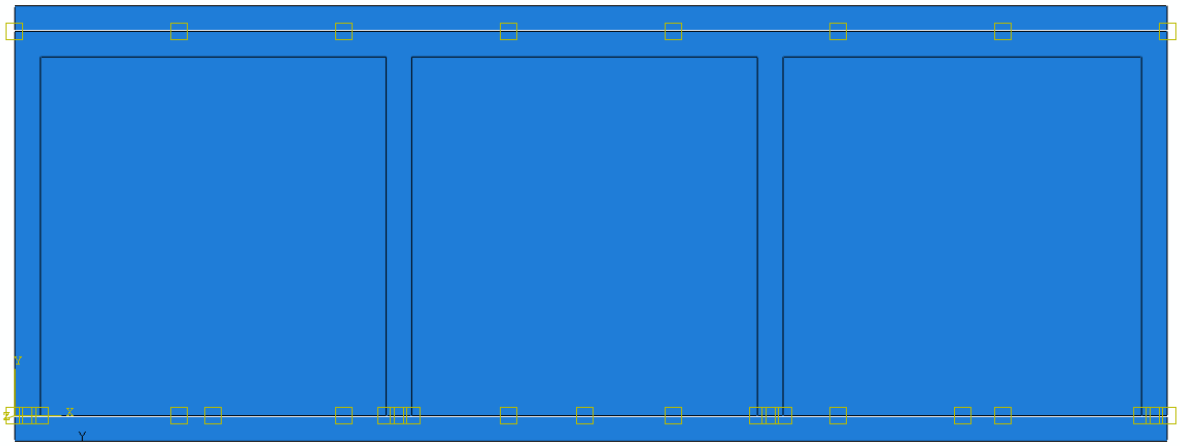

(b) Model 3B: Partitioned wall with frame and panels

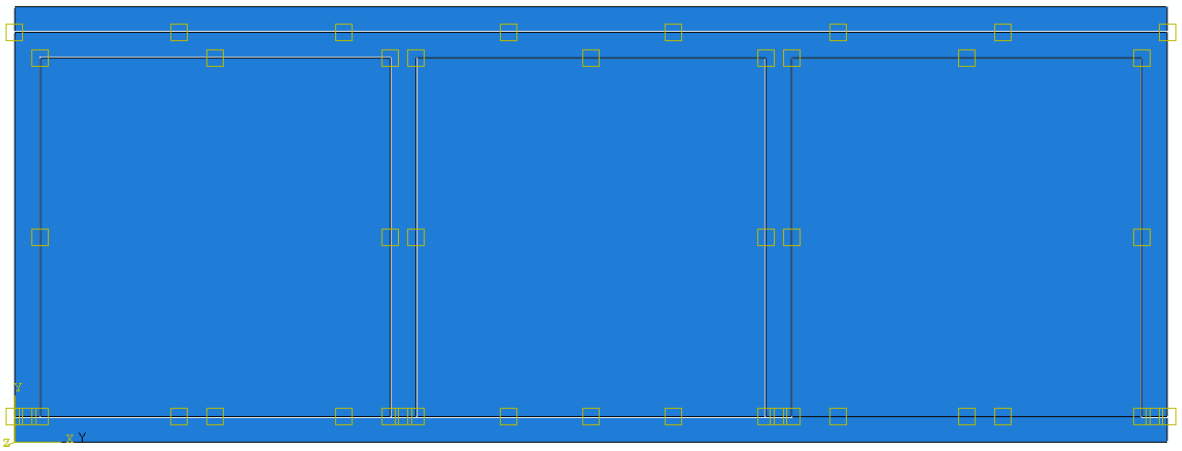

(c) Model 3C: Frame and panels bonded by cohesive contacts

Figure 7-2 Macroscopic models for a three-panel wall

The height of the wall is kept the same at 3000 mm, and the length of the wall is simply the height times the number of the panels the wall contains. Given that the width of the frame is 200 mm, the panels are 2800 mm in height, and are almost square. The length of the panels in each model varies between 2700 mm, 2733mm, and 2750 mm.

Surface traction is applied to the top surface of the top beam to act as lateral load, so that the magnitude of the load is proportional to the length of the wall, and therefore proportional to the number of the panels composing the wall. The bottom beam is fixed while the top beam is confined vertically to keep to the horizontal level.

7.2.2 Relative stiffness ratio of the panel to the frame.

The relative ratio of the masonry panel to the frame is considered using a factor λ_h proposed by Stafford Smith and Carter (1969).

$$\lambda_h = \sqrt[4]{\frac{E_m t \sin 2\theta}{4E_f I_c h}} \qquad \text{Equation 7-1}$$

where E_m, E_f = elastic moduli of the masonry panel and the frame, respectively

I_c = moment of inertia of the frame column

h = height of the masonry panel

t = thickness of the wall

θ = $\tan^{-1}\frac{h}{l}$, l is the length of the masonry panel

In partially grouted concrete masonry, the "frame" is a composition of grouted/reinforced concrete cores acting as columns and bond beams acting as horizontal beams, rather than a reinforced concrete frame infilled by masonry panels. Therefore, the elastic modulus of the frame is contributed by the concrete masonry, the grout and the reinforcing bars.

An experimentally validated anisotropic material model presented by Haider (2007) was first considered to simulate the behaviour of the masonry. However, this material model contains 21 properties and a considerable amount of stress-strain test data under compression and tension damage, which makes it too complex for the purpose of this study. Hence, isotropic elastic material properties were assigned to both the masonry panel (E_m=10,000 MPa, Poisson's ratio=0.25) and the effective composite frame (E_f=10,000 MPa in the beginning, Poisson's ratio=0.25), so that the relative stiffness ratio factor λ_h can be implemented.

Furthermore, since the dimensions of the panel and the frame are certain in the model, the relative stiffness ratio factor λ_h is basically equal to $\sqrt[4]{\frac{E_m}{E_f}}$ times a certain coefficient $\sqrt[4]{\frac{t\sin 2\theta}{4I_c h}}$. In other words, the relative stiffness ratio can be simply represented by the effective panel-to-frame modulus ratio $\sqrt[4]{\frac{E_m}{E_f}}$ of the masonry panel to the frame.

7.2.3 Effect of frame-panel bond strength.

Figure 7-3 shows how the bond strength between the frame and the panels (contributed by the strengths of masonry unit and masonry-mortar bond) can affect the principal compressive stress distribution across the wall, when the frame is as stiff as the masonry. To highlight the area of high principal compression in the walls, a lower bound stress limit was set to eliminate the area with low principal compressive stress (the gray colour area). Also, the bond beams and the frame are hidden from the view to better present the stress distribution in the panels.

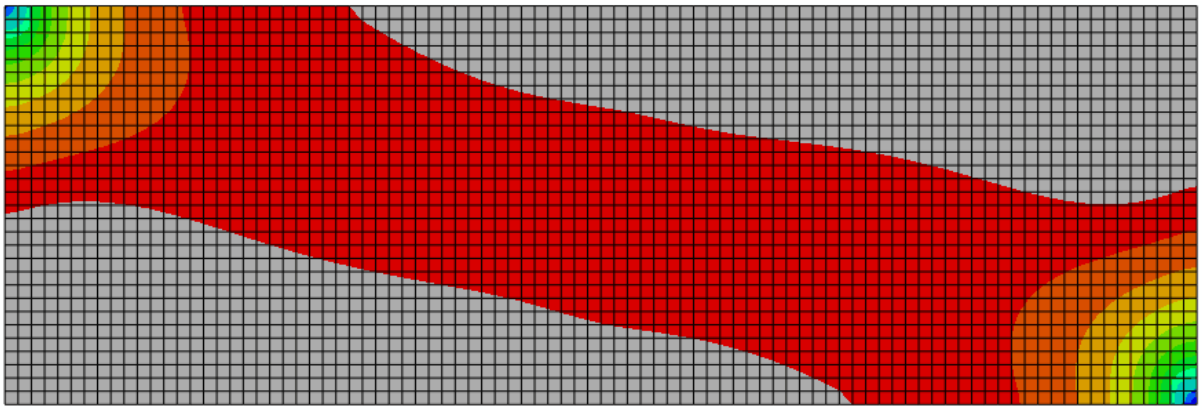

(a) Model 3A

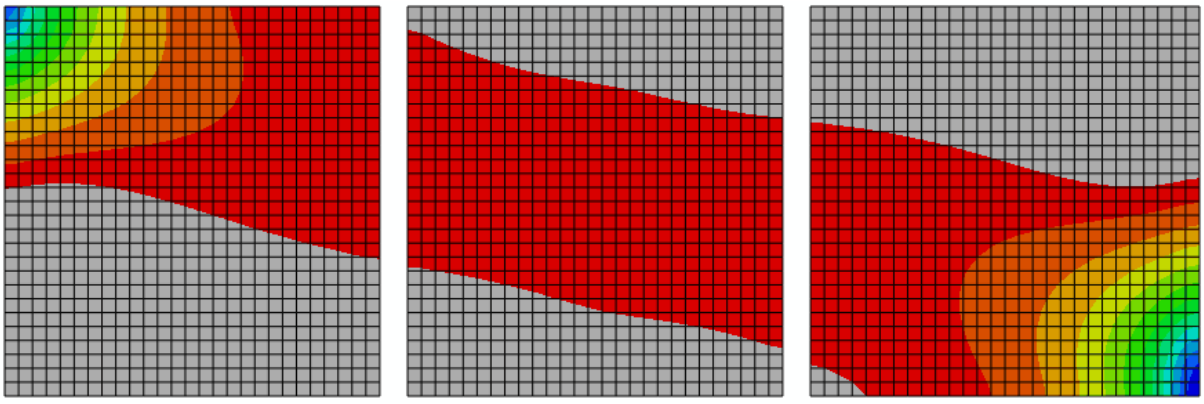

(b) Model 3B

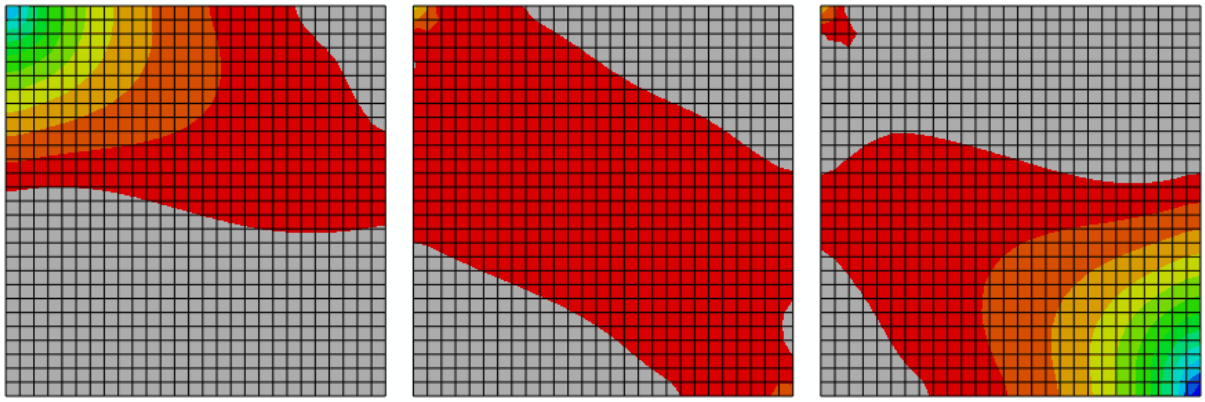

(c) Model 3C with moderate cohesion

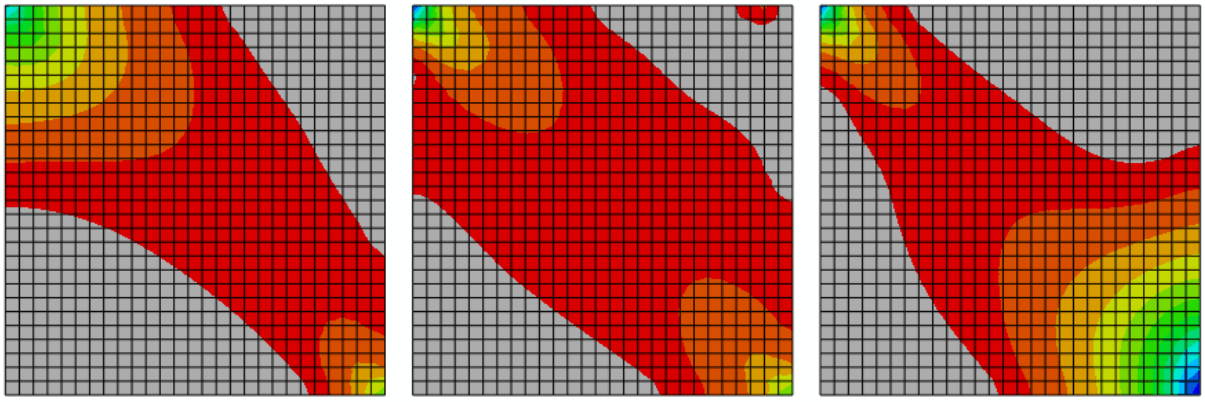

(d) Model 3C with weak cohesion

Figure 7-3 Compressive principal stress in a three-panel wall (varied bonding)

In Figure 7-3, Model 3A, which features no frame or panels, demonstrates a continuous diagonal compression strut throughout the wall (wall action). In Model 3B, although the frame and the panels can be assigned with different materials due to the partition, they still serve as a continuum part together. Hence, it can be inferred that the bond strength between the frame and panels is pretty strong. This strong bond strength causes Model 3B to produce a similar wall pattern to Model 3A. Plot (c) shows the principal compressive stress distribution in Model 3C when a set of moderate cohesion properties is assigned to the contacts between the frame and the panels. It appears that this wall is in an intermediate situation where it could fail in either a wall

action or a panel action. Plot (d) illustrates the stress distribution in Model 3C when weak cohesion properties are assigned to the contacts bonding the frame and the panels. This situation causes individual compression struts to occur in each panel, which is a clear panel behaviour.

In summary, it can be inferred that a strong frame-masonry bond strength is likely to cause the wall to fail in a wall action, while a weak frame-masonry bond strength would result in a panel fashion. To be able to discuss the effect of relative stiffness ratio of the panel to the frame (will be represented by the effective modulus ratio $\sqrt[4]{\frac{E_m}{E_f}}$) in the next section, the configuration of Model 3C with moderate cohesion was selected so as to minimize the influence from the frame-masonry bond strength.

7.2.4 Effect of relative stiffness ratio.

As mentioned above, the contact model (Model 3C) with moderate cohesive properties assigned to the contacts between the frame and the panels was adopted to investigate the effect of relative stiffness ratio of the panel to the frame. In this study, the relative stiffness ratio is represented by the effective modulus ratio $\sqrt[4]{\frac{E_m}{E_f}}$, whilst E_m does not change and E_f will be raised to a multiple of E_m.

The compressive principal stress distributions across the wall with increasing E_f are illustrated in Figure 7-4 (two-panel wall), Figure 7-5 (three-panel wall) and Figure 7-6 (four-panel wall). The result of the partitioned model (Model 3B) which exhibits a clear wall action is given at the beginning of each figure for comparison when $E_f = E_m$. Since increasing E_f causes the stress value and distribution to differ, varied lower bound stress limits are assigned to the stress contour plots to capture the shape of the compression struts in the wall.

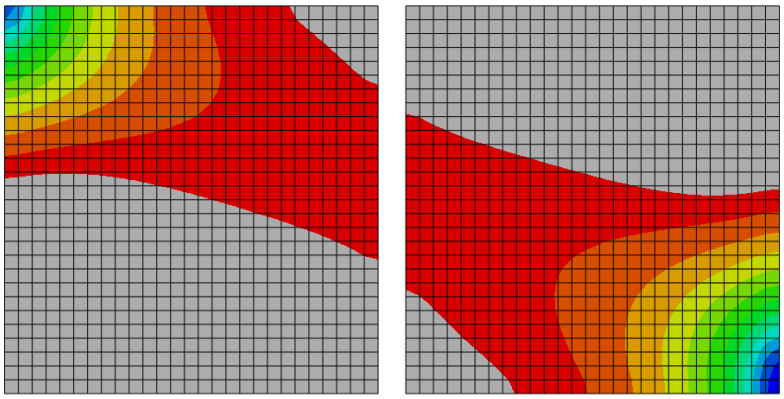

(a) $E_f = E_m$, $\sqrt[4]{\frac{E_m}{E_f}} = 1$ (partitioned model)

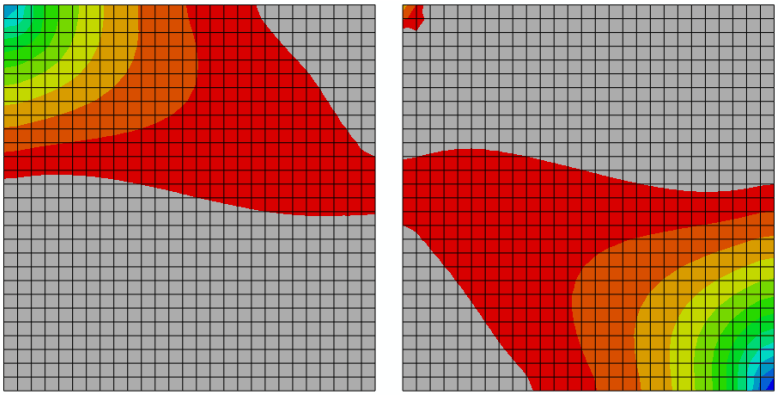

(b) $E_f = E_m$, $\sqrt[4]{\frac{E_m}{E_f}} = 1$

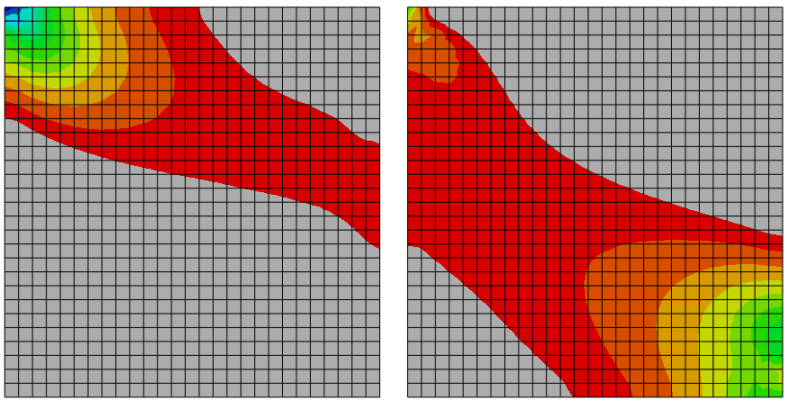

(c) $E_f = 10E_m$, $\sqrt[4]{\frac{E_m}{E_f}} = 0.56$

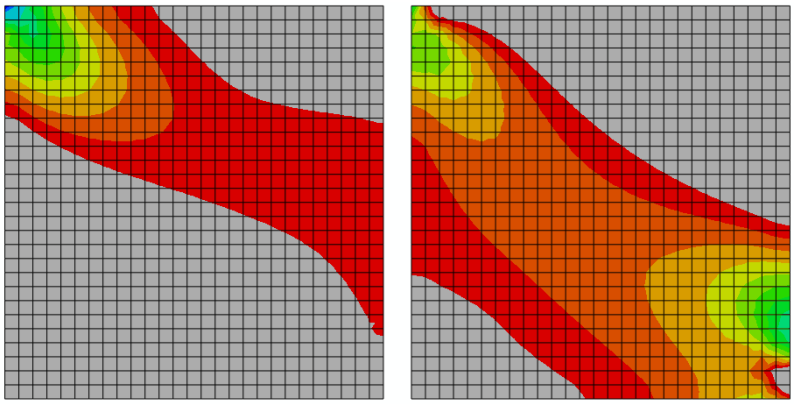

(d) $E_f = 20E_m$, $\sqrt[4]{\frac{E_m}{E_f}} = 0.47$

Figure 7-4 Compressive principal stresses in a two-panel wall

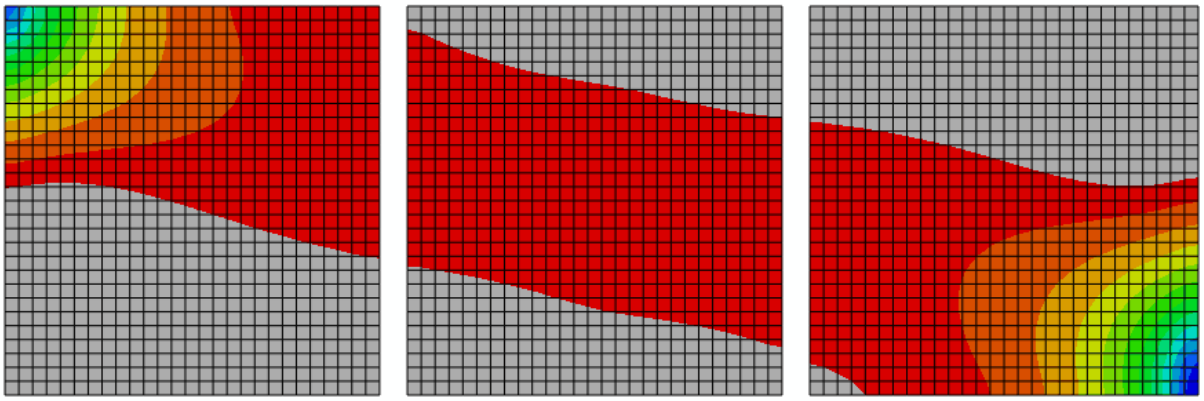

(a) $E_f = E_m$, $\sqrt[4]{\frac{E_m}{E_f}} = 1$ (partitioned model)

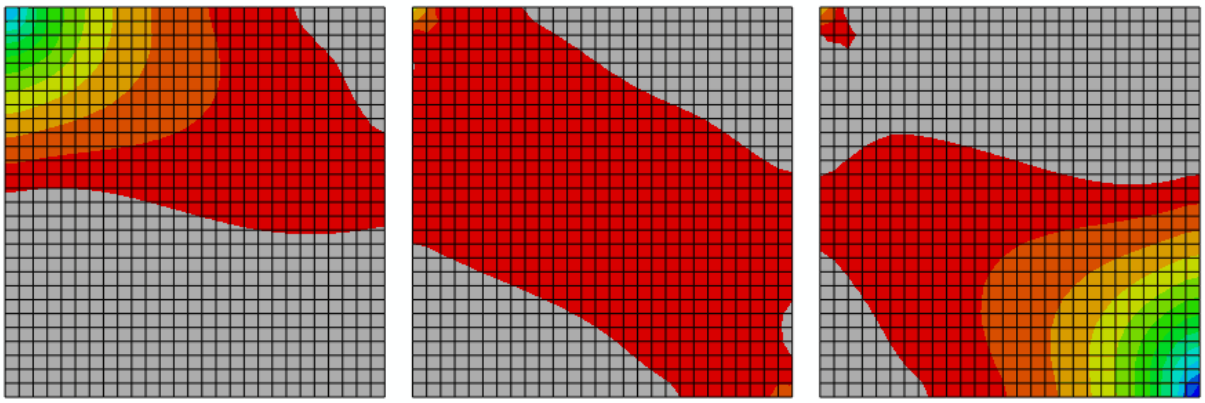

(b) $E_f = E_m$, $\sqrt[4]{\frac{E_m}{E_f}} = 1$

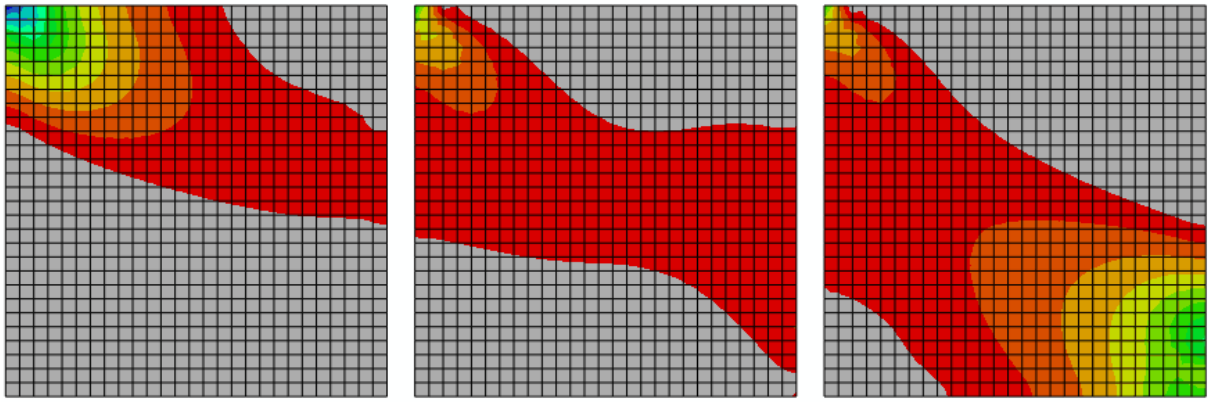

(c) $E_f = 10E_m$, $\sqrt[4]{\frac{E_m}{E_f}} = 0.56$

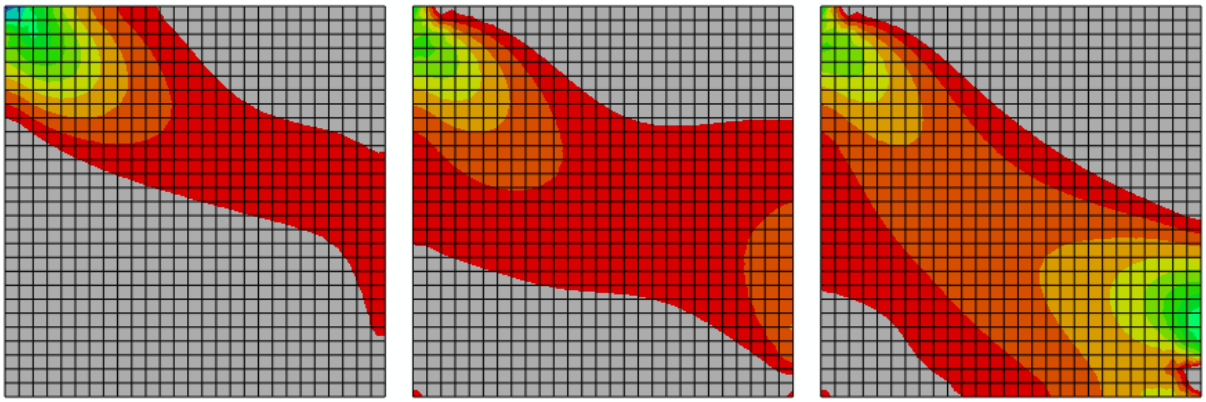

(d) $E_f = 20E_m$, $\sqrt[4]{\frac{E_m}{E_f}} = 0.47$

Figure 7-5 Compressive principal stresses in a three-panel wall

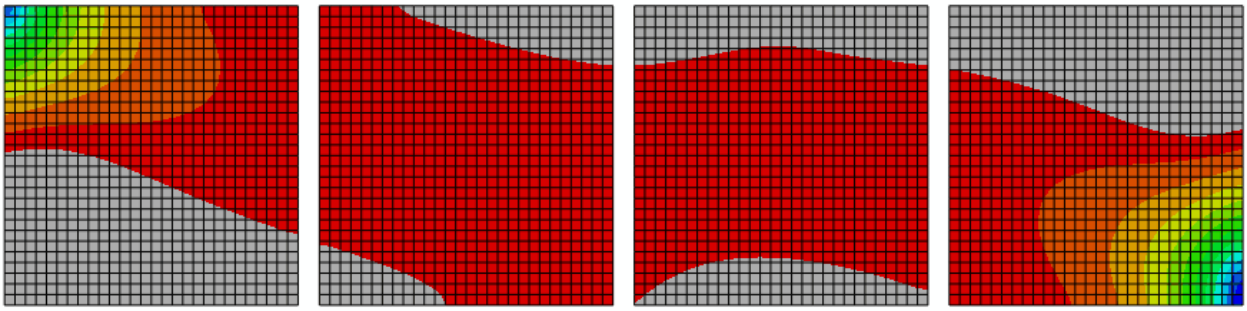

(a) $E_f = E_m$, $\sqrt[4]{\frac{E_m}{E_f}} = 1$ (partitioned model)

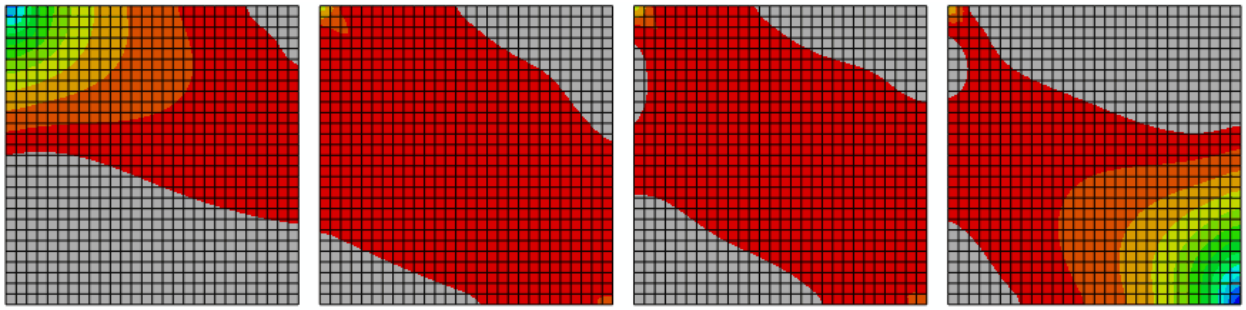

(b) $E_f = E_m$, $\sqrt[4]{\frac{E_m}{E_f}} = 1$

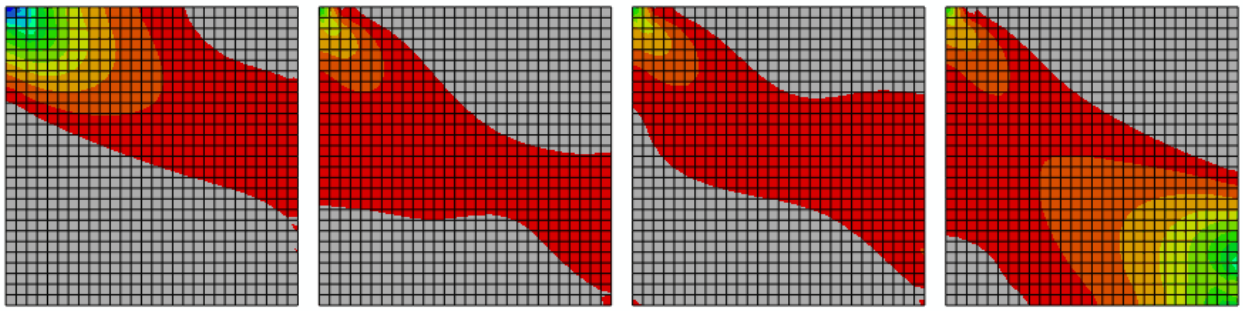

(c) $E_f = 10E_m$, $\sqrt[4]{\frac{E_m}{E_f}} = 0.56$

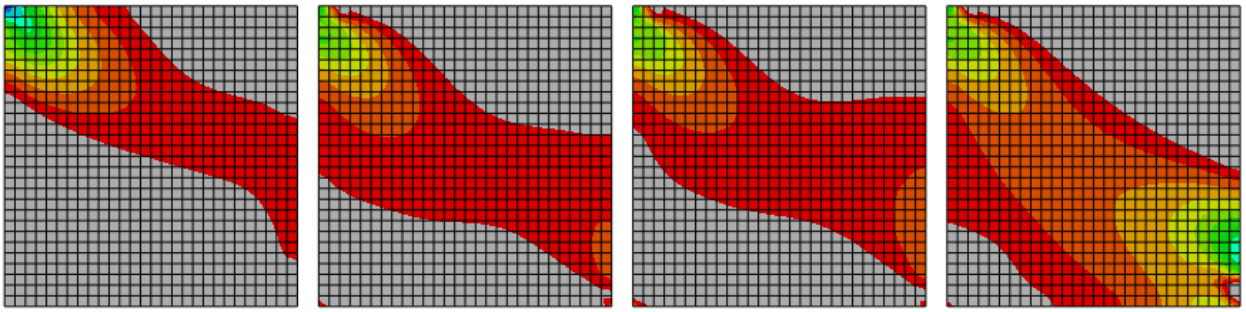

(d) $E_f = 20E_m$, $\sqrt[4]{\frac{E_m}{E_f}} = 0.47$

Figure 7-6 Compressive principal stresses in a four-panel wall

In Figure 7-4, Figure 7-5, and Figure 7-6, plots (a) show what the stress pattern looks like in the partitioned model, which simulates a wall with strong frame-masonry bond when E_f equals E_m. It can be observed from plots (b) to plots (d) that the compressive principal stress

distribution shifts from a wall pattern at the beginning (when $E_f = E_m$, $\sqrt[4]{\frac{E_m}{E_f}} = 1$) to a distinct panel pattern in the end (when $E_f = 20E_m$, $\sqrt[4]{\frac{E_m}{E_f}} = 0.47$). This means a multi-panel wall can demonstrate a wall pattern when the effective panel-to-frame modulus ratio $\sqrt[4]{\frac{E_m}{E_f}}$ is close to 1, whereas a low effective modulus ratio would likely cause the wall to fail in a panel action.

Also, when load is applied from left to right, the two left-end panels seem to prefer demonstrating a wall pattern, while the right-end panel seems to be more prone to develop a compression strut independently in a panel action. The right-end panel shows a clear diagonal strut as early as when $E_f = 10E_m$, $\sqrt[4]{\frac{E_m}{E_f}} = 0.56$, while the two left-end panels waited to shift to the panel pattern till $E_f = 20E_m$, $\sqrt[4]{\frac{E_m}{E_f}} = 0.47$.

In addition, it can be noted from the plots that the more panels a wall contains, the more likely the wall will fail in a panel pattern.

7.3 Microscopic Model

7.3.1 Basic model of a single-panel wall.

To verify the impact of relative panel-to-frame stiffness ratio (represented by effective panel-to-frame modulus ratio), a microscopic model was created to visualize the shear cracking in a masonry wall. A basic single-panel wall model was built to first explore the contact configuration as shown in Figure 7-7.

The wall is 6.5 units wide and 13 units high. Each masonry unit is created as an individual part. The full-size unit is 190 mm wide and 95 mm high (with thickness=90.5 mm). The half-size unit is a square part with side length of 95 mm. In the right plot of Figure 7-7, the

area highlighted by the red grid is grouted/reinforced and can be treated as the "frame" of the wall. The green area confined by the frame is plain unreinforced masonry. The full-size units contributed to forming the frame were partitioned into two halves, so that these units can be assigned with two different material properties - half grouted and half ungrouted.

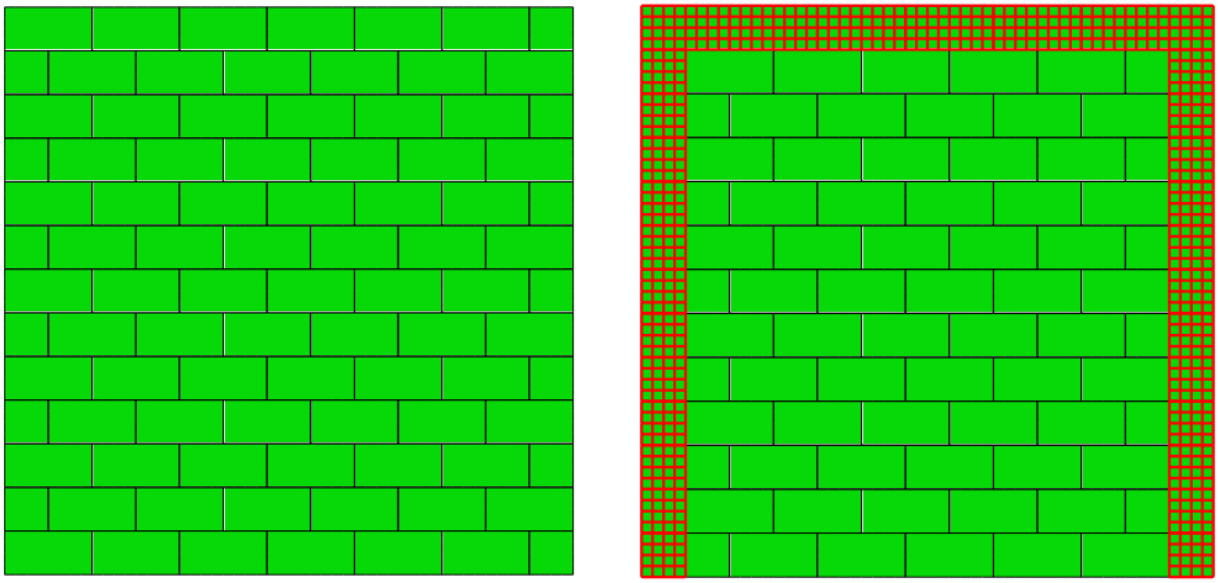

Figure 7-7 Basic model of a single-panel wall

The elastic modulus of the masonry panel (composed by ungrouted units), E_m, equals 10,000 MPa, with Poisson's ratio=0.25. The elastic modulus of the frame (composed by grouted units), E_f, was first kept the same with E_m, and was later increased as a multiple of E_m.

The bottom surface of the wall was fixed in both horizonal and vertical directions since the initial step. An axial stress of 0.5 MPa was distributed along to the top surface of the wall in the pre-compression load step. Lateral load was applied to the top surface in the form of a horizontal displacement in the lateral load step. The nonlinear geometry option was turned on when configuring the load steps. The number of attempts in each time incrementation was increased to 20 so as to ease the convergence difficulty.

7.3.2 Contact model.

Regarding the contacts between the masonry units, a spring contact model proposed by Chen and Liu (2015) was first considered and implemented with a smaller size single-panel wall (4.5-unit wide and 9-unit high) as shown in Figure 7-8.

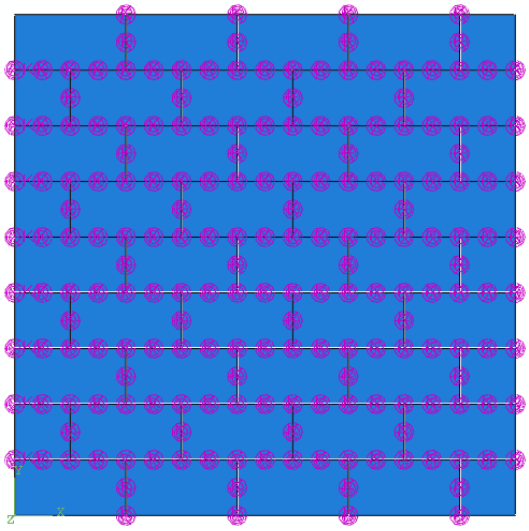

Figure 7-8 Spring contact

The idea is to connect each two coincident nodes from different units with two springs in the normal and shear directions. Therefore, a two-node joint needs two springs, and a three-node joint needs six springs. This requires 648 springs for the small size single-panel wall, and the springs were created by a script coded in Python. Since a two-panel wall was intended to be built next, the spring contact model was considered too complex to implement and thus was not adopted in this study.

Instead, the surface-based cohesive behaviour approach offered by Abaqus was adopted to simulate the interactions between the units. Surface-to-surface contact pairs were created to bond adjacent grouted units in the frame, which were denoted by the yellow squares in Figure 7-9. A surface-based general contact was established for all the other contacting interfaces within

the wall – either between adjacent ungrouted units in the panel, or between the grouted frame and the panel. This method resulted in 30 contact pairs and one general contact for a normal size single-panel wall (6.5-unit wide, 13-unit high), and this can be implemented in the GUI (graphical user interface) instead of writing a script.

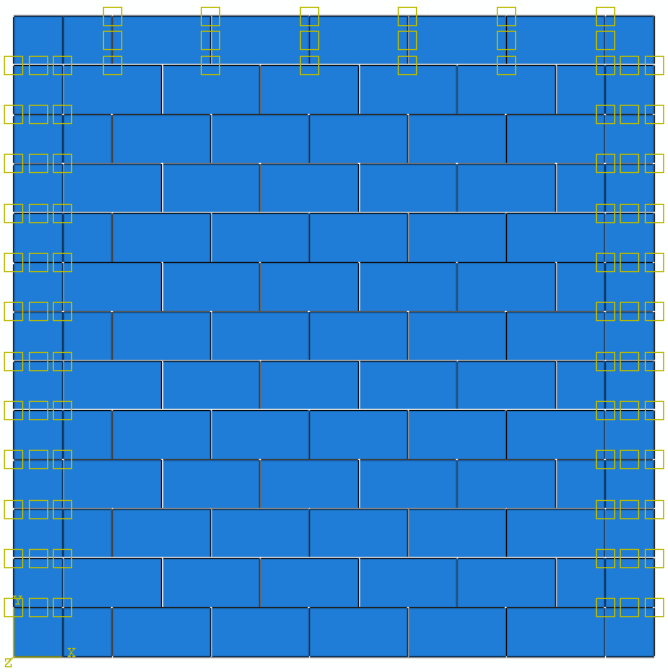

Figure 7-9 Surface-based contact

7.3.3 Contact properties.

The contact pairs (in the frame) and the general contact (in the panel, as well as between the frame and the panel) were assigned with respective contact properties, both including hard compression behaviour (which minimizes the penetration of the contacting surfaces), penalty friction (which prevents slipping regardless of contact pressure, friction coefficient=0.7), cohesive behaviour in the normal and shear directions, and damage initiation and evolution criteria based on a traction-separation law. Damage stabilization (viscous coefficient=1E-5) was also added in order to ease the convergence difficulty.

With respect to the cohesive behaviour, the normal and shear cohesive stiffnesses (k_n and k_s) were determined using the expressions in Equation 7-1, proposed by Lourenço (1994).

$$k_n = \frac{E_m E_{mortar}}{h_{mortar}(E_m - E_{mortar})},\ k_s = \frac{G_m G_{mortar}}{h_{mortar}(G_m - G_{mortar})} \qquad \text{Equation 7-2}$$

where E_m and E_{mortar} are the Young's moduli of the masonry and the mortar, G_m and G_{mortar} are the shear moduli of the masonry and the mortar, and h_{mortar} is the thickness of the mortar joints. Assumptions have been made for these parameters in order to determine the cohesive stiffnesses: $E_{mortar} = E_m/10$, $G_m = 0.4E_m$, $G_{mortar} = 0.4E_{mortar}$, and $h_{mortar} = 5$ mm.

Concerning the damage mechanism, a bilinear traction-separation response was considered as shown in Figure 7-10. Point A indicates the initiation of damage, and point B marks the completion of damage evolution. This constitutive response is similar to the one used for the XFEM crack described in Chapter 5 Section 5.2 (Figure 5-3), except that the undamaged traction-separation behaviour needs to be specified in this case. The slope of the line between point O and point A is actually one of the cohesive stiffnesses calculated from Equation 7-2, depending on which direction (normal or shear) is under consideration.

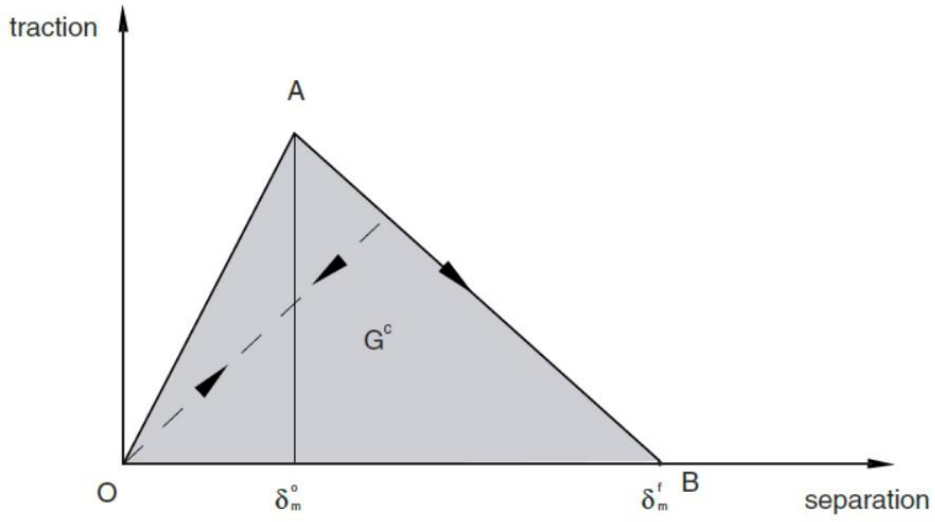

Figure 7-10 Bilinear traction-separation response (Abaqus (2014))

Energy-based damage evolution was chosen. The fracture energy required for input is equal to the area under the traction-separation curve. The dependence of the fracture energy on the mode mix was defined based on a power law fracture criterion in a linear fashion (power=1).

7.3.4 Simplified model of a single-panel wall.

The basic model shown in Figure 7-7 contains five different types of unit: one grouted full-size unit, one ungrouted full-size unit, one partitioned full-size unit with grouted material on the left and ungrouted material on the right, another partitioned full-size unit with the order of the materials reversed, and lastly, one grouted half-size unit. This variety of units increases the difficulty when establishing the wall geometry and assigning the contact pairs.

As shown in Figure 7-11, a simplified model consists of merely one grouted half-size unit (which forms the frame) and one ungrouted half-size unit (which composes the masonry panel). This simplifies the procedure of assembling the wall geometry, whilst also easing the procedure of defining the 30 contact pairs. Everything else was configured the same as the basic model, except one procedure was added in the end: two half-size units were bonded together by a “tie” constraint to form a full-size unit, signified by the sets of three yellow circles in Figure 7-11.

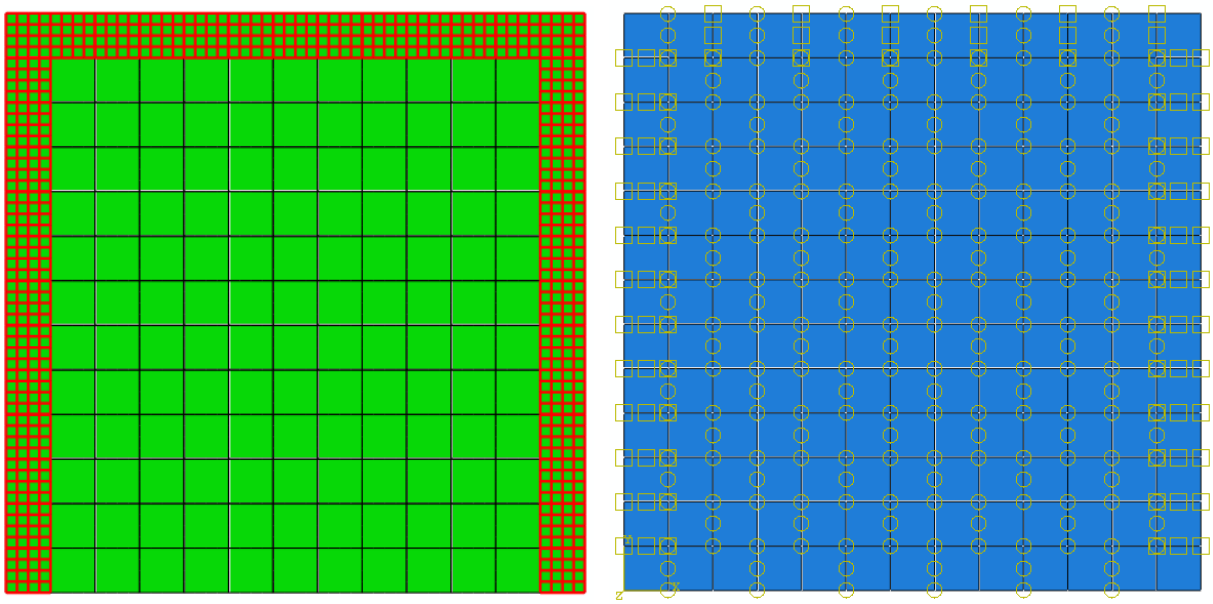

Figure 7-11 Simplified model of a single-panel wall

Figure 7-12 demonstrates the cracks developed by both the basic model and the simplified model in the case of a single-panel wall, with a deformation scale factor of 30. In plots (a) and (b), the two models demonstrate almost identical crack patterns aligned with the diagonal when E_f equals E_m. The cracking patterns in plots (c) and (d) also highly agree with each other when E_f is increased to 10 times of E_m. Hence, the simplified model was considered effective for predicting the cracking pattern. A two-panel wall was built based on this model.

It is worth mentioning that increasing E_f means the frame is started to be grouted and reinforced. It can be imagined that the presence of the grout and the reinforcing bars contributes to the increase in E_f, as well as the increase in bond strengths at interfaces between the grouted units (in the frame). Hence, the bond strengths in the contact pairs for grouted units were assumed to increase in the same proportion as E_f/E_m with respect to the bond strengths in the masonry panel.

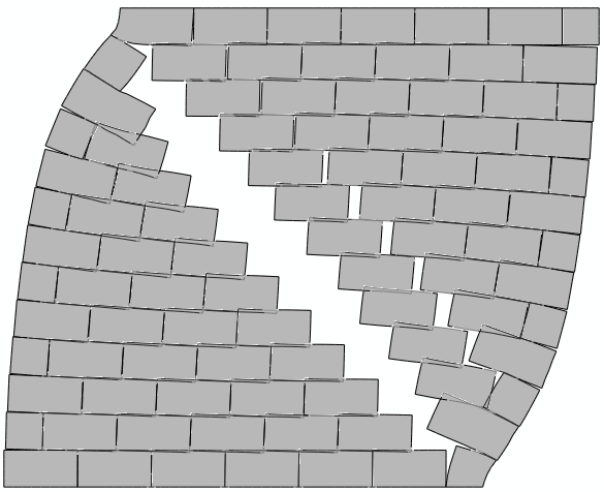

(a) Basic model, $E_f = E_m$, $\sqrt[4]{\frac{E_m}{E_f}} = 1$

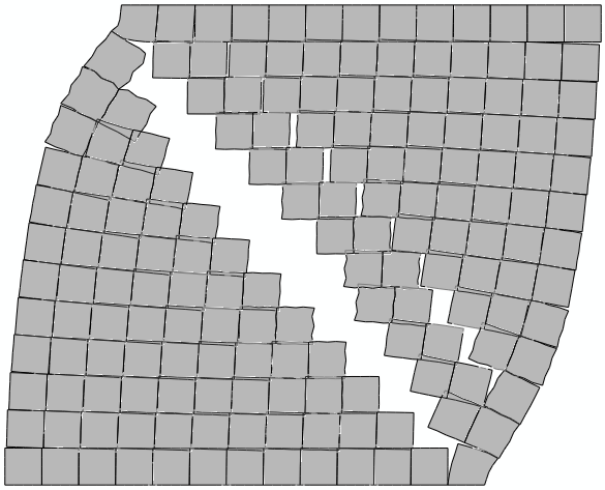

(b) Simplified model, $E_f = E_m$, $\sqrt[4]{\frac{E_m}{E_f}} = 1$

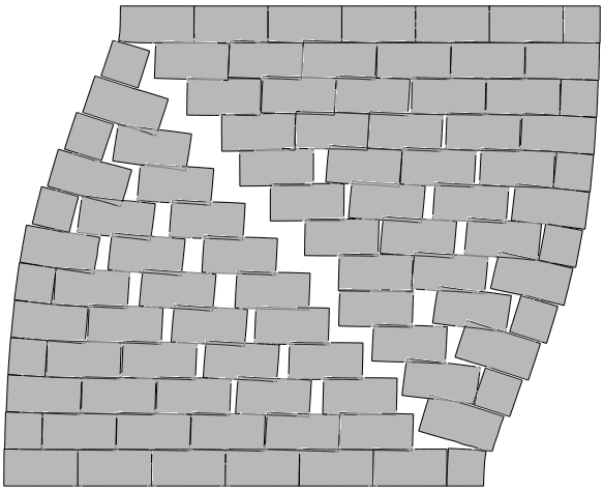

(c) Basic model, $E_f = 10E_m$, $\sqrt[4]{\frac{E_m}{E_f}} = 0.56$

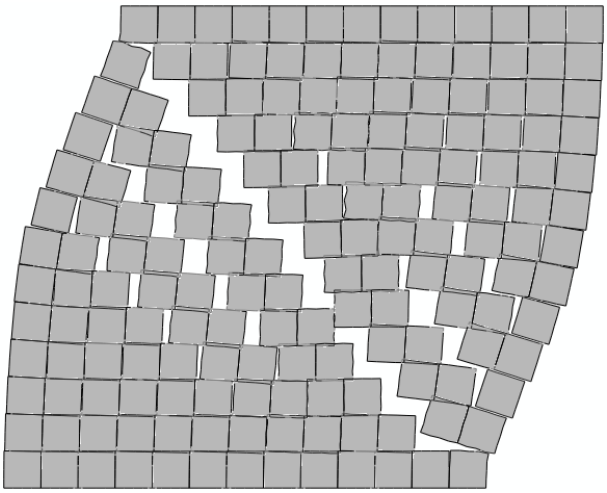

(d) Simplified model, $E_f = 10E_m$, $\sqrt[4]{\frac{E_m}{E_f}} = 0.56$

Figure 7-12 Cracks developed in a single-panel wall

7.3.5 Simplified model of a two-panel wall.

As given in Figure 7-13, the two-panel wall is of the same height as the single-panel wall, but 6 full-size blocks wider. All the other configurations are kept the same with the single-panel wall, including axial stress and displacement-controlled shear load.

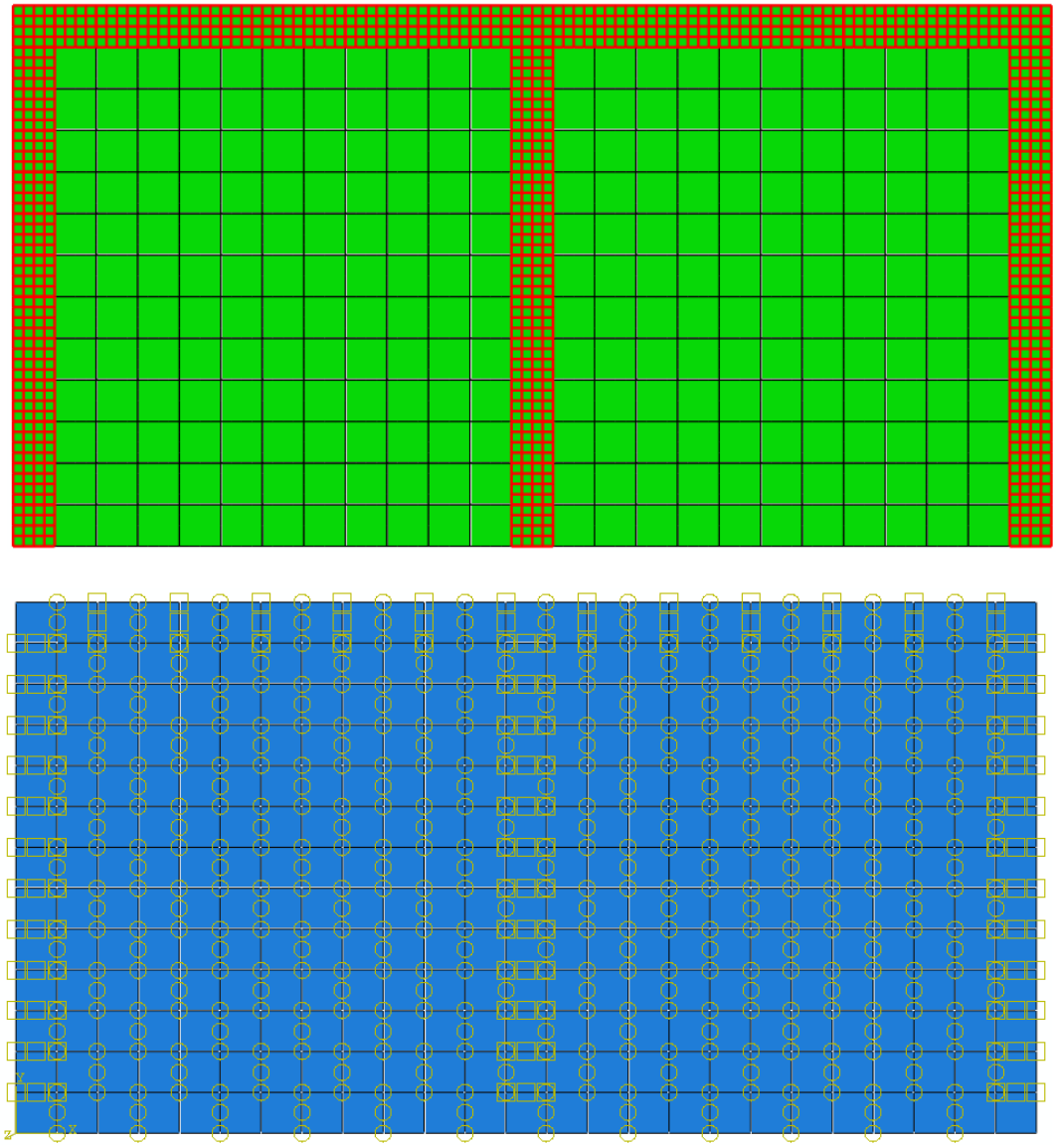

Figure 7-13 Simplified model of a two-panel wall

Figure 7-14 depicts the cracking pattern of a two-panel wall with increasing panel-to-frame stiffness ratio (denoted by E_{frame}/E_{panel}). All the cracking patterns are plotted at a certain step time (time difference within 1%) to ensure that the top surfaces of the walls were subject to the same horizontal displacement. The deformation scale factor is set to be 80 to display the cracks clearly.

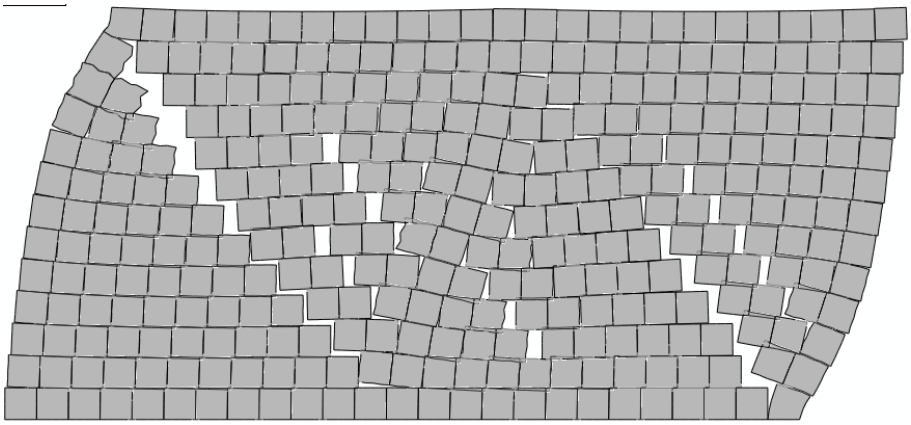

(a) $E_f = E_m$, $\sqrt[4]{\frac{E_m}{E_f}} = 1$

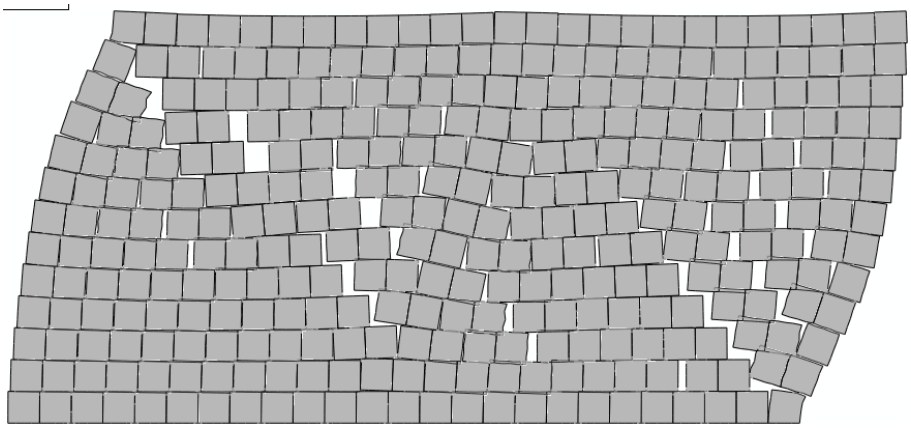

(b) $E_f = 3E_m$, $\sqrt[4]{\frac{E_m}{E_f}} = 0.76$

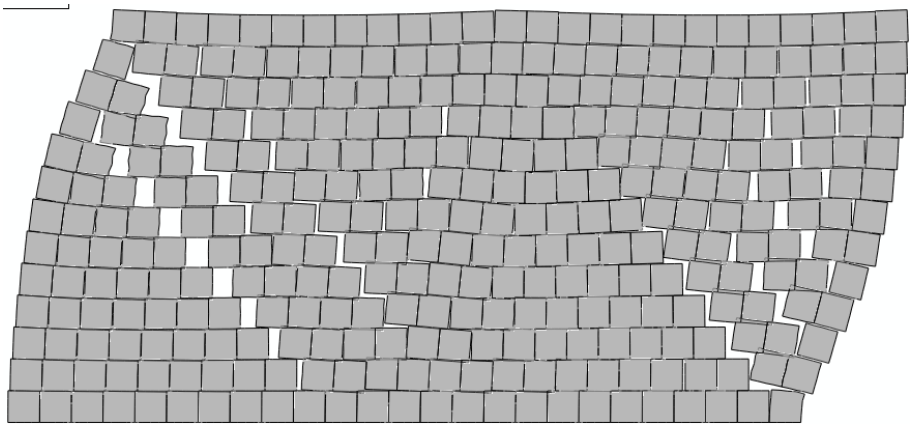

(c) $E_f = 5E_m$, $\sqrt[4]{\frac{E_m}{E_f}} = 0.67$

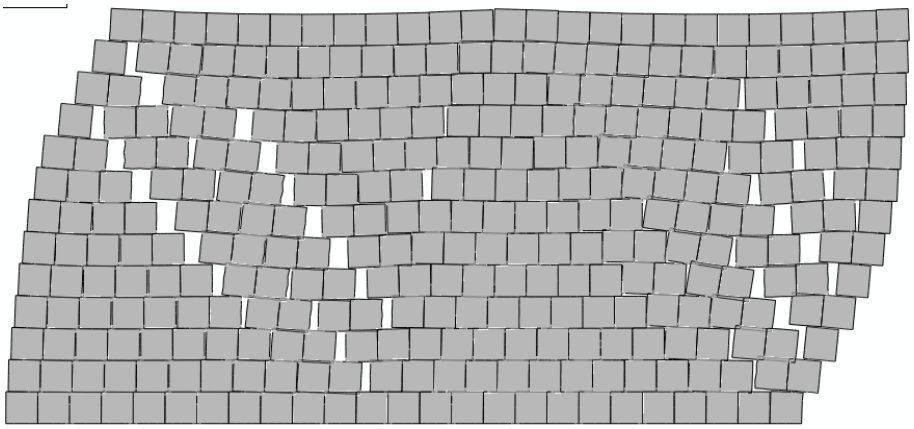

(d) $E_f = 10E_m$, $\sqrt[4]{\frac{E_m}{E_f}} = 0.56$

Figure 7-14 Cracks developed in a two-panel wall

In Figure 7-14, the wall almost demonstrates a wall pattern when $E_f = E_m$, $\sqrt[4]{\frac{E_m}{E_f}} = 1$. The top left half of the left panel cracks diagonally, as does the bottom right half of the right panel. In the middle of the wall, the blocks in courses 4 to 6 appear to slide past each other. In reality, a single horizontal sliding crack is most likely to develop in this region as the joints would have different strengths and the weakest joint would crack. The left panel does show the diagonal crack continuing down to the bottom right corner, in what would be a panel failure, but the width of this crack is substantially less than for the top half. When $E_f = 10E_m$, $\sqrt[4]{\frac{E_m}{E_f}} = 0.56$, the cracks seem to develop more clearly into a panel pattern, as shown in plot (d). Plots (b) and (c) illustrate the transition from a wall pattern to a panel pattern, with the (c) $E_f = 5E_m$, $\sqrt[4]{\frac{E_m}{E_f}} = 0.67$ case showing a distinct propensity for panel failure. The effect of the relative panel-to-frame stiffness ratio is thus undeniable. When the effective modulus ratio $\sqrt[4]{\frac{E_m}{E_f}}$ is close to 1, the wall is likely to fail in a wall pattern. The lower the effective modulus ratio becomes, the more likely the wall develops cracks in a panel pattern. This conclusion also agrees with the observation from the macroscopic model in Section 7.1.3.

Chapter 8 Summary and Conclusions

The work in this thesis has exposed some of the basic parameters that need to be examined with respect to the behaviour of partially grouted (and reinforced) concrete masonry subject to in-plane shear in addition to those already established in the literature. The effects of axial stress and aspect ratio were known in part, and these have been expanded upon. The effect of relative panel-to-frame stiffness ratio (represented by effective panel-to-frame modulus ratio in the study) is a completely new contribution to the knowledge. The particular conclusions with respect to the variables examined are listed below.

8.1 Effect of boundary condition and load application

- Walls with vertically restrained top boundary conditions and distributed lateral load applied to the top surface presented a symmetric distribution of principal compressive stress with respect to the diagonal.
- The addition of a bond beam effectively released undesirable tension in the anti-diagonal corners of the wall, as well as distributed the lateral load evenly to the top surface of the wall despite the location and area of the contact between the actuator and the bond beam.

8.2 Effect of axial stress

- Increasing the axial stress caused a decrease in the principal tensile stress, as well as a decrease in the tensile stress at the surface of imaginary voids, according to a cohesive strength model. (more noticeable in walls with low aspect ratios and in areas close to the compressive diagonal)
- An increase in axial stress widened the diagonal compression strut (zone of high principal compressive stress) and slightly altered the direction of the strut clockwise. (more noticeable in squat walls)

- The presence of axial stress (from 0 to 10 MPa) seemed to have limited influence on the magnitude of the compressive strut width ratios accounting for strength and stiffness. However, axial stress “bend” the width ratio curves (with respect to varying aspect ratios) when the aspect ratio is below one. This phenomenon was also demonstrated by the curves plotted according to the Canadian Standard, though this effect of axial stress is not indicated in the Canadian Standard.

8.3 Effect of wall aspect ratio

- Walls with lower aspect ratio were found to have a scattered pattern of principal compressive stress, while walls with higher aspect ratios presented a concentrated pattern of stress aligned with the diagonal.
- Increasing the aspect ratio altered the direction of the diagonal compression strut in an anticlockwise manner (as opposed to the axial stress), and resulted in wider strut widths for strength and stiffness according to both the finite element study and the Canadian Masonry Design Standard.
- In the study of the cohesive strength model, it had been observed that under a high level of axial stress (10MPa), an increase in the aspect ratio led to an increase in the tensile stress at the surface of the void. When there was no axial stress, the aspect ratio had a less remarkable influence on such stress.

8.4 Factors affecting multi-panel walls

- Relative panel-to-frame stiffness ratio was proved to affect the failure pattern of partially grouted multi-panel walls with finite element studies. When the effective panel-to-frame modulus ratio is close to 1, multi-panel walls presented cracking (as well as high principal compressive stress) in a wall action. Decreases in the relative modulus ratio

caused the multi-panel walls to shift the cracking pattern from a wall action to a panel action.

- When the frame-panel bond strength is significantly high, multi-panel walls presented high principal compressive stress in a wall cracking pattern. Decreasing the frame-panel bond strength caused the multi-panel walls to shift from a wall behaviour to a panel behaviour.

8.5 Suggestions for future studies

More investigations, both modelling and experimental can be done regarding,

1. The effect of axial stress on the strut widths for strength and stiffness, especially the "bending" phenomenon on the strut widths curves with respect to varying aspect ratios. The work should be aimed at providing data so that this aspect of the Canadian Design Standard can be improved.
2. The effect of panel aspect ratio on failure pattern of multi-panel walls. The work should be aimed at giving basic understanding of the mechanisms involved such that in time, provisions can be introduced into the Canadian Standard.
3. The effect of axial stress and aspect ratio (of wall and panel) on multi-panel and multi-storey walls. These two factors interact and so there is a need to understand the interaction more clearly.
4. Experiments and modelling to relate the strength of a single panel test to the strength that may be expected in a multi-panel configuration.

More experiments are also encouraged to provide specific material properties for finite element modelling.

References

Abaqus (2014). *Abaqus Analysis User's Guide*.

Anderson, D. and Brzev, S. (2009). *Seismic Design Guide for Masonry Buildings*. Toronto, ON: Canadian Concrete Masonry Producers Association.

Alcocer, S. M. and Meli, R. (1995). Test program on the seismic behaviour of confined masonry structures. *TMS Journal*, 13(2), 68-76.

AS 3700-2011 (2011). *Australian Standard of Masonry Structures*. Sydney, NSW: Standards Australia.

Assa, B. and Dhanasekar, M. (2000). A layered line element for the flexural analysis of cyclically loaded reinforced concrete beam–columns. *Computers & Structures*, 78(4), 517-527.

Banting, B.R., El-Dakhakhni, W.W. (2014). Normal strain-adjusted shear strength expression for fully grouted reinforced masonry structural walls. *Journal of Structural Engineering*, 140(3).

Benli, G., and Houqin, Z. (1991). The seismic resistance behavior of partially reinforced brick walls. *Proceedings of the 9th International Brick/Block Conference*, Berlin, Germany, 481-489.

Benzeggagh, M.L. and Kenane, M. (1996). Measurement of mixed-mode delamination rracture toughness of unidirectional glass/epoxy composites with mixed-mode bending apparatus. *Composites Science and Technology*, 56, 439–449.

Bernardini, A., Modena, C., Lazzaro, G. and Valluzzi, M.R. (1997). Cyclic behaviour and modelling of reinforced masonry panels. *Proceedings of the 11th International Brick/Block Masonry Conference*, Shanghai, China, 40-49.

Bolhassani, M., Hamid, A.A., Moon, F.L. (2016). Enhancement of lateral in-plane capacity of partially grouted concrete masonry shear walls. *Engineering Structures*, 108, 59-76.

Brunner, J.D. and Shing, P.B. (1996). Shear strength of reinforced masonry walls. *The Masonry Society Journal*, 14(1), 65-77.

Chen, X. and Liu, Y. (2015). Numerical study of in-plane behaviour and strength of concrete masonry infills with openings. *Engineering Structures*, 82, 226-235.

CSA S304-14 (2014). *Design of Masonry Structures*. Mississauga, ON: Canadian Standards Association.

Da Porto, F., Mosele, F. and Modena, C. (2009). Reinforced clay masonry walls under shearcompression loads: experimntal behaviour. *Proceedings of the 11th Canadian Masonry Symposium*, Toronto, Canada, 39-48.

Davidson, B. J., Brammer, D.R. (1996). Cyclic performance of nominally reinforced masonry walls. NZNSEE Conference, New Polymouth, New Zealand, 144-151.

Dhanasekar, M. (1985). *The performance of brick masonry subjected to inplane loading* (PhD thesis). University of Newcastle, Australia.

Dhanasekar, M. and Haider, W. (2008). On the inplane shear and simplified design provisions for reinforced masonry in AS3700. *Proceedings of the Australian Structural Engineering Conference*, Melbourne, Australia, 133-145.

Dhanasekar, M., Haider, W. and Janaraj, T. (2011). Response of partially grouted wider reinforced masonry walls to in-plane cyclic shear. *Proceedings of the 7th International conference*, Krakow, Poland, 112-124.

Dhanasekar, M., Shrive, N.G. and Page, A.W. (2008). On the design of wide spaced reinforced masonry shear walls. *Proceedings of the Australasian Conference on the Mechanics of Structures and Materials*, CRC Press Balkema, Netherlands, 509-515.

Dhanasekar, M., Steedman, M. and Nguyen, H. (2001). Effect of spacing of reinforcement on the in-Plane shear response of masonry walls. *Proceedings of the 6th Australasian Masonry Conference,* Adelaide, Australia, 135-144.

Dickie, J.E., and Lissel, S.L. (2009). Comparison of in-plane masonry shear models. *Proceedings of the 11th Canadian Masonry Symposium*, Toronto, Canada.

Drysdale, R. G. and Hamid, A. A. (1979). Behavior of concrete block masonry under axial compression. *ACI Journal Proceedings*, 76 (6), 707-722.

Drysdale, R. G., Hamid, A. A. and Baker, L. R. (1993). *Masonry Structures: Behaviour and Design*. Englewood Cliffs, NJ: Prentice Hall Inc.

ElGawady, M.A., Lestuzzi, P. and Badoux, M. (2005). Performance of masonry walls under in-plane seismic loading. *The Masonry Society Journal*, 23, 85-104.

Fattal, S. G. (1993) The effect of critical parameters on the behavior of partially grouted masonry shear walls under lateral loads. In NISTIR 5116, Gaithersburg, MD, 45: National Institute of Standards and Technology.

Ghanem, G.M., Salama, A.E., Elmagd, S.A., and Hamid, A.A. (1993). Effect of axial compression on the behavior of partially reinforced masonry shear walls. *Proceedings of the 6th North American Masonry Conference*, Philadelphia, 1145–1157.

Haach, V. (2009). *Development of a design method for reinforced masonry subjected to inplane loading based on experimental and numerical analysis* (PhD thesis). University of Minho.

Haider, W. (2007). *In-plane response of wide spaced reinforced masonry shear walls* (PhD thesis). Central Queensland University.

Haider, W. and Dhanasekar, M. (2004a). Experimental study of monotonically loaded wide spaced reinforced masonry shear walls. *Australian Journal of Structural Engineering*, 5(2), 101-118.

Haider, W. and Dhanasekar, M. (2004b). Deformation characteristics of wide spaced reinforced masonry shear walls. *Proceedings of the 7th Australasian Masonry Conference*, Newcastle, 93-101.

Hamedzadeh, A. (2013). *On the Shear Strength of Partially Grouted Concrete Masonry* (MSc thesis). University of Calgary.

Hamedzadeh, A. and Shrive, N.G. (2013). The effect of aspect ratio on the shear strength of partially grouted concrete masonry with wide-spaced reinforcement. *Proceedings of the 12th Canadian Masonry Symposium*, Vancouver, 12 pp.

Hansen, K. F., Nykanen, E. and Gottfredsen, F. R. (1998). Shear behaviour of bed joints at different levels of precompression. *Masonry International*, 12 (2), 70-78.

Ingham, J.M., Davidson, B.J., Brammer, D.R. and Voon, K.C. (2001). Testing and codification of partially grout-filled nominally-reinforced concrete masonry subjected to in-plane cyclic loads, *The Masonry Society Journal*, 19(1), 83-96.

Janaraj, T., and Dhanasekar, M. (2014). Finite element analysis of the in-plane shear behaviour of masonry panels confined with reinforced grouted cores. *Construction and Building Materials*, 65, 495-506.

Janaraj, T., and Dhanasekar, M. (2015). Effectiveness of two forms of grouted reinforced confinement methods to hollow concrete masonry panels. *Journal of Materials in Civil Engineering*, 27 (12).

Janaraj, T., and Dhanasekar, M. (2016a). Studies on the existing in-plane shear equations of partially grouted reinforced masonry. *Australian Journal of Structural Engineering*, 17(3), 180-187.

Janaraj, T., and Dhanasekar, M. (2016b). Design expressions for the in-plane shear capacity of confined masonry shear walls containing squat panels. *Journal of Structural Engineering*, 142(2).

Janaraj, T., Dhanasekar, M. and Haider, W. (2011). Wider reinforced masonry shear walls subjected to cyclic lateral loading. *Architecture Civil Engineering Environment*, 4, 39-46.

Jianguo, F. and Jingqian, X. (1986). Experiment study of shear strength of reinforced masonry walls under cyclic loading. *Proceedings of the 4th Canadian Masonry Symposium*, Fredericton, 581-595.

Kaminosono, T., Isoishi, H., Yamaguchi, Y. and Kaway, R. (1986). Seismic capacity of reinforced masonry walls including effects of axial stress. *Proceedings of the 4th Canadian Masonry Symposium*, New Brunswick, Canada, 163-174.

Kaminosono, T., Teshigawara, M., Hiraishi, H., Fujisawa, M., and Nakaoka, A. (1988). Experimental studies on seismic performance of reinforced masonry walls. *Proceedings of the 9th World Conference on Earthquake Engineering*, International Association for Earthquake Engineering, Tokyo, 109-114.

Khattab, M.M. and Drysdale, R.G. (1993). The effect of reinforcement on the shear response of grouted concrete masonry. *The Masonry Society Journal*, 12(1), 38-44.

Loov, R.E. (2000). Shear design of concrete – a simpler way, *Proceedings of the 3rd Structural Specialty Conference*, Canadian Society for Civil Engineering, London, Ontario, 49-56.

Lourenço P.B. (1996). *Computational strategies for masonry structures* (PhD thesis). Delft University of Technology, Delft, Netherlands.

Mahmoud, A.D.S., Hamid, A.A., and Magd, A.E. (1995). Lateral response of unreinforced masonry shear walls. *Proceedings of the 7th Canadian Masonry Symposium*, McMaster University, Hamilton, Ontario, Canada. 110-125.

Maleki, M., Drysdale, R.G., Hamid, A.A. and El-Damatty, A.A. (2009). Behaviour of partially grouted reinforced masonry shear walls- experimental study. *Proceedings of the 11th Canadian Masonry Symposium*, Toronto, Ontario, Canada.

Mann, W. and Muller, H. (1982). Failure of shear stressed sasonry- an enlarged theory, tests and application to shear walls. *Proceedings of the British Ceramic Society*. 30, 223-235.

Masami, F., Tishikazu, K. and Yoshiharu, Y. (1986). Seismic capacity of reinforced masonry walls: effect of shear span ratio. *Proceedings of the 4th Canadian Masonry Symposium*, New Brunswick, Canada.

Matsumura, A. (1987). Shear strength of reinforced hollow unit masonry walls. *Proceedings of the 4th North American Masonry Conference*, Los Angeles, California, USA.

MSJC (2013). *Building Code Requirements and Specifications for Masonry Structures*. Masonry Standards Joint Committee, The Masonry Society (TMS).

Oan, A.F., and Shrive, N.G. (2011). Influence of axial stress on shear performance of concrete masonry walls. *Proceedings of the 9th Australasian Masonry Conference*, Queenstown, New Zealand, 10 pp on CD.

Oan, A.F., and Shrive, N.G. (2015). The effect of horizontal reinforcement embedded in bond beams in concrete masonry walls. *Proceedings of the 12th North American Masonry Conference*, Denver, 13pp on CD.

Petersen, R. (2009). *In-plane shear behaviour of unreinforced masonry panels strengthened with fibre reinforced polymer strips* (PhD thesis). University of Newcastle.

Riddington, J.R. and Naom, N.F. (1994). Finite element prediction of masonry compressive strength. *Computers & Structures*, 37(6), 9.

Schultz, A.E. (1994). NIST research program on the seismic resistance of partially-grouted masonry shear walls. *National Institute of Standards and Technology*, Gaithersburg, MD, NISTIR 5481.

Schultz, A.E., Hutchinson, R.S. and Cheok, G.C. (1998). Seismic performance of masonry walls with bed joint reinforcement. *Proceedings of the Structural Engineers World Congress*, San Francisco, T119-4.

Schultz, A.E., Hutchinson, R.S. and Cheok, G.C. (2000). Seismic performance of masonry walls with bed joint reinforcement. *Proceedings of the 12th International Brick/Block Masonry Conference*, Madrid, Spain, 1625-1631.

Scrivener, J.C. and Baker, L.R. (1988). Factors influencing grouted masonry prism compressive strength. *Proceedings of the 8th Brick and Block Masonry*, London, Elsevier Applied Science 2: 874-883.

Shing P.B. and Cao L. (1997). Analysis of partially grouted masonry shear walls. *National Institute of Standards and Technology*, Gaithersburg, MD, NISTIR GCR, 97-710.

Shing, P.B., Brunner, J.D. and Lotfi, H.R. (1993). Evaluation of shear strength of reinforced masonry walls. *The Masonry Society Journal*, 12(1), 61-76.

Shing, P.B., Schuller, M. and Hoskere, V.S. (1990). In-Plane resistance of reinforced masonry shear walls. *Journal of Structural Engineering*, 116 (3), 619-640.

Shrive, N.G. (1983). Compression testing and cracking of plain concrete. *Magazine of Concrete Research*, 35, 27-39.

Shrive, N.G. and Page, A.W. (2008). In-plane cyclic loading of partially grouted masonry – a review and assessment of research needs. *Proceedings of the 14th International Brick and Block Masonry Conference*, Sydney, 10 pp on CD.

Shrive, N.G., Page, A.W., Simundic, G. and Dhanasekar, M. (2009). Shear tests on wide spaced partially reinforced squat masonry walls. *Proceedings of the 11th Canadian Masonry Symposium*, Toronto, 223-232.

Stafford Smith, B. and Carter, C. (1969). A method of analysis for infill frames. *Proceedings of the Institution of Civil Engineers*, 44, 31-48.

Steelman, J. and Abrams, D.P. (2007). Effect of axial stress and aspect ratio on lateral strength of URM shear walls. *Proceedings of the 10th North American Masonry Conference*, St. Louis, Lissouri, USA, 849-859.

Thamboo, J.A. (2014). *Development of thin layer mortared concrete masonry* (PhD thesis). Queensland University of Technology.

Timothy, P.H. (2010). *Evaluation of Masonry Walls Performance Under Cyclic Loading* (MSc thesis). Washington State University, Washington, USA.

Voon, K.C. and Ingham, J.M. (2004). Shear strength of concrete masonry walls. *Proceedings of the 7th Australasian Masonry Conference*, Newcastle, 102-111.

Voon, K.C. and Ingham, J.M. (2006). Experimental in-plane shear strength investigation of reinforced concrete masonry walls. *Journal of Structural Engineering*, 132 (3), 400-408.

Voon, K.C., Ingham, J.M. and Davidson, B.J. (2000). In-plane seismic response of reinforced concrete masonry. *Proceedings of the 12th International Brick and Block Masonry Conference*, Madrid, 921-935.

Yokel, F.Y. and Fattal, S.G. (1976). Failure hypothesis for masonry shear walls. *Journal of the Structural Division*, 102(3), 515-532.

Zhuge, Y. (1995). *Nonlinear dynamic response of unreinforced masonry under inplane lateral loads* (PhD thesis). Queensland University of Technology, Australia.

Zhuge, Y., Thambiratnam, D. and Corderoy, J. (1998). Nonlinear dynamic analysis of unreinforced masonry. *Journal of Structural Engineering*, 124(3), 270-277.